Master thesis and internship[BR]- Master's thesis : Investigation of TiN micro-heaters microfabrication pathways[BR]- Internship

Auteur : Batlle Mari, Lucas
Promoteur(s) : Fleury-Frenette, Karl
Faculté : Faculté des Sciences appliquées
Diplôme : Master en ingénieur civil en aérospatiale, à finalité spécialisée en "aerospace engineering"
Année académique : 2023-2024
URI/URL : http://hdl.handle.net/2268.2/20419

UNIVERSITY OF LIÈGE - SCHOOL OF ENGINEERING AND COMPUTER SCIENCE

Investigation of TiN μ-heaters microfabrication pathways

Master's thesis completed in order to obtain the degree of Master of Science in Aerospace Engineering by Lucas Batlle Mari

Author:
Lucas BATLLE MARI

Supervisor:
Dr. Karl FLEURY-FRENETTE

Committee members:
Pr. Eric ZIEMONS
Dr. Patrick GAILLY
Mr. Ismaël LAHMAÏD

Academic Year 2023-2024

Abstract

Mirrors onboard spacecrafts are too often contaminated before and during their journey into space by molecular species that can jeopardize the optical payload and, in some cases, the whole mission. The power-efficient outgassing of these molecular species stands as the motivation behind the integration of sub-surface microheaters into the mirror. This work is an investigation of preliminary steps in the microfabrication of titanium nitride microheaters to be integrated under the surface of flight mirrors.

The preparation of TiN thin films has been done by Ion Beam Sputtering over silicon (100) and magnesium fluoride substrates. Electrical resistivity, optical properties and roughness with respect to the thin film thickness have been studied for deposition over silicon (100). Finally, the thin film transfer from a magnesium fluoride substrate to a quartz surface has been tried with the Laser-Induced Forward Transfer (LIFT) technique with the prospect of characterizing it.

During this work, 15 coatings have been prepared with thicknesses ranging from 6 to 138 nm. A peak of resistivity has been observed for thin film thicknesses around 44 nm. This behavior has been explained by the intrinsic stresses variations inside the thin film. For studied coatings, optical properties are not constant with respect to the thickness. Surface roughness has been studied for thin films between 18 and 138 nm. Results have shown no significant variation as a function of thickness and the average roughness is 0.4 ± 0.1 nm. A titanium nitride line of 8 mm length and 129 μm width has been LIFT deposited.

Keywords : Microheaters, Titanium nitride, Sputtering, Laser-Induced Forward Transfer, Thin films.

Acknowledgements

First and foremost, I would like to express my sincere gratitude to Dr. Karl Fleury-Frenette, the supervisor of my Master's thesis. His continuous support, patience, knowledge and invaluable guidance throughout the entire project greatly contributed to its final outcome.

Besides my supervisor, I am deeply grateful to my committee members Pr. Eric Ziemons, Dr. Patrick Gailly and Mr. Ismaël Lahmaïd for their investment. It would like to thank Dr. Patrick Gailly for his help in lab experiments. Special thanks go to Ismaël for his availability and kindness. His comments guided my steps towards the completion of this work.

I would also like to thank the employees of the Centre Spatial de Liège (CSL). Especially Julien Rosin and Frédéric Rabecki for the trainings regarding the vacuum chamber utilization, and Cédric Hardy for substrate cleaning. I am also grateful to PhD students of the CSL Clément, Sélim and Maurice for their support and friendly atmosphere during breaks.

Thanks should also go to my office mates Nicolas, Emile and Lucas for their help, moral support and entertainment. Special thanks go to Lucas for his company and our chess sessions during midday breaks.

I would be remiss in not mentioning my friends for their emotional support and particularly Elric, Gilles and Amaury for their help with proofreading. Special thanks go to J., without him, it would not have been the same. I would also like to thank my partner Claire for giving me motivation and her beautiful smile throughout the year. Finally, my greatest gratitude goes to my parents, who always believed in me.

Table of Contents

Acronyms

AM Additive Manufacturing

ALD Atomic Layer Deposition

CSL Centre Spatial de Liège

CTE Coefficient of Thermal Expansion

CMOS Complementary Metal Oxide Semiconductor

DPN Dip-Pen Nanolithography

DC Direct current

DL Drude-Lorentz

DRL Dynamic Release Layer

FIB Focused ion beam

4PP Four-Point Probe

IR Infra-red

IBS Ion Beam Sputtering

LCVD Laser Chemical Vapor Deposition

LDT Laser Decal Transfer

LIBT Laser-Induced Backward Transfer

LIFT Laser-Induced Forward Transfer

MEMS Micro-Electromechanical Systems

MBE Molecular Beam Epitaxy

NIR Near InfraRed

PSI Phase Shifting Interferometry

QCM Quartz-Crystal Microbalance

RF Radio frequency

RMS Root Mean Square

sccm standard cubic centimeters per minute

UV Ultra-Violet

VSI Vertical Scanning Interferometry

VIS Visible

Introduction

For the past 20 years, the space industry has been in constant progress every year, making satellites more and more complex. Each innovation having in common its faculty to deal with the space environment. Satellite components are submitted to several hazards from their launch to their end of life. One of them is the contamination component which is due to external as well as internal sources of the satellite itself. On one hand, for the internal source, the contamination is directly related to the material outgassing of each spacecraft component. On the other hand, for the external source, the contamination is related to particles in the atmosphere or other spacecraft. This contamination can affect normal operations of the spacecraft at various severity levels and the main motivation is to limit its impact.

Mirrors are a recurrent component in satellites, with a lot of different applications. Those mounted inside optical systems result from very high precision manufacturing. As such, a small perturbation of its surface by foreign bodies has a direct impact on reflection conditions, leading to inaccuracies depending on the application. To remove these impurities, one way to proceed is by heating the mirror itself, to desorb contaminants deposited onto the surface.

A potential solution is integrating a heating system in the very vicinity of the mirror surface under the reflective coating. This system can be seen as a microheater, defined as an integrated heating device for micro-scaled systems. A microheater aims at providing efficient thermal management in Micro-Electromechanical Systems (MEMS) and its microfabrication is worth being investigated. The microheater itself is generally composed of a substrate on which a heating track is deposited. A way to make microheaters would be by preparing a thin film over a substrate and to transfer it onto the device by LIFT.

The main objective of this Master's thesis is to study the properties of TiN thin films to provide a strong basis for the fabrication of micro-heating systems integrated in satellite mirrors. All of this is motivated by the need to degas particles present on the mirror surface to minimize their impact on the overall optical system. It will also increase our knowledge on nano-scale TiN coatings properties and preparation. This work focuses on the analysis and discussion of experimental results obtained in laboratories during a four-month internship at the Centre Spatial de Liège (CSL).

TiN thin films were deposited using Ion Beam Sputtering (IBS) on silicon and magnesium fluoride substrates. Electrical resistivity, roughness and optical analysis were carried out for several thin film thicknesses. Some preliminary tests of TiN tracks deposition were performed by LIFT, with a basic topological characterization.

First, in chapter 1, this work introduces some generalities concerning microheaters and their applications. This part reviews the main microheating systems, with a focus on the most important properties heating tracks should have. Several materials are compared and the main motivations behind the choice of the TiN are detailed.

Then, chapter 2 briefly describes different ways to prepare TiN thin films, the actual lab instrumentation used to prepare them, and finally the prepared samples. The choice of IBS is motivated by being compared to other sputtering techniques. A detailed explanation of the experimental setup is also provided because the methodology to prepare the samples is an integral part the results discussion.

After that, chapter 3 introduces the instruments used for the characterization of the samples. This part is directly followed by chapter 4 and chapter 5, presenting and discussing the main results. First, the thickness of the samples is determined experimentally using a combination of characterization instruments. Then, the evolution of the roughness, resistivity and optical properties as a function of thickness is discussed.

Finally, the microheater track preparation and characterization is presented in chapter 6 after a presentation of the LIFT technique.

Chapter 1

Microheaters

Contents

One way to achieve decontamination of the mirror component is outgassing the impurities by integrating a heating system near its surface. This system can be seen as a microheater, and this section is therefore a state-of-the-art of what has already been done in MEMS concerning microheaters. A deeper focus is made on its constituting materials and their relevant properties.

Microheaters can be seen as a miniaturization of heaters (or hotplates), with the benefits of being less power consuming and having a lower thermal mass. Thus, more reactivity and higher temperature can be achieved. Their main function is to produce heat via methods such as Joule heating, ultrasonic, or radiative heating. The temperature that can be attained depends on several factors such as electrical, mechanical, and thermal properties, alongside material and geometrical characteristics [59]. Usually, the thickness of the heating filament/track is between ~ 100 nm and ~ 100 μm [21].

They are useful for a wide range of applications. For example, they can be integrated in microdevices, having applications in gas sensors, electron microscopes and pressure cells [21]. They can also be used as fuel cell heat sources, high power micro furnace and ignition systems. The electronics and substrate thermal regulation is also a motivation for the development of microheaters. Among all these applications, the requirements for microheaters mostly overlap and the differences are more about how the heater is supported and attached to the substrate [53].

According to Velmathi at al. [59], microheaters design ensures:

- a low power consumption,
- low thermal mass,
- a better uniformity of the temperature,
- enhanced thermal insulation from the surroundings.

Following these general requirements, it is possible to optimize the heating mechanism, the used materials and the geometry depending on the application. These aspects are described separately through the next three sections.

1.1 Heating mechanism

There are two main kinds of heating systems: internal and external. Such systems are illustrated in Concerning internal heating mechanisms, they are directly integrated inside the system through different micromachining methods. They are often used in microfluidics to control the temperature of the fluid [28]. Such a system is illustrated in Figure 1.1a. On the other hand, external microheaters are separated from the element to heat, or even not touching it. Thus, they are further divided in contact and non-contact heating techniques, where contact means that the microheater has been clamped or glued to allow for conduction. Another application for microfluidics is shown in Figure 1.1b. This system aims to heat a microfluidics device by sticking the microheater on its base. In contrast, non-contact heaters work with ultrasonic heating or radiation.

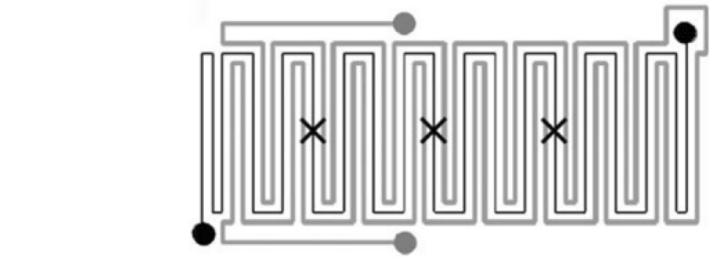

(a) Internal.

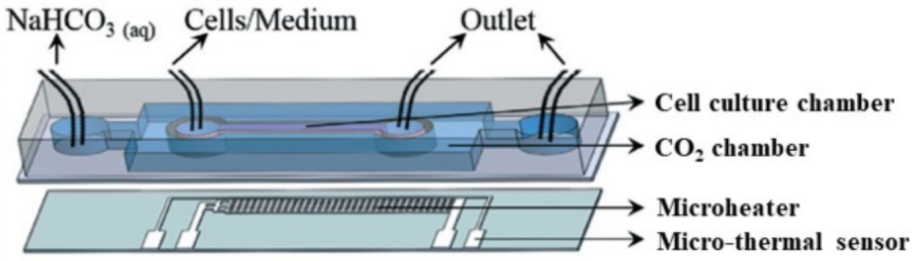

(b) External (contact).

Figure 1.1: Examples of heating microsystems [34],[23].

1.2 Materials description

Before going into the geometrical characteristics, it is important to have an overview of which materials are used for microheaters. The main goal is to know which parameters are important for both the thin film acting as the heating material and the substrate on which it will be deposited.

1.2.1 Heating material (thin film)

As a reminder, the purpose of the deposition is to have thermally functionalized surfaces outgassing impurities. It should therefore have strong thermal properties. In addition, it should also be compatible with the receiving surface in terms of adhesion and general properties. A non-exhaustive list of the important characteristics a microheater should have is proposed in Figure 1.2.

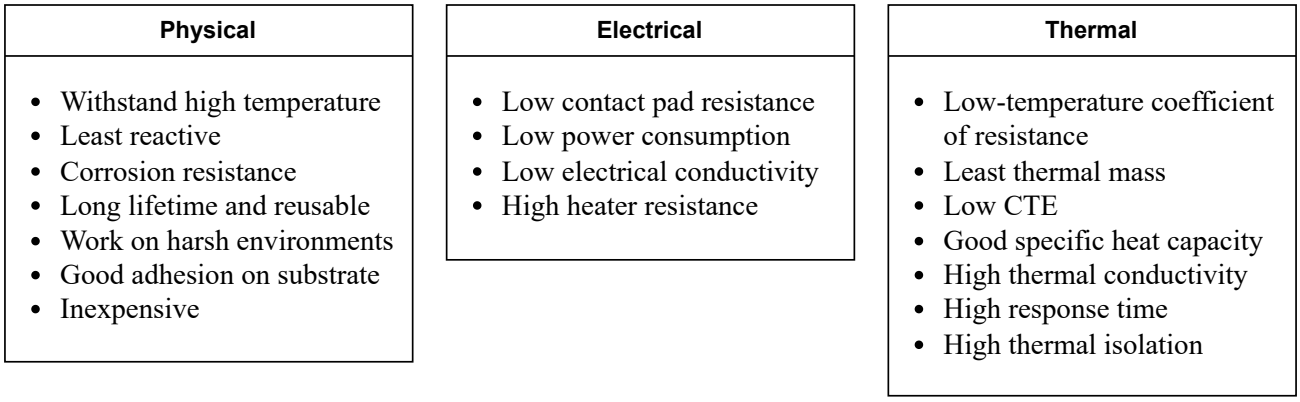

Figure 1.2: Ideal characteristics of a good microheater [21].

These mentioned characteristics can be interpreted as materials properties which are relevant for microheater applications [6]:

- high electrical resistivity,
- high thermal conductivity,
- low Coefficient of Thermal Expansion (CTE),
- high melting point,
- low Poisson's ratio,
- large Young's modulus.

Some additional constraints from the fabrication must be taken into account. Typically, the compatibiliy with the substrate in terms of properties.

According to the literature, commonly used materials are Pt, Au, Ag, Ti, W, Ni and NiCr. Some nitrides like titanium nitride (TiN) and gallium nitride (GaN) can also be used [21]. Moreover, some semiconducting materials such as doped silicon and polysilicon, silicon carbide and some doped metal oxides have been investigated [6]. Finally, some studies have been performed on hafnium diboride [51] and molybdenum [32]. In this section, the idea is not to make a materials selection, however, some aforementioned materials considered more relevant are going to be compared to the TiN in terms of properties. To complete the comparison, Table 1.1 summarizes all the selected properties for the analysis. It is worth mentioning that these data for bulk materials are likely to differ for thin films. In fact, they vary depending on their fabrication method, dimensions and composition [53]. However, it remains a good first indicator for the design of a microheater.

Table 1.1: Bulk properties for different heater materials [6], [53]

Property	**Al**	**Ni**	**Pt**	**Ti**	**TiN**	**Mo**
Electrical resistivity [$\mu\Omega$-cm]	2.65	6.93	10.5	54.3	20	5.34
Yield strength [MPa]	205	138	180	-	8600	1150
CTE [x$10^{-6}K^{-1}$]	14.2	13.4	8.8	8.6	9.35	4.8
Thermal conductivity at 300K [W m$^{-1}K^{-1}$]	318	90.9	71.6	21.9	19.2	138
Melting point [$^{\circ}C$]	1064	1455	1768	1668	2930	2623
Density [Kg/m^3]	19320	8908	21090	4507	5220	1022
Youngs modulus [GPa]	79	200	168	116	79-250	329
Poisson's ratio	0.44	0.31	0.38	0.32	-	0.307
Specific heat [J/Kg-K]	900	440	130	129	-	250

First, the drawbacks of Al and Au are their low resistivity and poor adhesion [6]. Concerning Pt, it is used at temperatures of $\simeq$ 500°C, its main drawback is its price and the fact that its resistivity begins to drift above 650° [6]. At a lower cost, Ni can be used instead. To reach a higher melting point, molybdenum seems to be a suitable option, having also the advantage to have an easy deposition [32]. At last, Ti films are also possible, but the melting point of the TiN is higher.

Concerning the TiN, it is known for its hardness, good thermal conductivity and high electrical resistivity, as shown in Table 1.1. It is recognized for its high chemical stability at room temperature [43]. This stability is a critical parameter for thin films, ensuring also that their other properties remain stable. Its oxidation occurs at 800°C in air [43]. It is also an important characteristic when it comes to additive manufacturing techniques like ablation or material transfer. TiN coatings also offer the advantage of allowing the adjustment of residual stress over a wide range, therefore bolstering the heater's durability. Additionally, its heat conductivity is moderate, promising minimal conductive heat losses through connecting wires. In contrast, yield problems can appear due to high stress. Another advantage

is its faculty to operate at high temperatures: around 700°C [8]. Finally, its growth is compatible with Complementary Metal Oxide Semiconductor (CMOS) technology.

In terms of applications, TiN is usually used for protective coatings. Alternatively, it can be found in diffusion barriers [41] and solar energy converters [48]. Also, because of its gold color, it can be used for decorative coatings.

This Master's thesis application objective is to investigate the fabrication process of TiN microheaters, thus, some initial choices have been made among preparation methods. The preferred one is to prepare it in two main steps: first, the deposition of a TiN coating by sputtering, and second, the LIFT deposition of a TiN track on a selected substrate from the sputtered coating. Some sections dedicated to their description and state-of-the-art are involved in this report (chapter 2 and chapter 6).

As mentioned previously, the discussed properties are the ones of the bulk material. Although they can be a great initial indicator, a more detailed study depending on the geometry and the preparation process should be performed to obtain a more accurate characterization of the μ-heater material properties. In the literature, two parameters are critical for TiN: the thickness of the film and the concentration of nitrogen when creating the thin film.

First, a relevant property variation with respect to thickness is electrical resistivity. A study, done for layers made by Atomic Layer Deposition (ALD) for diffusion barriers application, reports a quite significant variation [66]. This variation is attributed to the surface effect for TiN thicknesses below 20 nm. The same kind of observation has been done for the corresponding roughness; both are shown in Figure 1.3. Even if the preparation conditions and the context are different for our study, they are a great indicator of how much a property can change with respect to the thickness.

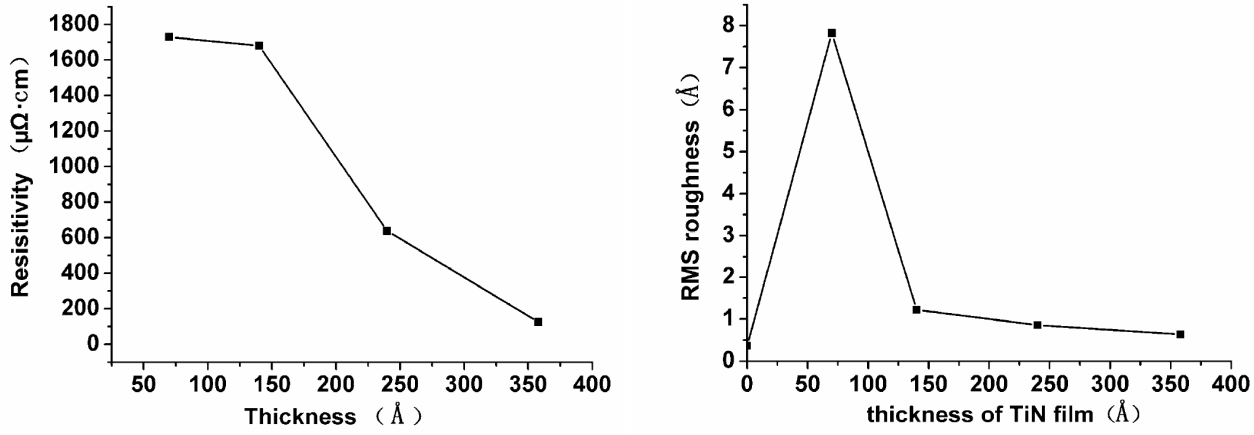

(a) Electrical resistivity.

(b) Roughness (RMS).

Figure 1.3: Electrical resistivity and roughness variation with respect to the thickness of TiN layers deposited by ALD [66].

Secondly, depending on the nitrogen flow provided during the deposition, different phases can appear in the material, thus changing its properties. The phase diagram of the TiNx is shown hereafter in Figure 1.4.

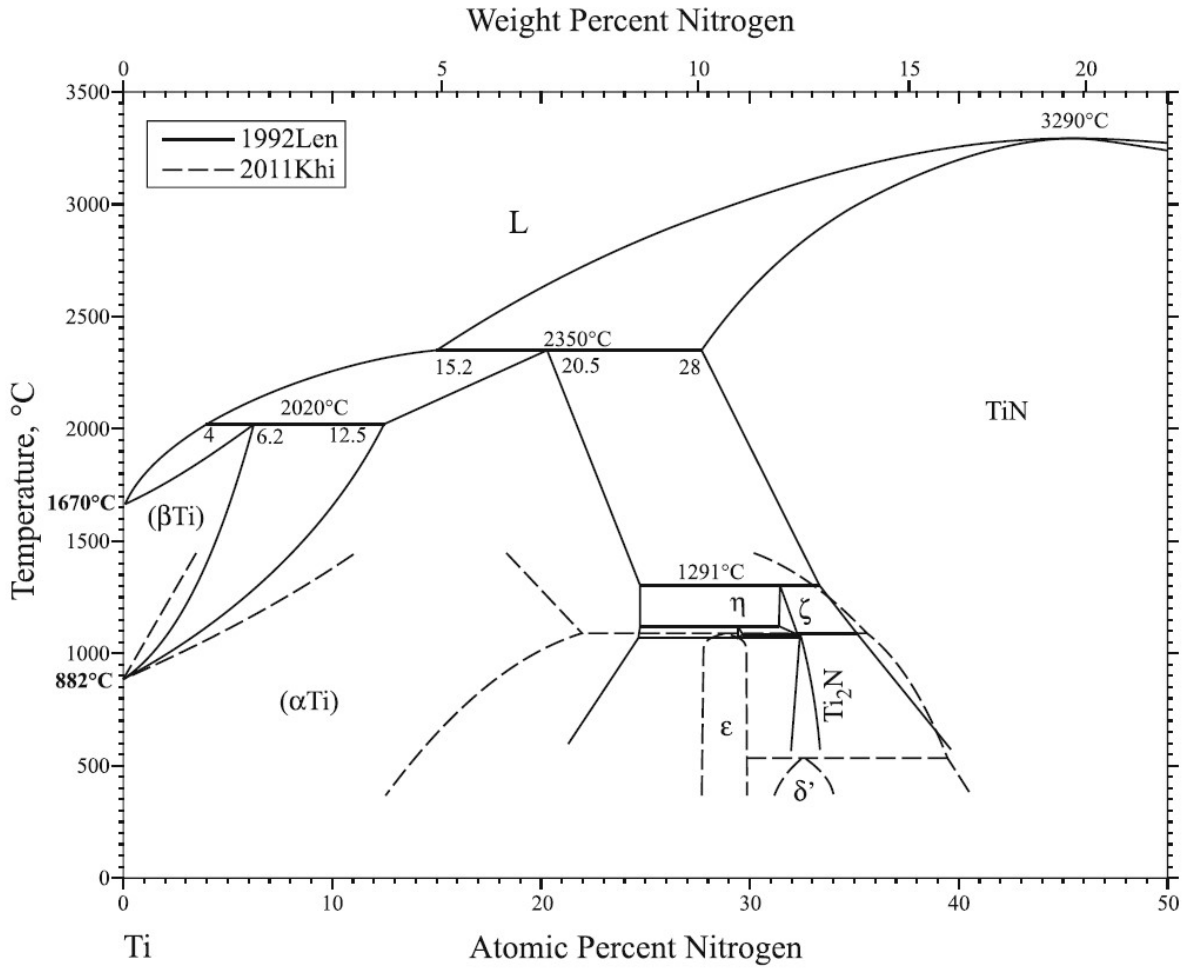

Figure 1.4: Phase diagram of the TiNx [33].

Depending on the partial pressure of N_2 injected during the process, the thin film can have a different nitrogen atomic percentage. When enough N_2 is injected, the material should be saturated. This happens generally for nitrogen atomic percentages greater than 40% [33]. In this area only, the material is composed of a single-phase TiN. When the atomic percentage becomes lower, it becomes a multi-phase film with the apparition of Ti_2N in its composition.

In the same way as for the previous example, another study focused on the effect of a changing nitrogen partial pressure on its properties for TiN is illustrated in Figure 1.5. Hardness and electrical resistivity variations of TiN and TiC films with respect to their composition ratio are shown. These films have a thickness of 0.3 to 7 μm and are prepared by Radio frequency (RF) sputtering [55].

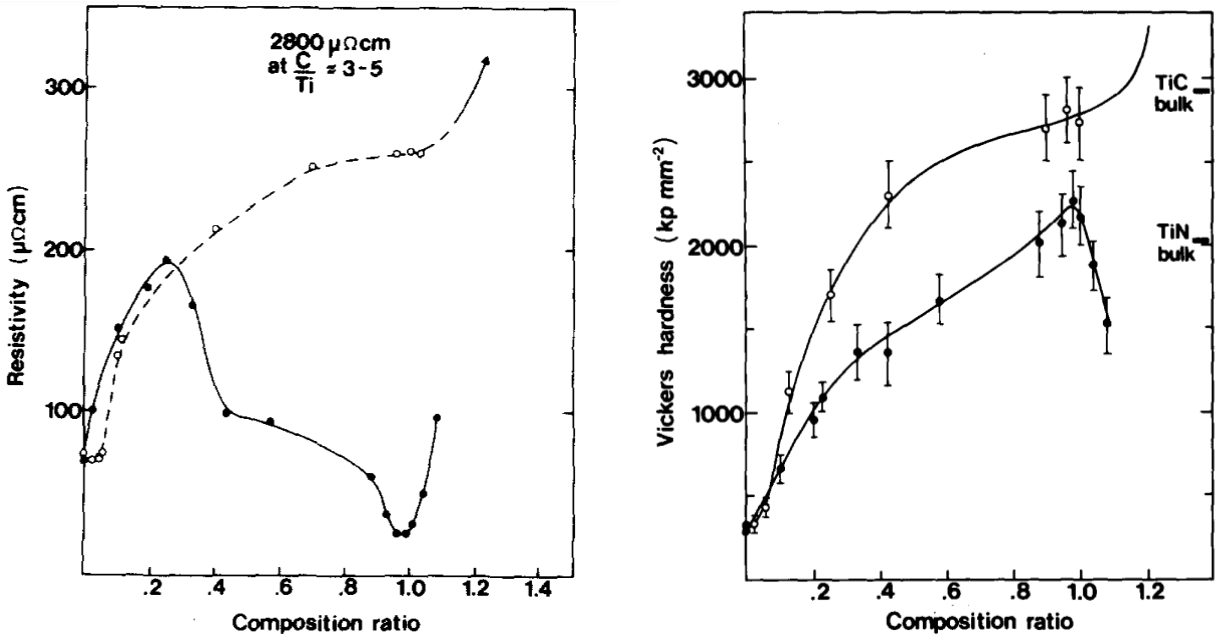

(a) Electrical resistivity.

(b) Hardness.

Figure 1.5: Electrical resistivity and hardness variations with respect to the nitrogen composition ratio of • TiN and ○ TiC coatings [55].

To summarize this section about the heating material description, TiN seems to be a suitable material fulfilling most of the conditions. Microheaters with TiN are less common but sufficient information is available to confirm their relevance for microheaters application.

However, when it comes to very small scales, less than $\sim 10\mu$m [55], some properties can vary a lot. This variation is also specific depending on the way the thin film is prepared and/or its dimensions. Thus, a detailed properties analysis is worth doing.

1.2.2 Substrate material

In a general way, microheater substrates are adapted to the application. For substrates in contact with the ground, low thermal conductivity is required. When the substrate is the intermediate layer between the heat transfer medium and the heater, its thermal conductivity must be as high as possible [53]. A non-exhaustive list of already investigated materials by researchers is available in Figure 1.6.

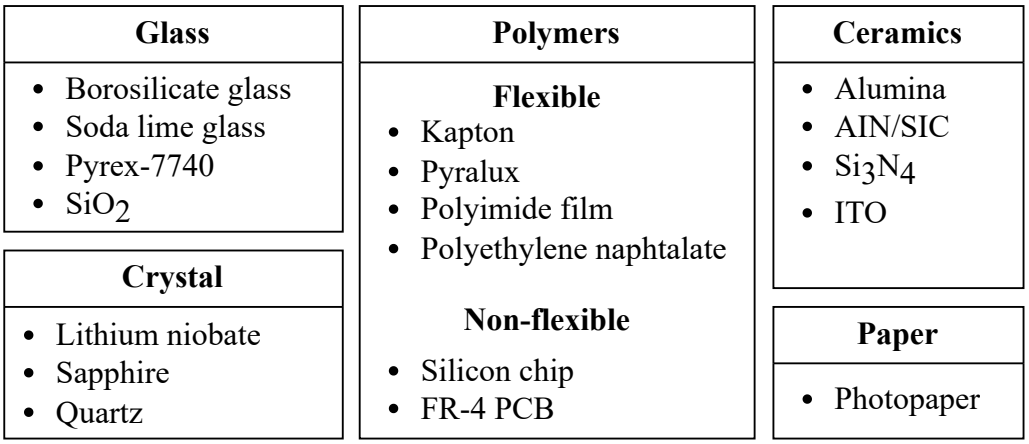

Figure 1.6: Already investigated substrate materials for microheaters classification [53].

1.3 Geometry

Geometry is the design parameter varying the most with respect to the desired application. Figures 1.7, 1.8 and 1.9 summarize what has already been studied in the field.

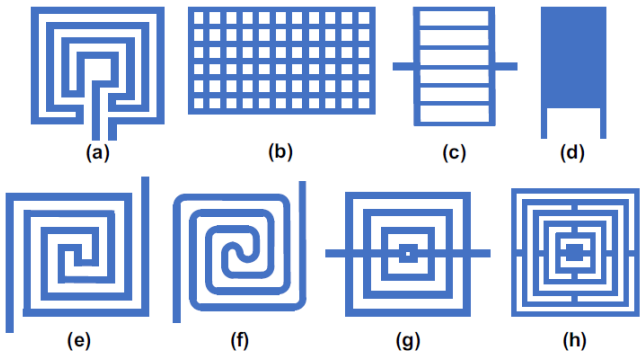

Figure 1.7: Box patterns investigated for the microheater track [53].

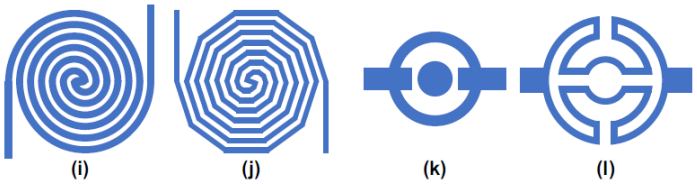

Figure 1.8: Annular patterns investigated for the microheater track [53].

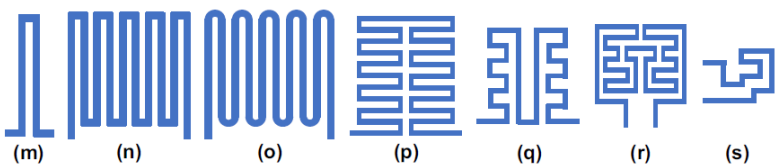

Figure 1.9: Serpentine patterns investigated for the microheater track [53].

The most important parameter for a track is its uniformity, i.e. the constancy of the generated temperature field [53]. Another important parameter is the efficiency of the microheater, directly related to its power consumption. For example, the double squared spiral model (e) is more efficient at high temperatures. Generally, tracks have a width of approximately 10 μm [53]. More specifically applied to TiN heaters for contamination outgassing, the optimum pattern still needs to be identified.

Chapter 2

Samples preparation

Contents

The investigation is made on TiN thin films deposited on Si(100) and MgF2 substrates. This section begins with some generalities concerning the Ion Beam Sputtering (IBS) and alternative sputtering methods. The description is followed by an explanation of the process before, during and after the thin film IBS deposition. Finally, the resulting samples and their initial characteristics are shown. In total, 15 samples have been prepared, covering thicknesses from 6 nm to 138 nm.

2.1 Ion Beam Sputtering (IBS)

Sputtering is a deposition technique aiming to deposit a thin layer onto a substrate by bombarding a target material with ions. The exposed target surface then sputters, and the goal is to place the substrate in the sputtering pathway to collect these ejected particles. Ideally, the substrate should be rotating, so that they are deposited uniformly on the substrate surface.

The main advantage of sputtering is its ability to deal with high melting point materials, like titanium. In addition, the method is very well known and is already used for a lot of applications, including thin film preparation [45]. However, it has the drawback of having a low utilization of the target material for some configurations resulting in a low deposition rate. As an alternative, Molecular Beam Epitaxy (MBE) can be used but it is heavier in terms of facilities. The main sputtering techniques are magnetron sputtering and the IBS [17].

First, magnetron sputtering is the most commonly used technique. It is seen as an upgrade of the glow discharge sputtering. The latter consists of having a Direct current (DC) or a Radio-Frequency (RF) power source which will apply a difference of potential between the target (having the role of cathode) and the anode. If the power source is DC, then the target needs to be a conductor. The process is performed at low plasma pressure, most of the time an Argon plasma. Typical values of 10^{-2} or 10^{-3} millibars can be obtained [35]. The potential difference therefore leads the Ar^{+} ions to be accelerated towards the target surface, and thus, ejecting atoms from the target collected as a layer on the substrate.

For magnetron sputtering, a circular magnetic field is introduced to trap the electrons near the surface of the target, having a "donut" shape. The ions hit the target and a thin film is formed on the substrate. Having a high density of electrons at a specific area on the surface can however be problematic, as the deposition will be higher on this zone than outside of it [17], this phenomenon is also known as "race track". The glow discharge sputtering and its implementation as magnetron sputtering are illustrated in Figure 2.1b.

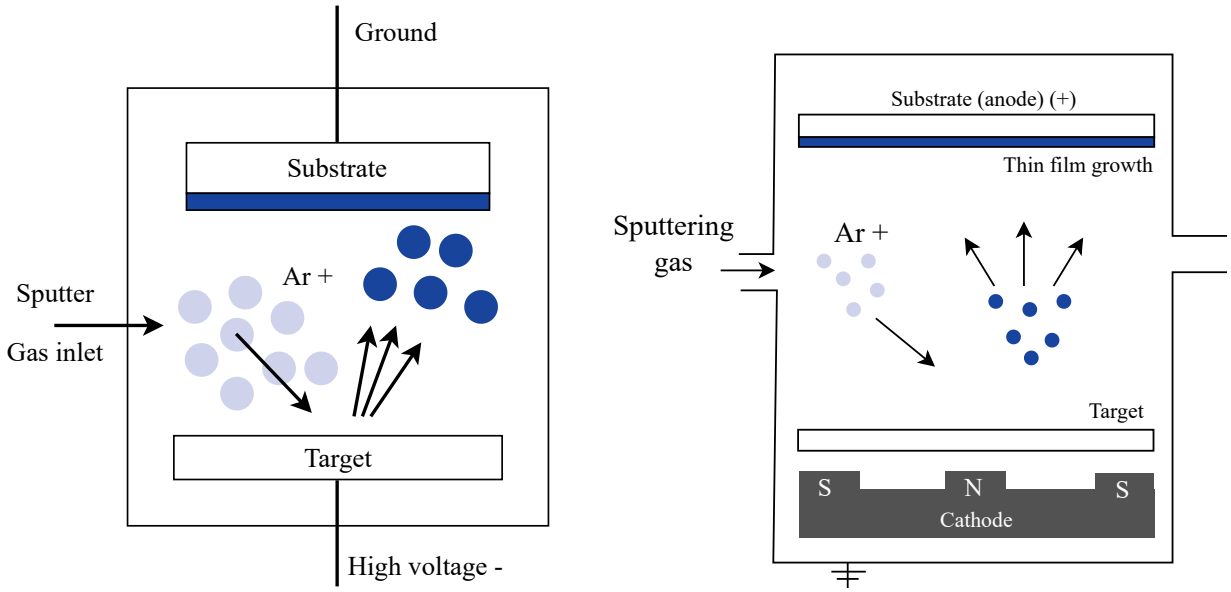

(a) Glow discharge sputtering.

(b) Magnetron sputtering.

Figure 2.1: Glow discharge and magnetron sputtering typical setups [17] [47].

Nevertheless, in this work, IBS is preferred to magnetron sputtering for thin films preparation. The main motivation behind this choice is that IBS allows better thickness monitoring and control of the thin film. In fact, the magnetron sputtering can be used for the preparation of TiN as well, and with a higher deposition rate. Concerning the working environment, IBS can be performed at lower pressures, typically around 10^{-4} or 10^{-5} millibars [42]. It also has the advantage of not being in contact with plasma, contrarily to magnetron sputtering. Before diving into all the important components, an illustration of a typical IBS setup is shown in Figure 2.2. This sketch is also an introduction to the description of the IBS installation in the lab at CSL.

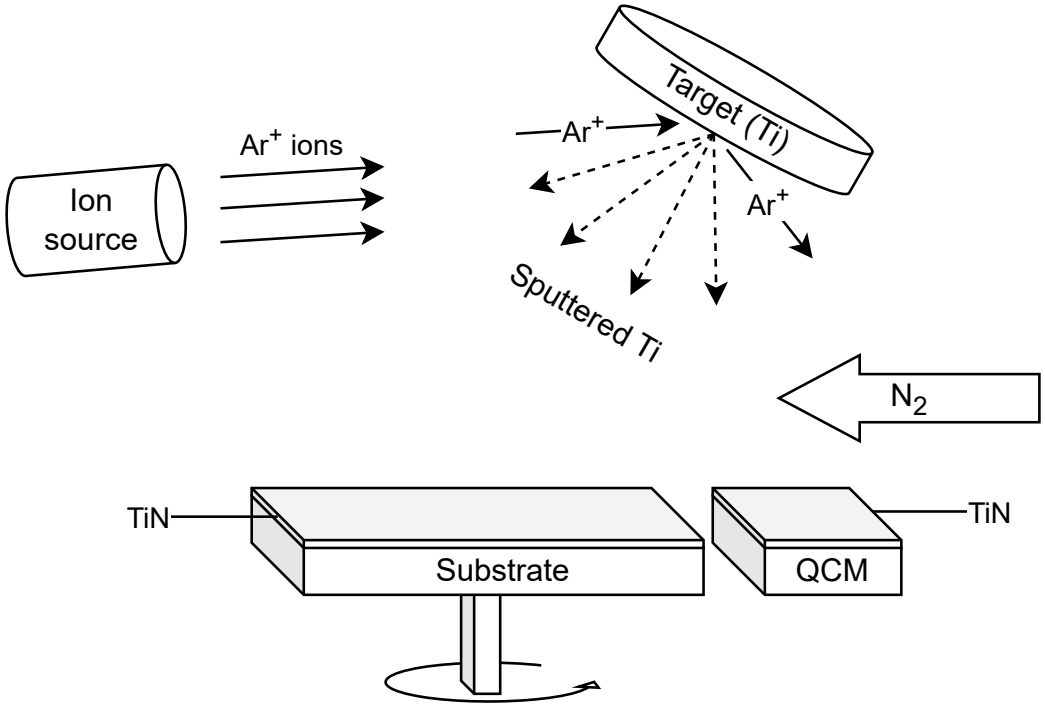

Figure 2.2: Used IBS setup.

IBS is performed by exposing a Ti target with positively charged ions (here, Ar^+ ions). A part of these ejected atoms can then "land" on a receiving substrate and form the desired layer. As a TiN thin film needs to be created, N_2 atoms are provided to the environment. Ti atoms in the environment can then react with the N_2 injected gas to form TiN. The IBS configuration allows the beam to be totally independent of the target and substrate potentials and provides the ability to easily create multilayers. The practice is also well known and studied, and several nitride depositions have already been performed by introducing a reaction gas [27].

The deposited thickness is monitored via a Quartz-Crystal Microbalance (QCM), placed just next to the substrate. A QCM is composed of a piezoelectric crystal and couples the mass load versus the frequency of the used crystal to determine the thickness of this mass load [4]. However, the layer deposited on the QCM can be different from what is truly deposited on the substrate, as it is not at the same position as the substrate. Additionally, the QCM takes as input the acoustic impedance of the material, which can be different in reality compared to what can be found in the literature. Calibration is therefore needed by iterating the thickness calculations involving other instruments. This procedure is explained in more detail in chapter 4.

The Ar^+ ions can be generated either by a Penning ion source or a Kaufman ion source, which are represented in Figure 2.3.

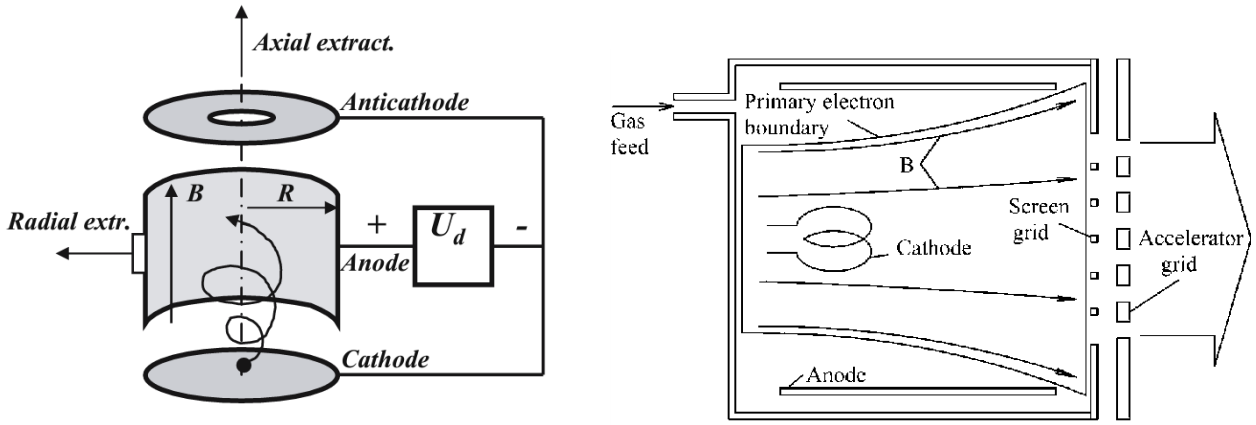

(a) Penning ion source.

(b) Kaufman ion source.

Figure 2.3: Schematics of the possible ion source configurations [2][15].

On one hand, the Penning ion source is composed of two cathodes linked by a cylindrical anode in which an axial magnetic field is applied. By applying a potential between the cathode and the anode and coupled with the axial magnetic field, the electrons of the Ar gaz will have a helical path towards the anode (like for the magnetron sputtering). Then, the formed Ar^+ ions, which move towards the cathode, are extracted by letting an aperture in the cathode. Typically, for an Ar gaz, a potential of several hundred volts is needed [17].

On the other hand, the Kaufman ion source involves a cathode with thermal electron emission filaments. Another difference is the presence of grids with aligned multiple apertures, composing the anode with the cylindrical chamber. These grids have the same effect a lens can have for optical designs. Finally, for a typical Kaufman ion source, lower discharge potential and pressure are needed. For IBS, the used ion source is generally the Kaufman one. It has the advantage of generating a high current compared to the applied voltage. It is not common to do IBS with a DC current. Usually, the gas mix is directly introduced in a RF source [3].

The last part of the process is the combination of the Ti and N_2 atoms to create the final layer. Usually, a second ion beam pointing towards the receiving substrate is used. The objective is to have a more homogenous repartition of the molecules on the substrate surface. This application is crucial for the deposition of dielectrics but not for TiN deposition [17].

A summary of the main advantages and disadvantages of IBS is available in Figure 2.4.

Advantages	Drawbacks
• High melting point materials compatibility • Good thickness monitoring • No direct contact with plasma • Low pressure environment	• Low efficiency • Low deposition rate

Figure 2.4: Advantages and drawbacks of the deposition by Ion Beam Sputtering (IBS).

2.2 IBS facility

To perform the deposition, an initial pressure around $1 \cdot 10^{-6}$ mbar is needed, for a working pressure of $1 \cdot 10^{-4}$ mbar. So, the setup must be mounted inside a vacuum chamber. Some useful information is therefore given regarding the vacuum chamber and the ion source.

2.2.1 Vacuum chamber

The IBS is done in a vacuum chamber located in a Class 10000 clean room (ISO 7). A picture of its configuration is shown in Figure 2.5.

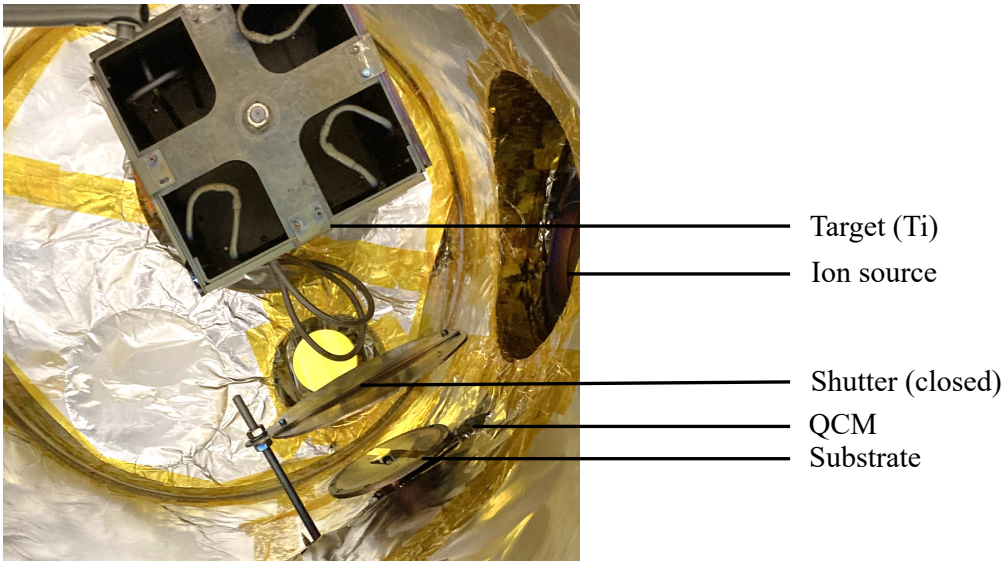

Figure 2.5: Disposition of the sputtering setup.

As a reminder, the installation aims to prepare the thin films: a Ti target is hit by the Ar^+ ion beam and is sputtered. Then, the Ti atoms react with the inserted nitrogen to form a thin film over the substrate. There is also the presence of a shutter, allowing the process to start and stop at specific moments, typically when the thickness detected on the QCM is reached.

As the sputtering is done at very low pressures, it is equipped with a vacuum generation system, illustrated in Figure 2.6.

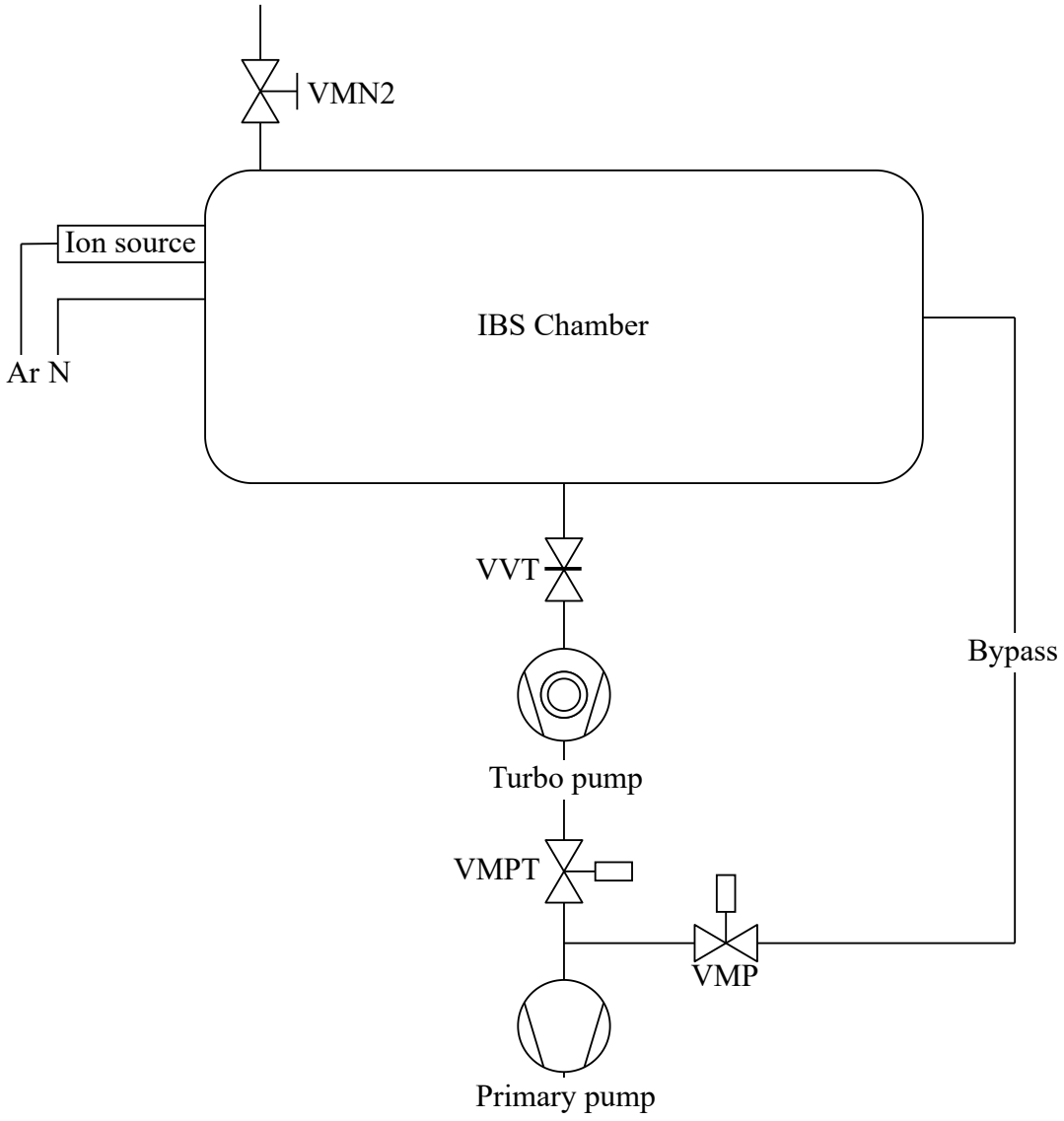

Figure 2.6: Vacuum generation system of the tank.

It comprises two pumps: the primary pump and the turbomolecular pump. The latter is rotating at 40000 RPM, this high velocity requires several steps to safely pump. The pumping procedure is described in the next paragraph.

When the chamber is initially at atmospheric pressure, a first pumping with the primary pump is done until reaching a pressure around $1{\cdot}10^{-1}$ mbar. This pumping is performed through the bypass circuit and lasts several minutes. Translating to Figure 2.6, the VVT and VMPT valves are closed, and the VMP is open. Then, a second pumping is performed with the turbo pump until reaching $1.6{\cdot}10^{-6}$ mbar. This process usually takes one night to reach the desired pressure. Before connecting the turbo pump to the tank, it is mandatory to open the VMPT to equilibrate pressures, then close the VMP and finally the VVT can be opened. After that, the sputtering process can be done. It is also worth mentioning that the chamber, initially at $1.6{\cdot}10^{-6}$ mbar, reaches a pressure of approximately $1{\cdot}10^{-4}$ mbar due to the injection of Ar and N gases. Finally, the venting of the chamber is necessary to get the atmospheric pressure back. All valves must be closed in order to isolate the chamber, then, the VMN2 valve can be opened.

2.2.2 Ion source

The last interesting part of the IBS facility is the ion source. It can be highlighted that the ion beam needs an incidence angle (ranging typically around 20-30°). The goal of this incidence is to minimize the exposure of the substrate scatter particles from the target.

Concerning the generated beam itself, its constituting positive ions Ar^+ are interacting with each other, repulsing themselves. Consequently, there is a natural divergence in the beam. To limit this effect, electrons can be injected in the beam through tungsten thermal electron emitters, with the objective to get the charge neutrality. The neutralizer is however not used in this work. It is illustrated in Figure 2.7.

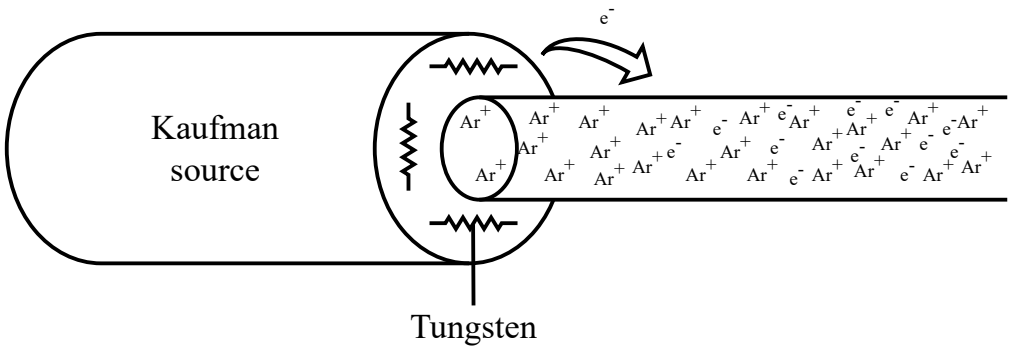

Figure 2.7: Source setup with neutralizer.

2.3 Preparation

The first step is to reach approximately $1.6{\cdot}10^{-6}$ mbar in the IBS vacuum chamber. After that, the injections of Ar (directly in the source) and N_2 (in the chamber) gases increase the working pressure to approximately $1{\cdot}10^{-4}$ mbar. In total, 15 samples are prepared by IBS in the previously presented chamber. To set up the deposition, the density and the acoustic impedance of the TiN must be added as inputs to the QCM. Concerning the process temperature, it is assumed to be at room temperature.

Next, the ion beam is powered on, the shutter is opened after a source stabilization time of $\sim$20 min and the sputtering can be initiated. Hereafter in Table 2.1 are presented the values of the deposition parameters during the process. The process is performed without neutralizer emission.

Table 2.1: Ion Beam Sputtering (IBS) important deposition parameters value.

Inlet gas flows	Nitrogen	2 scc/m
	Argon	4 scc/m
Source setup	Ionic current	35 mA
	Ionic voltage	940 V
	Acceleration voltage	350-260 V
	Discharge current	200-300 mA

It is worth noting that the deposition is monitored with the software *Maxtek* [19], in which the desired thickness can be indicated. When this thickness is detected on the QCM, the program automatically closes the shutter and provides information about the deposition time.

Concerning the indicated gas flow values, they are indicated in standard cubic centimeters per minute (sccm) which are equivalent to a flow of 1 cm^3/min at standard temperature and pressure. The amount of Ti atoms sputtered from the surface are linked to the Ar flow rate. So, varying both Ar and N flow rates leads to varying the saturation rate of nitrogen in the TiNx mix. Flow rate values indicated in Table 2.1 are based on previous depositions also performed in 2012 at the CSL. At that time, measurements by Rutherford Backscattering led to a nitrogen concentration of 40% in the TiNx mix. This concentration can be compared to the phase diagram of the TiNx in Figure 1.4: at standard temperature, the mix seems to have some Ti_2N molecules and is not totally composed of TiN.

Among all the prepared TiN samples,

- 14 are on a Si(100) substrate,
- 1 is on a MgF_2 substrate, for the LIFT.

Additionally, there is a sample only constituted of the Si(100) substrate to get artificially a 0 nm thickness. For each sample, Table A.1 gives the estimated thickness by the QCM t_{QCM}, the deposition date and the deposition duration. For a better understanding of which sample is discussed, a numeration based on the measured thickness is proposed. This numeration is strictly followed in this work. It is worth knowing that only sample 9 is the one deposited over a MgF_2 substrate and is intended for the LIFT in chapter 6. The remaining ones are all over Si(100) substrates and are intended for the characterization.

Finally, a picture of the target setup before and after the sputtering for samples 9 and 14 is shown in Figure 2.8.

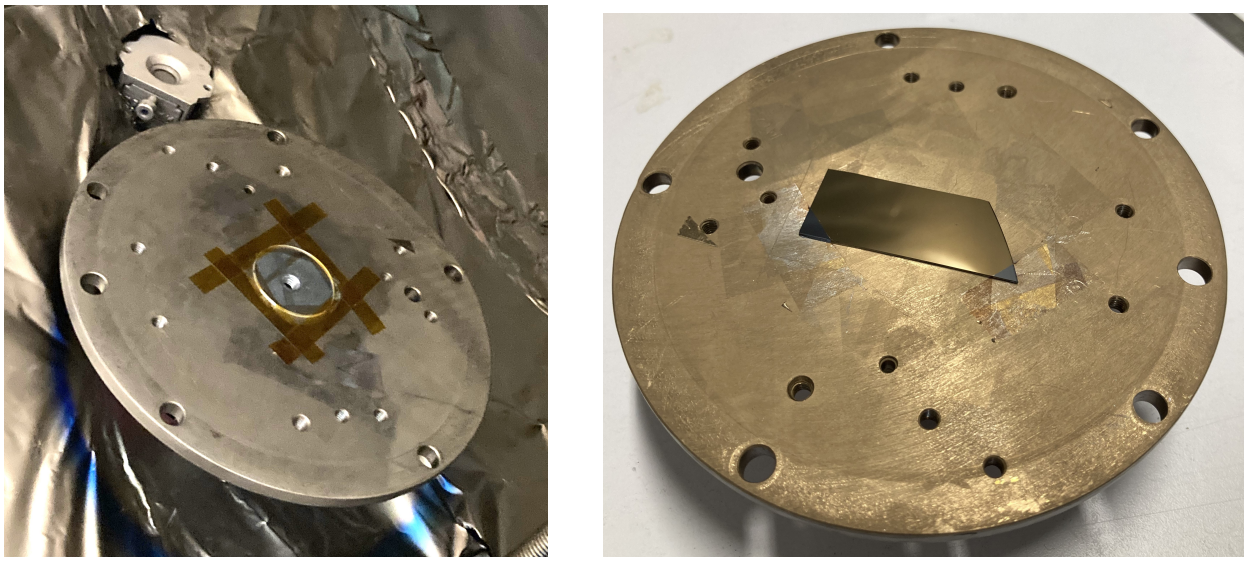

(a) Sample 9 (over MgF_2), before.

(b) Sample 14 (over Si), after.

Figure 2.8: Pictures of different samples before and after the deposition by IBS.

To conclude this chapter, after reviewing the important characteristics of the IBS, a detailed description of preparation facilities and process has been provided. The deposition by IBS occurs at pressures around $1{\cdot}10^{-4}$ mbar in a vacuum chamber. Concerning the thickness, it is monitored by the QCM, which was not calibrated at this stage. The measured thickness will be presented in a dedicated chapter.

Chapter 3

Characterization instruments

Contents

During this work, several instruments were used. Initially, the samples are coated in an IBS deposition chamber. Then, all the samples are characterized with the help of microscopes and ellipsometers. In parallel, the resistivity is also studied with a technique called the Four-Point Probe (4PP). Finally, the transfer to get a the final microheater track is performed by using a laser micromachining workstation. All the instruments are located in class 10000 clean rooms (ISO 7), at CSL. This means that the room is limited in terms of maximum particles per m^3: 352,000 particles larger than 0.5 μm, 83,200 $\geq 1\mu m$ and 29,300 $\geq 5\mu m$. This section is dedicated to the description and theoretical backgrounds related to each characterization instrument.

3.1 Microscopes

The inspection of the thin films is performed with microscopes. Both a digital microscope and an interferometric microscope (also referred to profiler). The digital microscope (Figure 3.1a) is used for the observation of the final track. The used model is the *Keyence VHX-5000*, handling magnifications up to 1000x. Its use is restricted to general observations because of its limited vertical resolution. The profiler (Figure 3.1b) generates an interference image on the camera to obtain a 3D profile. Higher vertical resolutions can therefore be attained. Depending on the magnification used, different interferometer models are used: the Michelson model is used for low magnifications ($\leq$ x5) and the Mirau model for high ones ($\geq$ x20). An example of a setup using a Michelson interferometer is illustrated in Figure 3.2.

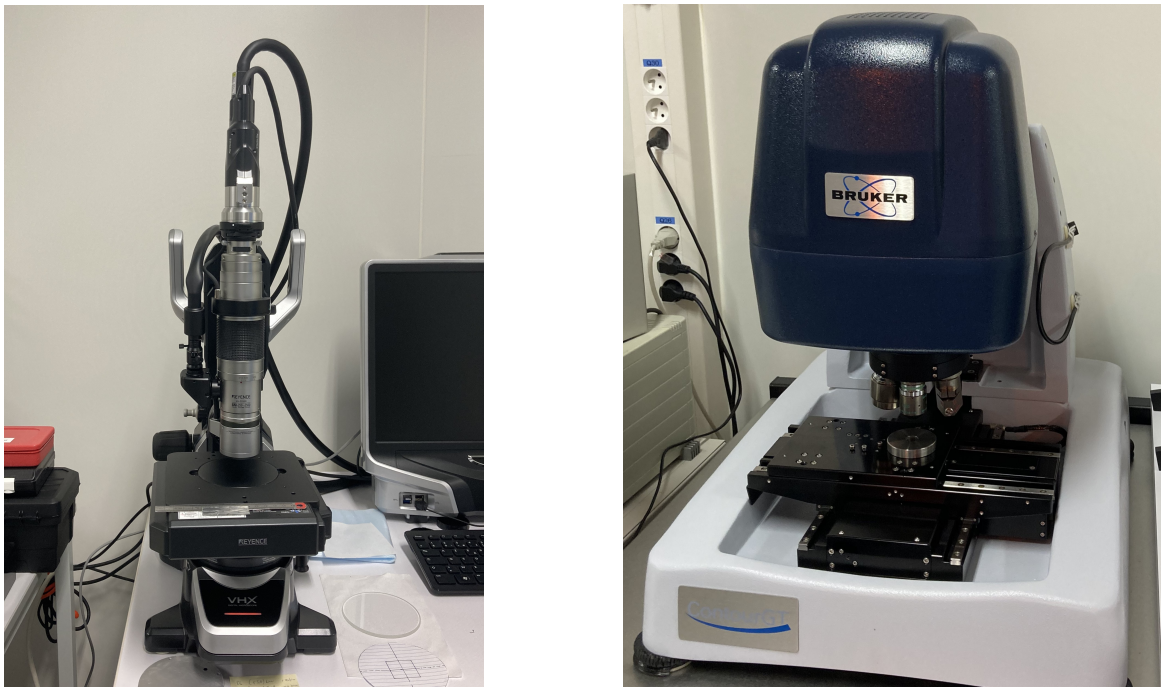

(a) Digital microscope.

(b) Interferometric microscope.

Figure 3.1: Pictures of the used digital and interferometric microscopes.

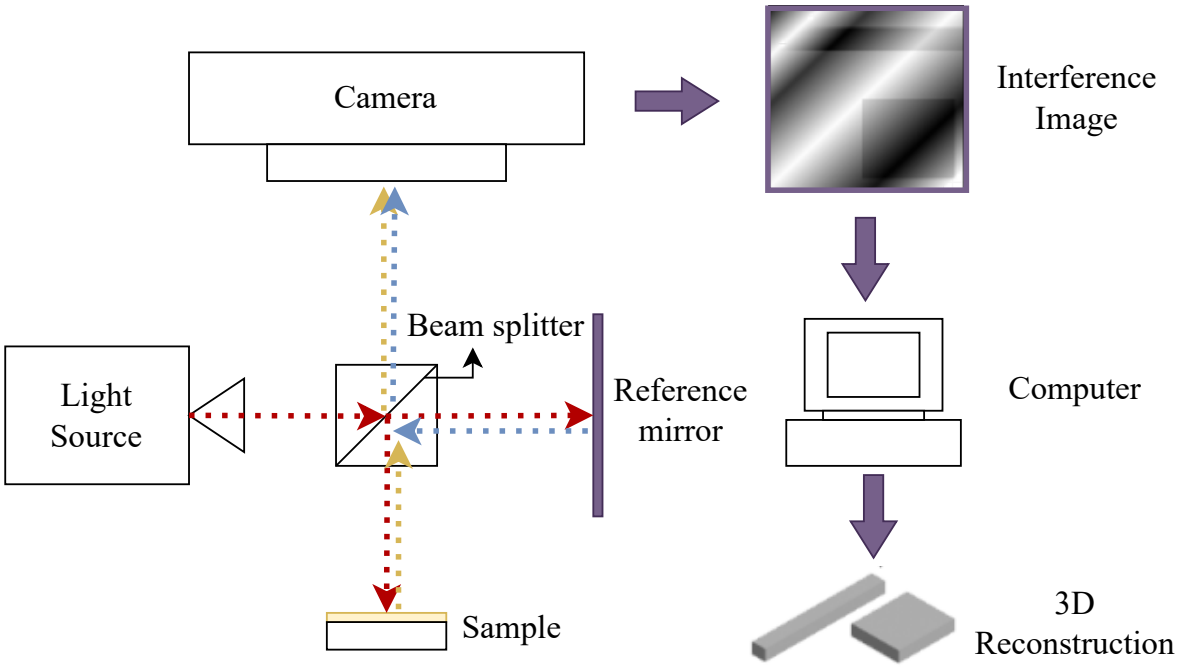

Figure 3.2: Typical setup of a profiler (Michelson interferometer) [38].

The precision of the profiler varies with the chosen measurement mode: Vertical Scanning Interferometry (VSI) or Phase Shifting Interferometry (PSI). The VSI, on one hand, uses a broadband (usually white) light source. It aims to move the objective to bring each point of the surface into focus to record their height. It reaches precision in the nanometer range and is typically used for rough surfaces. PSI, on the other hand, uses a narrowband light source (522 nm). During PSI measurements, the internal translator modifies the optical path length of the test beam. Each adjustment in the optical path results in a shift of the fringe pattern. Shifted fringes are periodically captured by the camera, creating a series of interferograms. Computer algorithms combine these interferograms to determine the surface height profile. The vertical resolution is thus more accurate than VSI, reaching the sub-nanometer scale.

The profiler is used to study two characteristics: the thin film thickness and surface roughness. When studying a sample composed of two or more materials in PSI, special attention is needed to ensure results relevance. The materials have different complex refraction indices and thus a change in the phase shift is induced, independently of the height difference. This can be avoided by adding a correction factor to the measured thickness, based on another measurement method. In the case of this work, correction factors have been used for the thickness calculation, from the thicknesses obtained by the ellipsometer. A more detailed analysis is done in chapter 4. The used profiler model is the *Bruker ContourGT*, working with the software *Vision64* [7].

3.2 Ellipsometer

Another useful instrument available in the lab is the ellipsometer. This instrument aims to analyze optical surfaces based on the change of the polarization state of light after reflection on them. An illustration of the polarization change of a reflected beam is displayed in Figure 3.3.

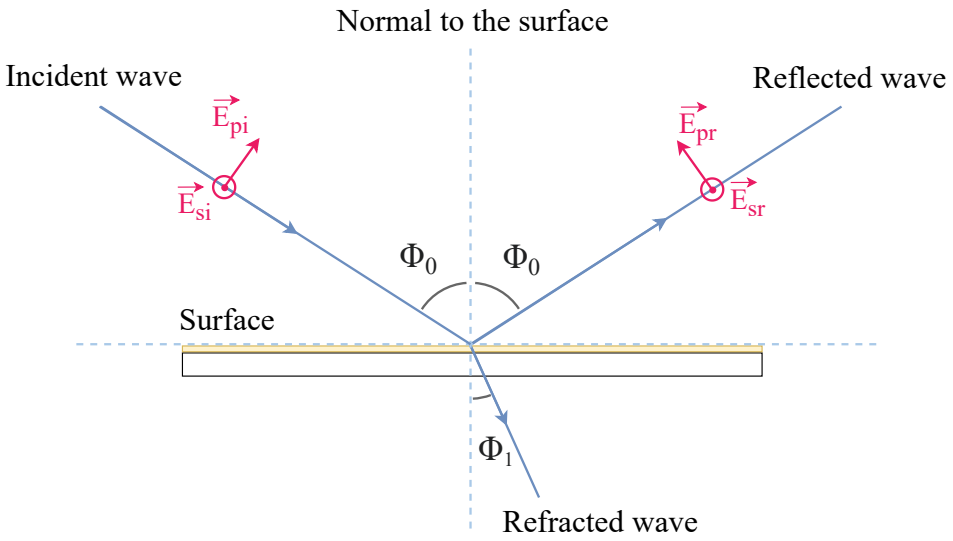

Figure 3.3: Reflection of polarization axes at the sample surface [5].

A polarized plane wave of known polarization is reflected by a (given) surface, and then measured in order to analyze the change of polarization due to the surface properties. In more details, the incident plane wave has an electric field composed of two components: one parallel to the incidence plane $\overrightarrow{E_{\text{pi}}}$ and another one perpendicular to it $\overrightarrow{E_{\text{si}}}$, as shown in Figure 3.3. The same terminology is used for the reflected electric field but replacing the "i" index by "r".

From these components, the reflection coefficients for both parallel and perpendicular polarization are given by [5]:

$$r_p = \frac{E_{\text{pr}}}{E_{\text{pi}}} = |r_p| e^{j\delta_p} \text{ and} \tag{3.1}$$

$$r_s = \frac{E_{\text{sr}}}{E_{\text{si}}} = |r_s| e^{j\delta_s} \,, \tag{3.2}$$

where δ_p and δ_s are the phase shift due to the reflection. Both coefficients are complex, so their ratio can be expressed as

$$\frac{r_p}{r_s} = \tan\Psi \cdot e^{j\Delta} \,, \tag{3.3}$$

where Ψ and Δ are the main parameters. Ψ is given by the modulus ratio and follows

$$\tan\Psi = \frac{|r_p|}{|r_s|} \,. \tag{3.4}$$

Δ is the phase difference due to the reflection. Assuming a massive and isotropic sample, the Descartes law can be applied and is given by

$$N_0 \cdot \sin\Phi_0 = N_1 \cdot \sin\Phi_1 \,, \tag{3.5}$$

where N_0 is the exterior medium index, $N_1 = n_1 + jk_1$ is the substrate index, with n_1 the real refraction index and k_1 the extinction coefficient. The angles Φ_0 and Φ_1 are the incident and refracted angles. Finally, Ψ, Δ, n and k can be linked with the continuity at the interface of the tangential components of the electric field $\overrightarrow{E}$ and the magnetic field $\overrightarrow{H}$ [5]:

$$r_p = \frac{N_1 \cos\Phi_0 - N_0 \cos\Phi_1}{N_1 \cos\Phi_0 + N_0 \cos\Phi_1} \,; \tag{3.6}$$

$$r_s = \frac{N_0 \cos\Phi_0 - N_1 \cos\Phi_1}{N_0 \cos\Phi_0 + N_1 \cos\Phi_1} \,. \tag{3.7}$$

Where (r_p, r_s) are the reflection coefficients. Thus, for a single known wavelength measurement at a certain angle, the ellipsometer can determine the indices n and k of a layer with a known thickness. It is also possible to get n and the thickness e from known wavelength, angle and extinction coefficient k. This is only true for one single layer.

For N layers of materials which are not optically opaque, the number of unknowns increases to $3N + 2$ unknowns, so it is not possible to find all unknowns, knowing that the measure is only on two quantities. The way to proceed is therefore to assume that the index of the layers is known or is the result of a known blend. As a result, only the thicknesses of each layer will be an unknown and the measurement should be done for a sufficiently large number of wavelengths [5].

Concerning the configuration and the way the ellipsometer works, an illustration is shown in Figure 3.4.

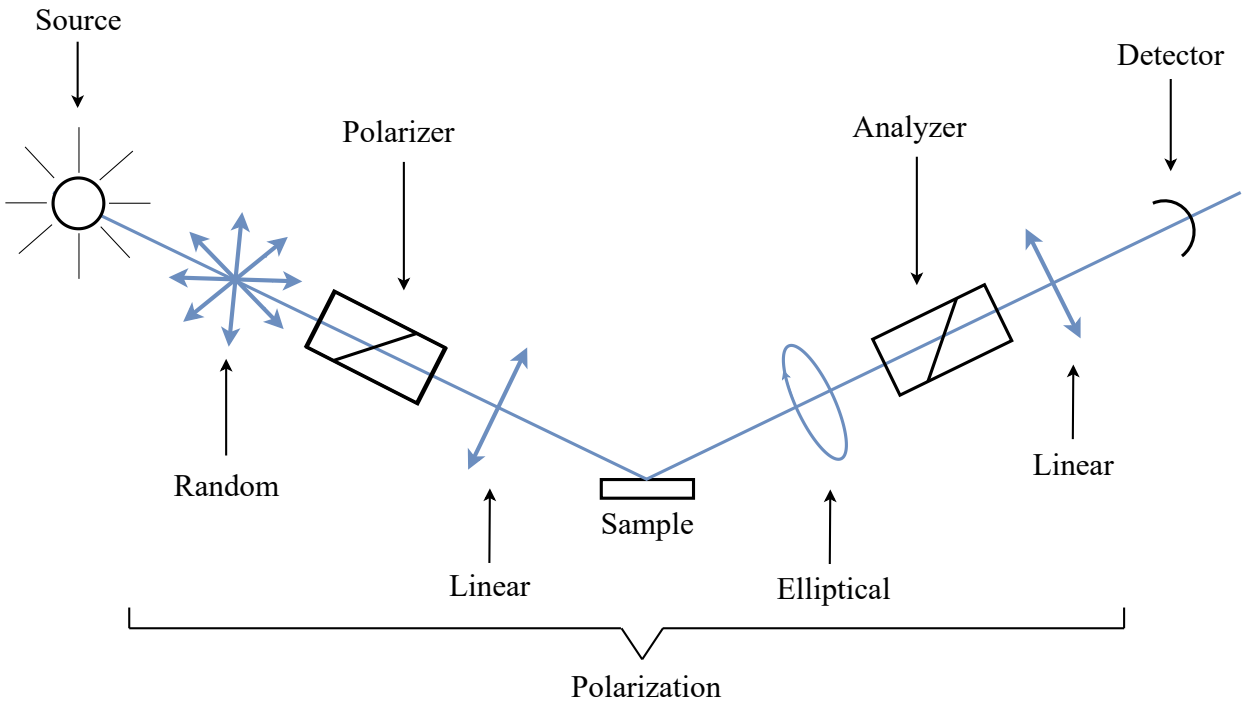

Figure 3.4: Ellipsometer configuration [5].

Several types of configurations are possible for an ellipsometer. The one used in the lab is the configuration with a rotating analyzer. The incident wave is first polarized linearly with a known polarization angle (45°). Then, after reflection, this polarization becomes elliptic due to the change in phase and amplitude. Finally, the analyzer is rotating to measure the modulus ratio $\tan \Psi$ and the change in phase Δ. The drawback of using a rotating analyzer is the need of having a detector insensitive to the polarization state. Moreover, the spectrometer must be placed between the source and the polarizer, leading to more sensitivity to parasite light.

In this work, the ellipsometer results are useful for several aspects. First, the $\Psi - \Delta$ coefficients are used to estimate the thickness of the deposited thin film layer. Their evolution with respect to the wavenumber of the incident beam is also used, to get an idea of the possible molecular content. In parallel, the evolution of the refraction coefficient n and the extinction coefficient k with respect to the wavelength are also interesting to analyze.

To obtain a thickness, the $\Psi - \Delta$ coefficients are compared to a model. This model is usually composed of the layers constituting the system and each of them corresponds to one specific material. This means that they contain the evolution of n and k with respect to the wavelength. From a model, the analysis part of the software can simulate the change of desired parameters to fit as well as possible the measured data and thus, estimate these parameters. Typically, the fit can be done by varying the thickness of a preselected layer entered in the model.

Two spectral ranges are analyzed: Ultra-Violet (UV)-Visible (VIS)-Near InfraRed (NIR) and Infrared (IR). They correspond to the ranges that can be handled by the two available ellipsometers in the lab: the *SENresearch 4.0* and the *SENDIRA (FTIR)*, both by *SENTECH*. Table 3.1 clarifies the corresponding spectral ranges of each ellipsometer and the studied parameter. Also, the dedicated software is *SpectraRay4* which is able to simulate, fit and measure data from the mentioned ellipsometers [18]. Finally, pictures of both ellipsometers are pesented in Figure 3.5.

Table 3.1: Overview of the spectral ranges and useful information provided by both ellispometers.

Model	**Spectral range**	**Useful information**
SENresearch 4.0	190 nm (deep UV) to 3,500 nm (NIR)	Thickness n & k coefficients
SENDIRA (FTIR)	400 cm^{-1} to 6000 cm^{-1} (1.7μm - 25μm) (IR)	Molecular content n & k coefficients

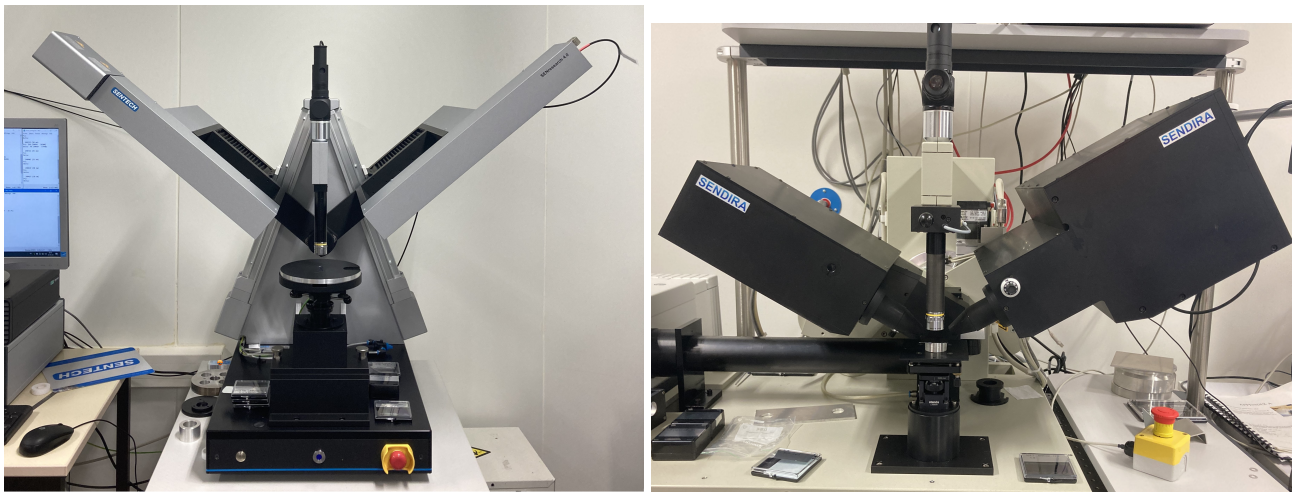

(a) UV-VIS-NIR. (b) IR.

Figure 3.5: Pictures of the used ellipsometers.

3.3 Four-point probe

The 4PP technique is used to get the resistivity of a material. The resistivity ρ can be obtained from the resistance R and the geometry of the sample. Knowing the voltage difference V and the current intensity I, R can easily be found from the basic formula

$$R = \frac{V}{I}. \tag{3.8}$$

A way to determine R experimentally is to simply pass a current through the material and get the ratio between the current I and the applied voltage V.

However, if only two probes are used, the obtained resistance value is most of the time incorrect. This is because the contact resistances R_c at the position of the probes are intrinsically included and in series with the one of the samples. Thus, a system of four probes is usually used, determining the voltage difference at another place [58]. Figure 3.6 illustrates the general principle.

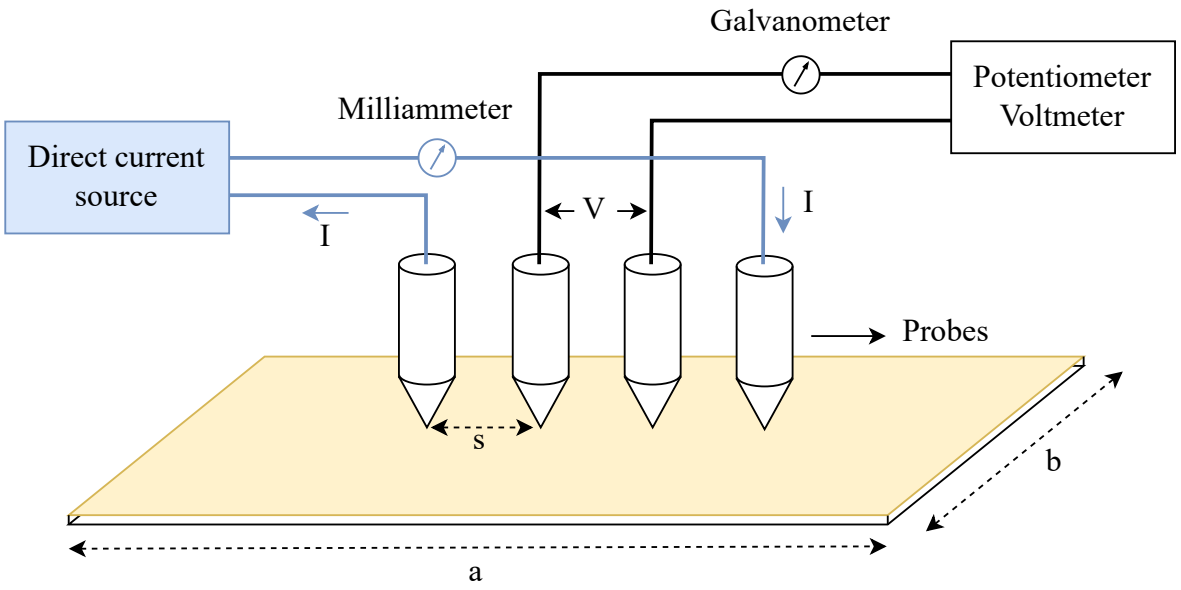

Figure 3.6: 4PP basic setup [58].

In the case of the 4PP, the potential is measured with the central probes, the external probes acting like a dipole on the sample. The resistivity is then determined by considering some correction factors based on the geometry of the sample and the proximity of the probes with respect to the borders.

Following notations of Figure 3.6, the sheet resistivity of a rectangular slice with a thickness $t \ll s$ is given by [50]

$$R_{\text{sheet}} = R_1\left(\frac{b}{s}, \frac{a}{b}\right) \cdot \frac{\pi}{\ln 2} \cdot \frac{V}{I} = 4.5324 \cdot R_1\left(\frac{b}{s}, \frac{a}{b}\right) \cdot \frac{V}{I}\,. \tag{3.9}$$

This correction factor is used to correct sheet resistivity results given by the instrument, which is considering an infinity large thin plate for its internal calculations, i.e. $R_1 = 1$. For each sample, R_1 is obtained by interpolating empirical data given in the literature [56].

A photograph of all samples is shown in Figure A.1. Additionally, the correction factor applied for each sample from its dimensions and empirical data interpolations is detailed in Table A.2. The final result given by the device is the sheet resistance, given in Ω/sq. Then, to obtain the bulk resistivity, this value should be multiplied by the thickness in cm, to generally have a result in $\mu\Omega$·cm. The 4PP offers a way to get the resistivity of the thin films. The instrument used for the measurements is the *Jandel RM3-AR Test Unit*. A picture of the device is shown in Figure 3.7.

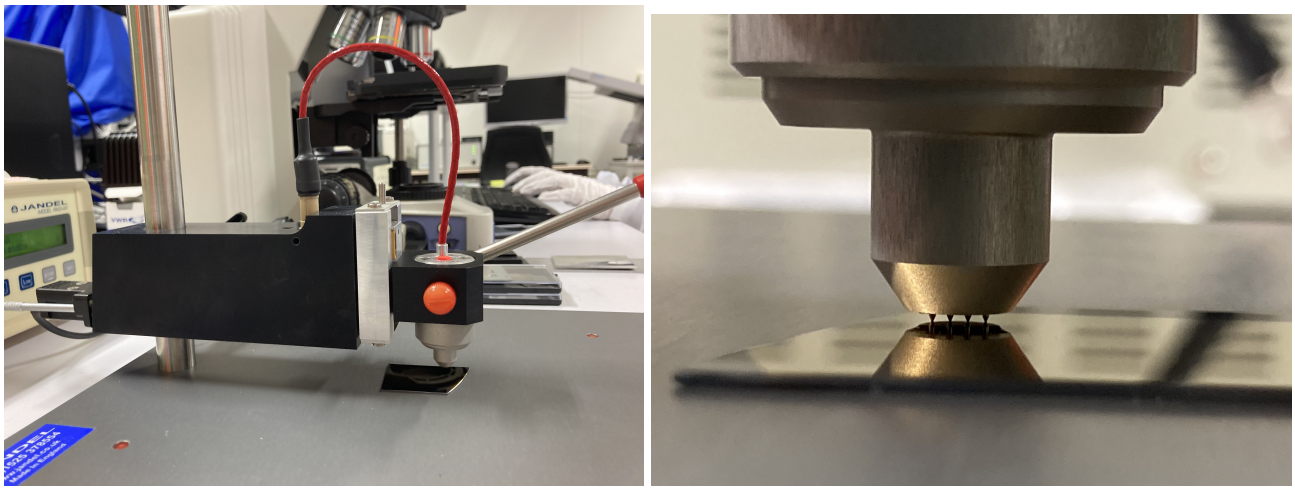

(a) 4PP. (b) Points in use.

Figure 3.7: Photograph of the 4PP.

3.4 Summary

To conclude, Table 3.2 indicates the useful information and the lab facility used for each characterization category.

Table 3.2: Characterization instruments and useful information.

Action	**Useful information**	**Used instrument**
Thickness determination	Thickness	Interferometric microscope UV-VIS-NIR Ellipsometer
Roughness analysis	Roughness	Interferometric microscope
Resistivity analysis	Sheet resistivity Free charges Thickness	4PP UV-VIS-NIR Ellipsometer
Optical analysis	n & k coefficients	IR Ellipsometer UV-VIS-NIR Ellipsometer
Molecular content analysis	Ψ & Δ	IR Ellipsometer

Chapter 4

Thickness determination

Contents

As mentioned, the thickness given by the QCM needs to be updated with more precise measurements. Used instruments in this section are the UV-VIS-IR ellipsometer and the interferometric microscope (profiler). First, an overview of the methodology is described. Then, the results are introduced and discussed.

4.1 Methodology

The methodology for the thickness determination and consequently the QCM calibration is illustrated in Figure 4.1. Once a sample is prepared, it is submitted to both ellipsometer and profiler measurements.

On one side, to be able to estimate the thickness with the ellipsometer, the experimental Ψ and Δ are compared to the Drude-Lorentz (DL) model available in the instrument database. From this model and after fitting the experimental data, the thickness is estimated. Correction factors for profiler measurements are also calculated. On the other side, measurements are done with the profiler and the correction factor is applied to finally have a second estimation of the thickness. After that, both methods are discussed, and a thickness estimation can be obtained.

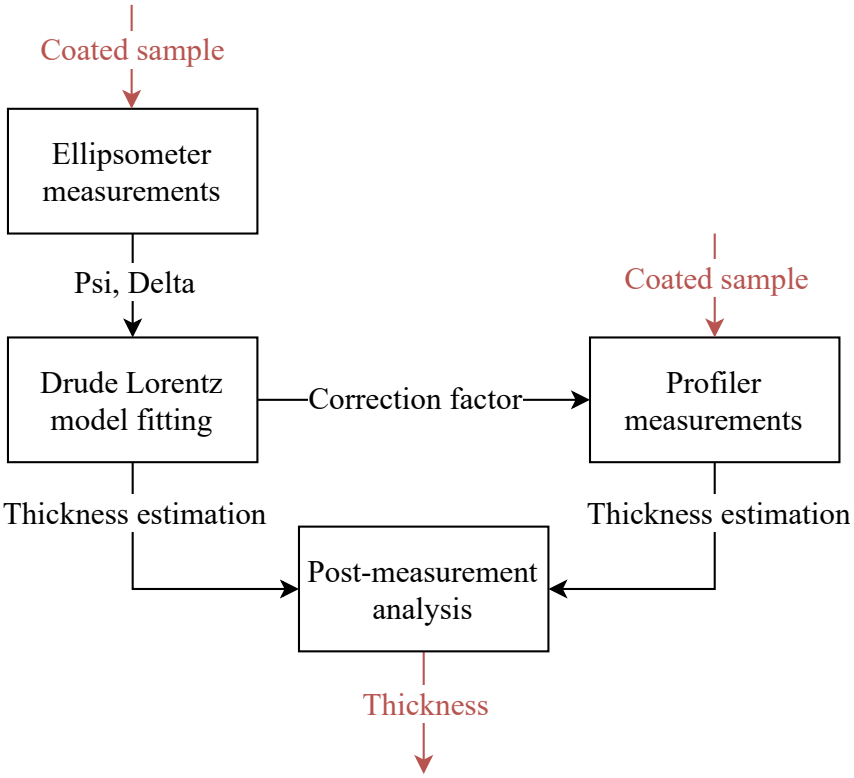

Figure 4.1: Thickness determination flowchart.

4.1.1 Ellipsometer measurements methodology

Measurements are done with the UV-VIS-IR ellipsometer in the maximum spectral range. The variation of (Ψ,Δ) with respect to the wavelength has been measured for all the samples. Measurement settings used for the spectroscopic ellipsometry are

- Max. spectral range, i.e. wavelengths from 190 nm to 3500 nm.
- Angle of incidence between 50° and 70°, step of 5°.
- 5 repetitions per measurement.

Once Ψ and Δ are known, the thickness is deduced. To do so, two methods can be used, each one involving a different model and different assumptions: the fitting directly from optically opaque data and the fitting from the theoretical DL model. These two methods are illustrated in Figure 4.2.

(a) Method 1. (b) Method 2.

Figure 4.2: Used models for the fitting of Ψ and Δ obtained with the UV-VIS-IR ellipsometer.

Method 1: fitting from the Drude-Lorentz (DL) model

In the *SpectraRay4* software, several materials are already available, including TiN. So the TiN layer (n, k) dataset can directly be used. This dataset is present in the form of a theoretical DL layer type.

The DL model assumes that the vibration of molecules in a material can cause resonances in its optical properties [18]. It can be described by the association of the dielectric function and the free charges contribution. The dielectric function is assumed to be the sum of Lorentz-oscillators, which are developed by representing an electron orbiting a massive, stationary nucleus as a spring-mass-damper system [30]. Mathematically, it gives

$$\varepsilon(\nu) = \varepsilon_1(\nu) + i\varepsilon_2(\nu) = \varepsilon_{1\infty} - \frac{\omega_p^2}{\omega^2 + i\omega_\tau \nu} + \sum_i \frac{\Omega_{p,i}^2}{\Omega_{0,i}^2 - \nu^2 - i\Omega_{\tau,i}\nu}\,, \tag{4.1}$$

where ε is the permittivity, ν is the wavenumber, ω_p and ω_τ are the strength and the damping of the free charge carriers contribution, Ω_p, Ω_0 and Ω_τ the strength, center frequency and damping of Lorentz-oscillators for each resonance and $\varepsilon_{1,\infty}$ the value of the dielectric function at infinite frequency. All these parameters are expressed in cm^{-1}.

Once the layer is integrated into the model, the fitting for each sample can be performed. When the theoretical curve is close enough to the experimental one, the resulting thickness is extracted.

Method 2: fitting from optically opaque data

This method assumes that the sample with the highest thickness, here sample 16, is thick enough to be optically opaque. First, the measured Ψ and Δ of the sample are converted to a material in *SpectraRay4*. The material contains the refraction index $n(\lambda)$ and the extinction coefficient $k(\lambda)$ for the whole spectral range (λ being the wavelength of the incident light). This (n,k) dataset is then integrated in the basic model like illustrated in Figure 4.2b. Instead of fitting experimental measurements from a theoretical model (method 1), the used reference is the optically opaque thin film model generated previously.

The only free parameter of this model is its thickness, so the fitting is done directly by varying the thickness of the optically opaque thin film to fit as accurately as possible experimental measurements of other samples. However, simulating the thickness variation implies a strong assumption that the structure of all thin films is the same as the one of the optically opaque one, which is not necessarily the case.

Finally, the measurement uncertainty determination is detailed in Appendix C.

4.1.2 Profiler measurements methodology

Concerning the profiler, measurements are only done by PSI to be as precise as possible. As a reminder, the goal is to get the 3D topography of the sample at a location where both the thin film and the substrate are visible separately. Having the height of the substrate surface and the height of the thin film surface leads to evaluate the thickness of the sample.

Measurement settings for the interferometric microscopy are listed below.

- Optical magnification: 20x.
- Numerical magnification: 1x.
- Post-process correction: Modal tilt only.

The observed sample may be tilted so the tilt correction is activated. Also, as mentioned in chapter 3, the refractive index of the substrate and the thin film are not the same and an additional correction factor should be applied to the thickness estimation.

4.2 Results and discussion

First, methods 1 and 2 are compared. It appeared during measurements that, with method 2, the optically opaque model was not fitting for intermediate and small thicknesses. A way to explain it is the existence of a molecular structure change depending on the prepared thickness. Also, one of the causes can be that sample 16 is still not optically opaque. Data should therefore be extracted from a thicker sample considered as optically opaque.

On the other hand, method 1 results in a much more accurate fitting even if some small differences are observed again for wavelengths over 1000 nm. This method is therefore used for the final thickness estimation from ellipsometer measurements. Thus, assumptions induced by the DL oscillator model are assumed. Ellipsometer measurements are shown in Table 4.1.

Samples 15 and 16 are not in the table because, as they begin to be optically opaque, the fitting attains its limits to estimate accurately their thickness, and their uncertainties are much larger than the ones obtained for thinner samples. In a general way, for measured samples, the estimated measurements uncertainty is quite stable.

Table 4.1: Experimental UV-VIS-IR ellipsometer thickness measurements summary.

Sample	t_{el} (nm)	
2	6.0	$\pm$ 0.1
3	10.5	$\pm$ 0.1
4	18.0	$\pm$ 0.1
5	30.5	$\pm$ 0.2
6	38.5	$\pm$ 0.3
7	42.5	$\pm$ 0.5
8	45.0	$\pm$ 0.6
10	52.0	$\pm$ 0.8
11	68.0	$\pm$ 1
12	81	$\pm$ 1
13	81	$\pm$ 1
14	94	$\pm$ 3

Concerning thicknesses obtained from the profiler, the calculated correction factor and the induced correction on the results are shown in Figure 4.3. This correction factor is obtained from an extrapolation of ellipsometer results, more detailed explanations are given in Appendix B. Then, the correction is applied to the initial estimation from the profiler.

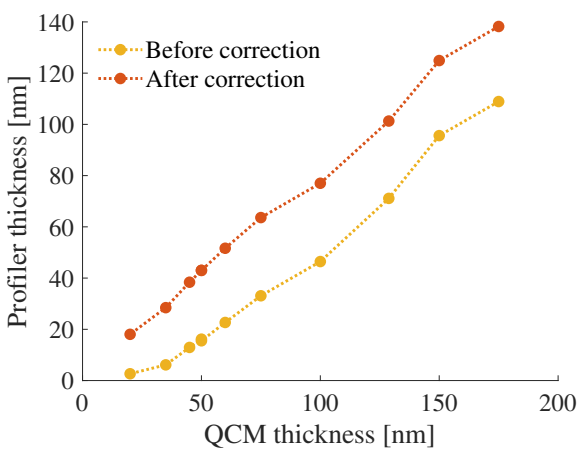

(a) Before/after correction.

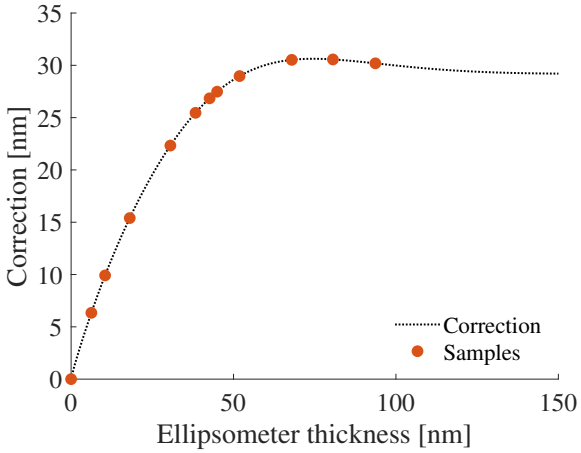

(b) Applied correction.

Figure 4.3: Effect of correction on the measured profiler thicknesses.

Final corrected measurements of the profiler are listed in Table 4.2 below. Here, samples 1, 2 and 3 thicknesses couldn't be obtained because of the interferometric microscope vertical resolution limitations.

Table 4.2: Experimental profiler thickness measurements summary.

Sample	**t_{pr} (nm)**	
4	18	$\pm$ 1
5	28	$\pm$ 2
6	38	$\pm$ 2.5
7	43	$\pm$ 3.5
8	43	$\pm$ 3
10	52	$\pm$ 3
11	64	$\pm$ 2
12	77	$\pm$ 3
13	79	$\pm$ 3
14	101	$\pm$ 2.5
15	125	$\pm$ 5
16	138	$\pm$ 3

4.2.1 Estimated thicknesses

Finally, thickness estimations can be compared together with the thickness estimated initially by the QCM, from Table A.1. The comparison is shown in Figure 4.4.

As a general observation, ellipsometer and profiler results are very close and seem to follow a linear tendency with respect to t_{qcm}. The assumption of a linear relation between them enables the possibility to do a linear extrapolation, which is useful for the QCM calibration. Additionally, uncertainties induced by profiler measurements are higher than the ones from ellipsometer measurements. Ellipsometer results seem to be more accurate for small thicknesses and the contrary can be observed from results with the profiler. For the final thickness estimation, the choice is made to consider the ellipsometer results for small thicknesses until a fixed threshold, from which the consideration switches to profiler results.

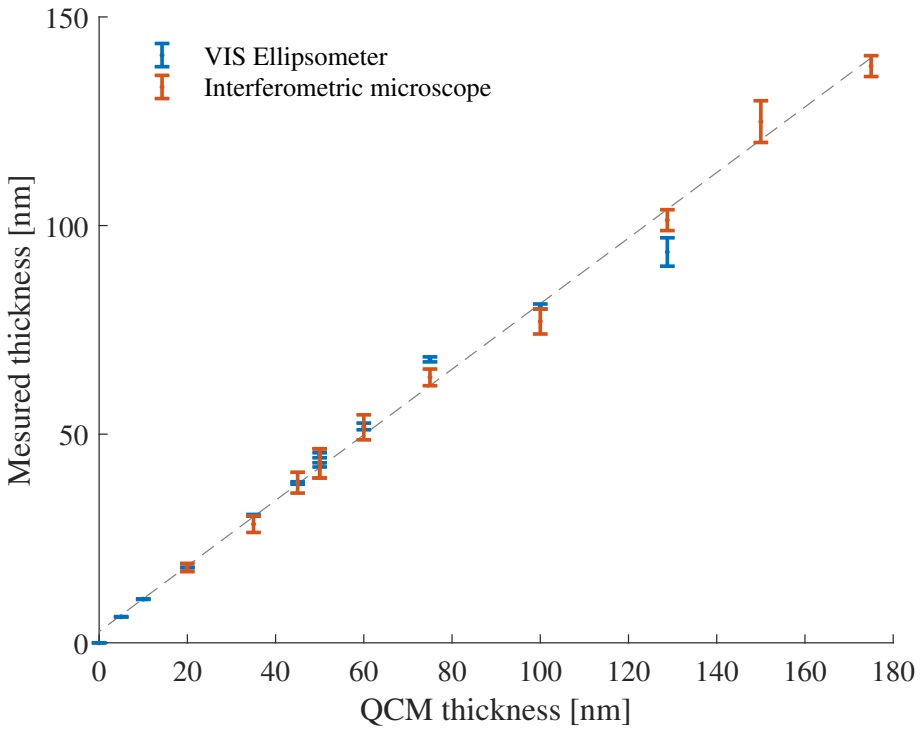

Figure 4.4: Comparison between thicknesses measured with the ellipsometer and the profiler with respect to the QCM thickness.

The selection of an optimal threshold value is thus necessary, it follows:

- Minimization of the distance between the Y-intercept of the linear extrapolation and the origin. This parameter can be an indicator of how close results are to reality. However, this is based on the linear relation assumption, which is already a simplification of what happen in reality.
- Minimization of the overall measurements uncertainty.

It is worth keeping in mind that this is one way to proceed and other methodologies are also possible. The selection converged to a threshold placed between samples 10 and 11.

In concrete terms, this means that the final estimated thicknesses are the ones measured by

- the UV-VIS-IR ellipsometer for samples thinner than sample 10 (included);
- the interferometric microscope for samples thicker than sample 11 (included).

A general graph is shown in Figure 4.5. As a complement, Figure 4.6 shows the final extrapolation and the variation of the Y-intercept with respect to the threshold position.

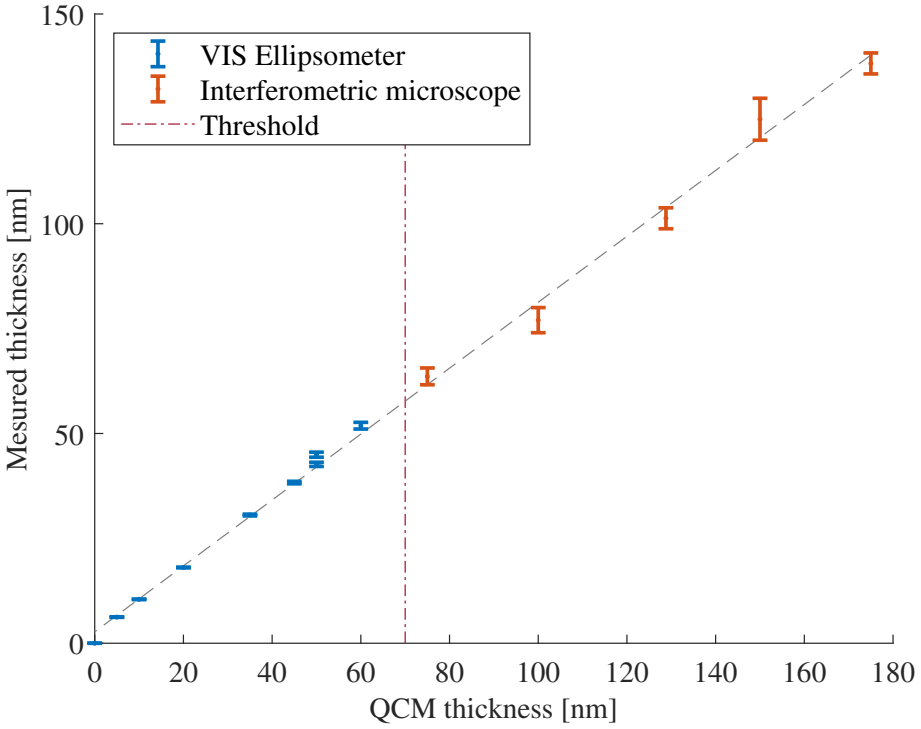

Figure 4.5: Final considered data after the threshold selection.

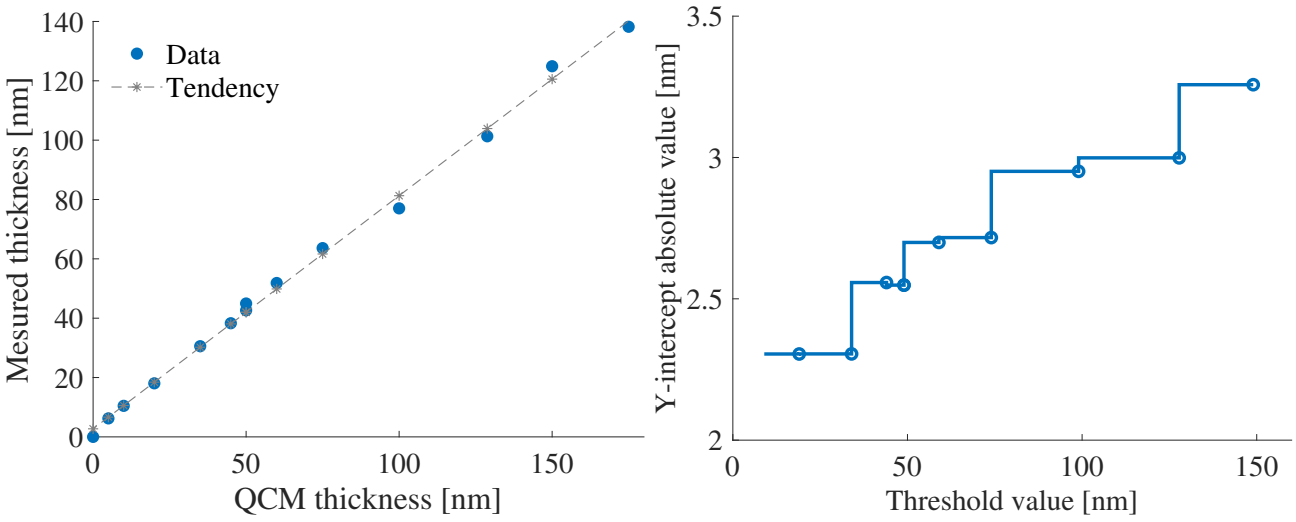

(a) Curve fitting based on the final chosen data.

(b) Y-intercept evolution with respect to the threshold.

Figure 4.6: QCM thickness study with respect to the threshold.

4.2.2 Deposition rate

Finally, from these final thicknesses, the deposition rate can be determined. This parameter is useful to characterize the deposition technique itself. Figure 4.7 shows the evolution of this deposition rate with respect to the thickness.

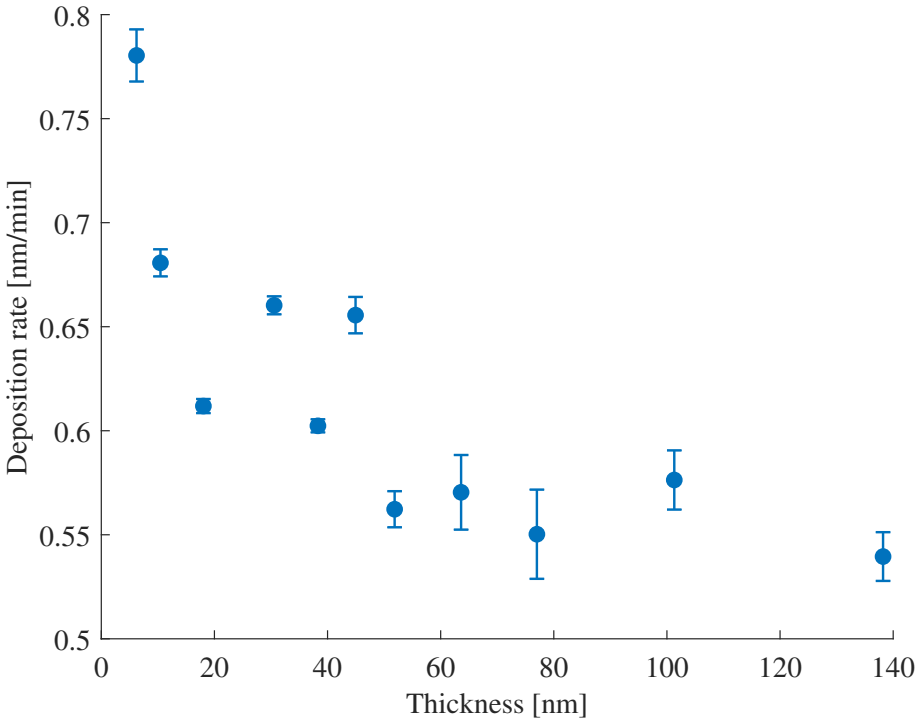

Figure 4.7: Deposition rate evolution with respect to the thickness.

First, this graph confirms that the deposition by IBS has a very low deposition rate compared to other techniques [1]. Also, there is a slight decrease of this rate with respect to the thickness of the sample to be prepared.

To conclude this section, sample thicknesses have been determined. First, the assumption has been made that the deposited thin films are acting like DL oscillators. From there, the thickness obtained by ellipsometry has been compared to the one obtained with the profiler. After a discussion about the legitimacy of each instrument depending on the sample thickness, it has been concluded that both results are used: ellipsometry for thinner films and profiler results for thicker ones. Finally, the deposition rates have been determined and it appeared that they were low compared to other techniques as foreseen. Table 4.3 contains all the final numerical data calculated through this section. These final thickness estimations are used as the basis of the sample characterization chapter in chapter 5.

Table 4.3: Final estimated thickness of each prepared sample, obtained from UV-VIS-IR ellipsometer (samples 1-10) and interferometric microscope (samples 11-16) measurements.

Sample	**t_{QCM}(nm)**	**Thickness (nm)**		**Dep. rate (nm/min)**	
1	0	-	-	-	-
2	5	6.0	$\pm$ 0.1	0.78	$\pm$ 0.01
3	10	10.5	$\pm$ 0.1	0.68	$\pm$ 0.01
4	20	18.0	$\pm$ 0.1	0.61	$\pm$ 0.005
5	35	30.5	$\pm$ 0.2	0.66	$\pm$ 0.005
6	45	38.5	$\pm$ 0.2	0.60	$\pm$ 0.005
7	50	42.5	$\pm$ 0.5	-	-
8	50	45.0	$\pm$ 0.6	0.66	$\pm$ 0.01
10	60	52.0	$\pm$ 0.8	0.56	$\pm$ 0.01
11	75	64	$\pm$ 2	0.57	$\pm$ 0.02
12	100	77	$\pm$ 3	0.55	$\pm$ 0.02
13	-	79	$\pm$ 3	-	-
14	130	101	$\pm$ 2.5	0.58	$\pm$ 0.01
15	150	125	$\pm$ 5	-	-
16	175	138	$\pm$ 3	0.54	$\pm$ 0.01

Chapter 5

Samples characterization

Contents

This section aims to investigate how electrical properties of TiN thin films change as a function of their thickness. This is the continuation of chapter 4, and thus, all the methodology related to the thickness determination is complemented by several characterizations: resistivity analysis, roughness analysis and optical properties analysis. An illustration of the general methodology for characterization, based on Figure 4.1 flowchart, is proposed in Figure 5.1.

First, the resistivity of each sample is analyzed with two complementary methods: from the 4PP and from ellipsometer measurements. The optical properties characterization is performed by ellipsometry. Moreover, the samples roughness is investigated using optical interferometry. Finally, a summary of all obtained results concludes this section. During the experiments, interesting changes have been observed for resistivities around 44 nm, not following the general tendency observed in literature.

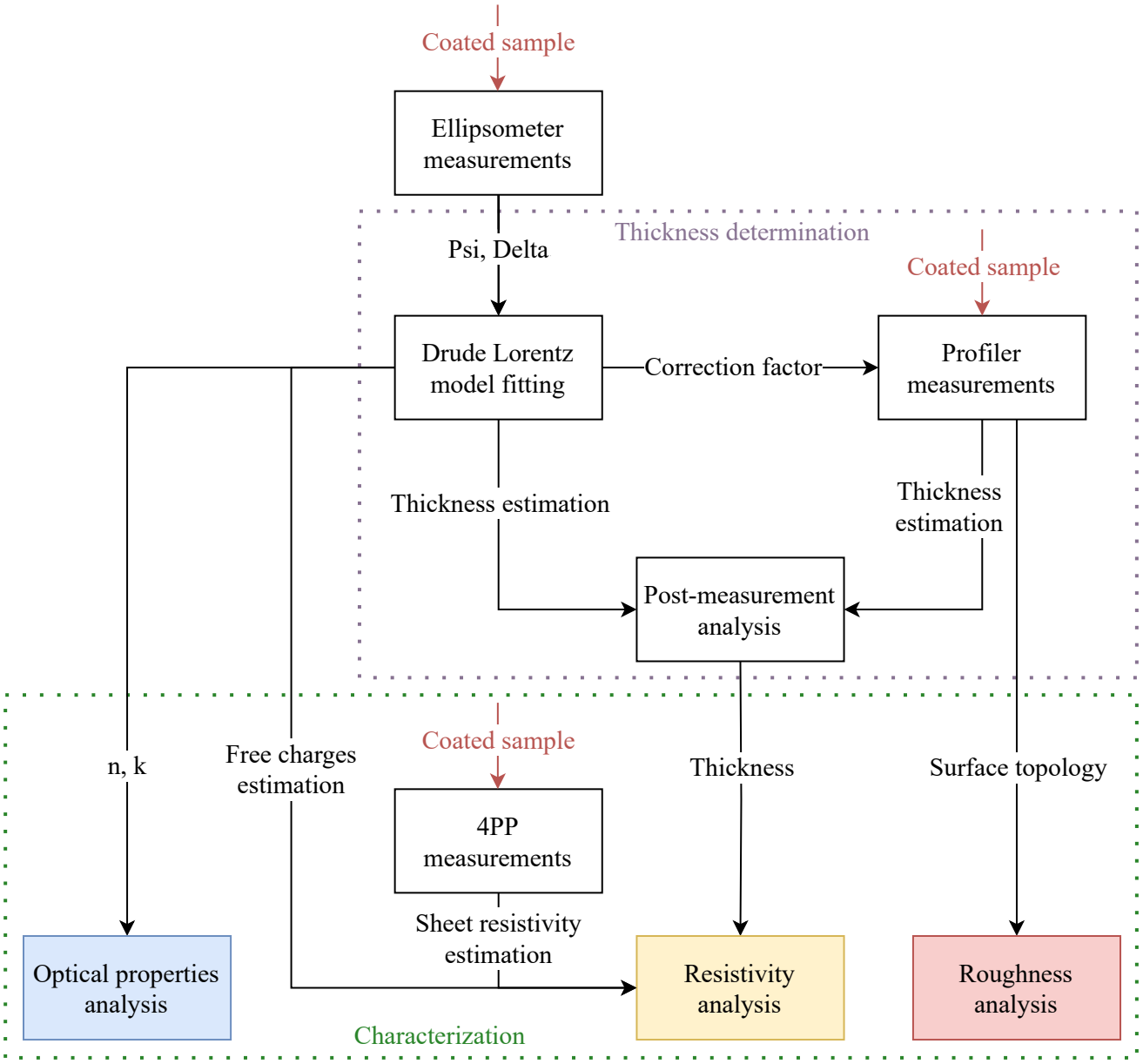

Figure 5.1: Sample characterization flowchart.

5.1 Resistivity analysis

The resistivity determination is based on 4-point probe (4PP) and ellipsometric measurements.

5.1.1 Methodology

The first way to obtain the resistivity of a sample is by getting the sheet resistivity from 4PP measurements $R_{\text{sheet, 4PP}}$ and to multiply it by the thickness t:

$$R_{\text{4PP}} = t \cdot R_{\text{sheet, 4PP}} \,. \tag{5.1}$$

Measurements with the 4PP all followed the same methodology, listed hereafter.

- 4 locations have been probed per sample.
- 3 different currents per location have been tested: from 0.1 to 30 mA depending on the sample thickness.
- 2 current directions (forward and backward).

In total, 24 measurements per sample have been made to get the sheet resistivity. The methodology regarding the uncertainty calculation is available in Appendix C. Additionally, the thickness having been determined with the DL oscillator model, assumptions mentioned in section 4.1.1 are applied.

From Equation 3.9, the correction factor $R_1\left(\frac{b}{s}, \frac{a}{b}\right)$ must be determined. The 4PP instrument assumes an infinite plate, and thus, $R_1 = 1$ [56]. However, measured samples are not infinite plates, and the assumption is made to have a thin rectangular slice. For each sample, the appropriate correction factor R_1 corresponding to their dimensions is considered. Computed correction factors are presented in Table A.2. Although they are not totally rectangular (see Figure A.1), the assumption is nevertheless more adapted to the situation.

Concerning ellipsometer measurements, the DL oscillator model is once again considered and thus assumptions related to it remain in application. The methodology is the same as the one indicated in section 4.1.1, but instead of extracting the thickness, the useful parameters are ω_p and ω_τ. From there, the resistivity is given by

$$R_{\text{el}} = \frac{\omega_\tau}{\omega_p^2} \cdot \frac{1}{2\pi\varepsilon_0 c} \,, \tag{5.2}$$

where ε_0 is the permittivity of free space and c the speed of light. The methodology concerning the uncertainty is also detailed in Appendix C.

5.1.2 Results and discussion

First, resistivities obtained respectively by the 4PP measurements and their corresponding uncertainty can be determined. These measurements are the ones assuming a thin rectangular slice. Second, they are compared to the ones obtained from the fitting of the UV-VIS-IR ellipsometer with the DL oscillator model. Table 5.1 summarizes these results.

Table 5.1: Experimental resistivity measurements.

Sample	**Thickness (nm)**	**R_{4PP} ($\mu\Omega$-cm)**	**R_{el} ($\mu\Omega$-cm)**
2	6	350 $\pm$ 3%	320 $\pm$ 5%
3	10.5	210 $\pm$ 4%	200 $\pm$ 4%
4	18	145 $\pm$ 2%	140 $\pm$ 4%
5	30.5	148 $\pm$ 3%	150 $\pm$ 3%
6	38.5	146 $\pm$ 1%	140 $\pm$ 2%
7	42.5	225 $\pm$ 2%	210 $\pm$ 2%
8	45	220 $\pm$ 3%	215 $\pm$ 2%
10	52	120 $\pm$ 4%	105 $\pm$ 1%
11	64	105 $\pm$ 5%	100 $\pm$ 2%
12	77	103 $\pm$ 5%	95 $\pm$ 2%
14	101	97 $\pm$ 4%	90 $\pm$ 1%
15	125	91 $\pm$ 5%	90 $\pm$ 1%
16	138	95 $\pm$ 3%	90 $\pm$ 2%

The first observation is that 4PP and ellipsometer both give very similar estimations of the resistivity. Regarding uncertainties, those of 4PP measurements are around 2-3%. In comparison, ellipsometer uncertainties are higher for thinner films and lower for thicker ones. The 4PP measurement may damage the samples by indenting the coating with the points. So, for completely non-destructive measurements, it might be indicated to use the ellipsometer. Results given by both techniques are also compared graphically in Figure 5.2.

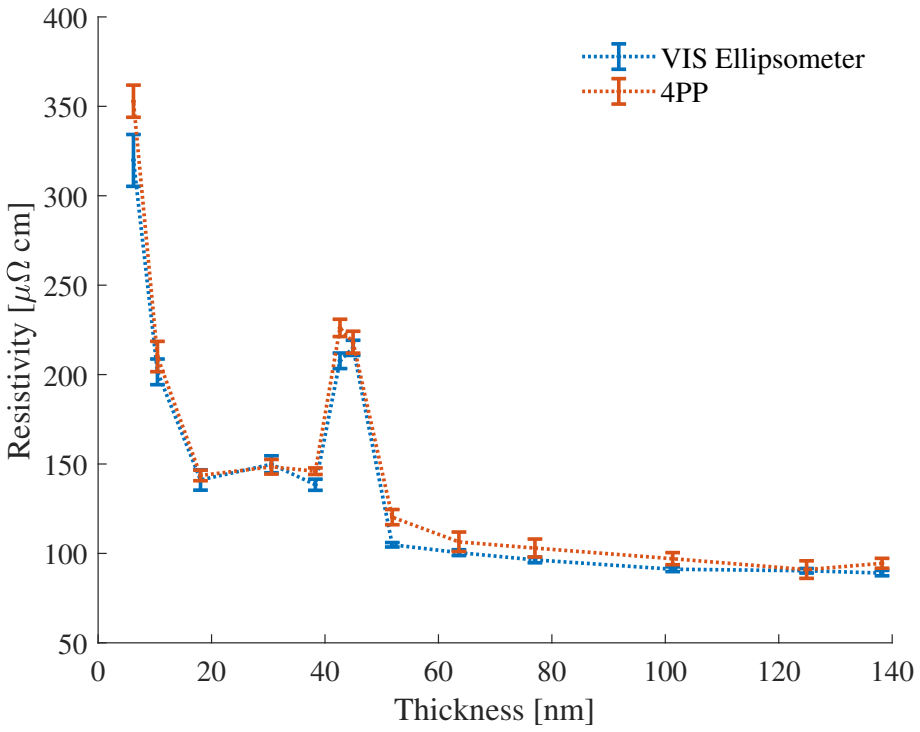

Figure 5.2: Evolution of the resistivity with respect to the thickness of the sample.

On one hand, the resistivity is decreasing with respect to the thickness of the sample. Resistivity changes in thin films may arise from electron mean free path changes [65]. This change has already been introduced in Figure 1.3a to highlight resistivity changes with the thickness of the sample. The explanation given in the context of this previous study was that, at some point, the resistivity decreases due to a lower roughness [66]: when the roughness increases, more electrons are scattered at the sample surface, leading to an increase of resistivity. The second component is the thickness increase itself: when more volume is involved, the mean free path of electron becomes larger, and this leads to lower resistivities. This effect is significant for very thin films up to a certain point where the electron mean free path converges to its bulk value. In our results, the resistivity converges to a value around 90 $\mu\Omega$·cm. This bulk resistivity enters in the same order of magnitude as the ones that can be found in the literature [6] [53] [66].

On the other hand, our results differ from the monotonous decrease of resistivity as function of thickness previously observed by the observation of a peak around 44 nm, where the resistivity is nearly doubled compared to the general trend. This peak is quite localized and is revealed by both 4PP and ellipsometry. An explanation behind this behavior can be the contribution of stress changes in the thin films depending on their thickness [60]. The formation of stress generally occurs during the deposition or growth of thin films. First, residual stresses originate from the mismatch between crystal lattice alignment of the thin film and its substrate. Additionally, there is a contribution from thermal stresses when a temperature gradient is applied due to a different CTE with the substrate. In this case, the effect of temperature is not studied. Finally, another stress evolution not related to lattice and thermal

mismatches can also be observed [60]. These stresses originate from the fact that depositions are made under non-equilibrium conditions. Generally, any redistribution of matter to find equilibrium will cause stresses in the film, since the thin film is retained by the substrate. These stresses are called intrinsic (or growth) stresses. Intrinsic stresses variation with respect to the thickness of the thin film is particularly interesting to introduce, as it is not linear. Its effect is shown in Figure 5.3.

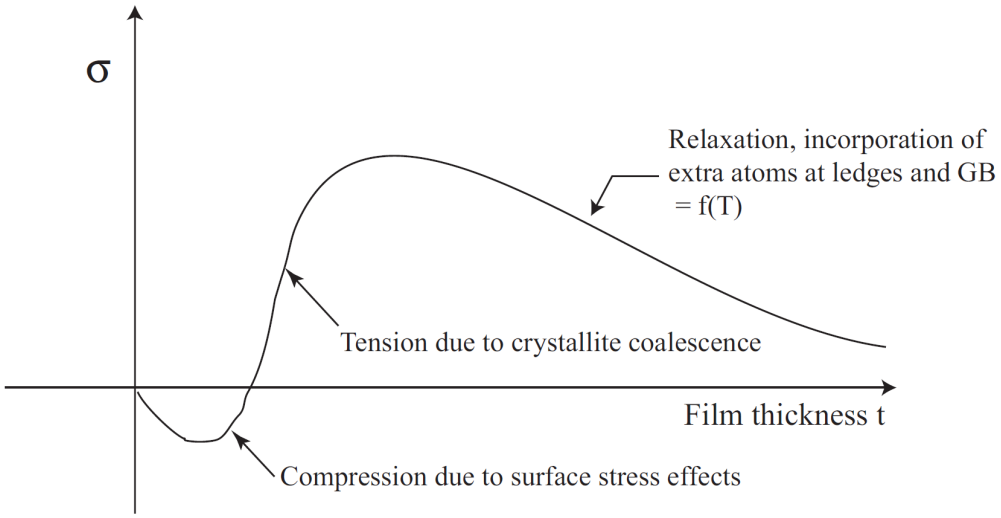

Figure 5.3: Evolution of the stress with respect to the thickness in thin films [60].

The curve shows that, for small thicknesses, there is a compression due to surface stress effects. Then, the stress switches from compression to tension until reaching a maximum tension at some point. This increase is due to the crystallite coalescence [39]. Finally, there is a relaxation and stresses decrease again.

One hypothesis explaining the apparition of a resistivity peak around 44 nm could be the intrinsic stresses transition. First, sputtered films have very large compressive stresses [60], so their influence can be significative. The strain induced by compression stresses have a tendency to bring TiN molecules closer : the electron mean free path decreases, and consequently the resistivity increases. After the resistivity maximum, the crystallite coalescence will have the effect of decreasing the resistivity. As shown in Figure 5.4, the gap between crystallites is closed and electrons are able to move more easily.

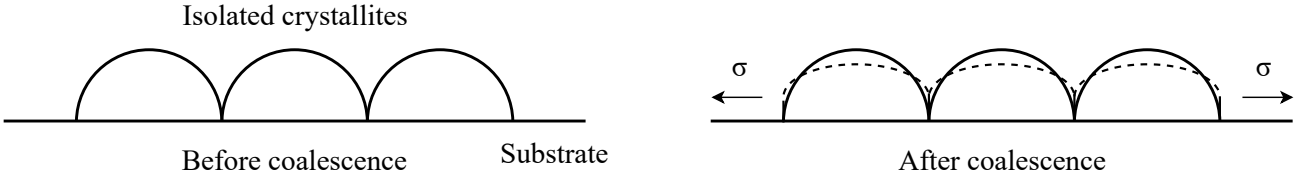

Figure 5.4: Crystallite coalescence illustration [60].

The free charge carrier strength ω_p of the DL model gives complementary information concerning the charge carrier density in the thin film. It is given by

$$\omega_p = \sqrt{\frac{ne^2}{\varepsilon_0 m}}, \tag{5.3}$$

where n is the charge carrier density, e the charge, ε_0 the permittivity of free space and m is the mass of the electron. It can serve as a direct indicator of the square root of the charge carrier density in a solid [24]. Additionally, the free charge carrier damping ω_τ of the DL model gives information concerning the mean free path. It can be expressed with respect to the collision frequency f_{col} :

$$\omega_\tau = \frac{2\pi}{c} \cdot f_{\text{col}}\,, \tag{5.4}$$

where c is the speed of light. This means that when the value of ω_τ increases, the frequency of collisions will increase. Consequently, the electron mean free path will be smaller, leading to an increase in resistivity. The evolution of the free charge carrier parameters with respect to the thickness are displayed in Figure 5.5. As expected, there is a peak around 44 nm for both ω_τ and ω_p. Thus, from the examination of free charge parameters, the observed change in resistivity is attributed to both variations in the electron mean free path and the number of charge carriers.

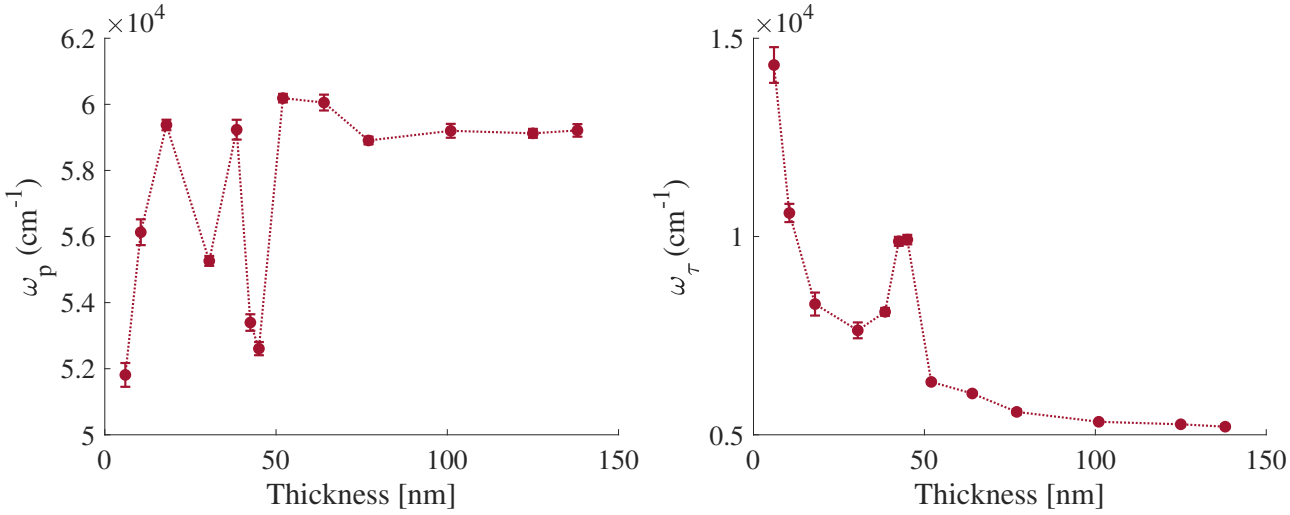

(a) Strength.

(b) Damping.

Figure 5.5: Variation of the DL free charge carrier parameters with respect to the thickness.

Final curves of Figure 5.2 are a combination of two tendencies:

- The general decreasing resistivity with respect to small thicknesses.
- The intrinsic stress changes in the thin film itself.

Here, all compared data refer to samples with a Si (100) substrate. Sample 9 (44 nm) being on MgF_2, it is interesting to determine if there is also a peak. Samples 7, 8 and 9 (all with thicknesses around 44 nm) resistivities measured with the 4PP are compared in Table 5.2.

Table 5.2: Sheet resistivity comparison between samples 7, 8 and 9 ($\sim$ 44 nm).

Sample	7	8	9
Substrate	Si (100)	Si (100)	MgF_2
$\mathbf{R_{sheet,\ 4PP}}$ **(Ω/sq)**	53	49	32

The substrate thus plays a role in the position of this peak. This consolidates the previously mentioned hypothesis. A resistivity depending on both general resistivity decrease and intrinsic stresses is the hypothesis to explain the observation. Further analysis with more samples and/or substrates would nevertheless be indicated.

Coming back to correction factors calculated to consider the thin rectangular slice assumption, Figure 5.6 shows its influence compared to the infinite plate assumption results.

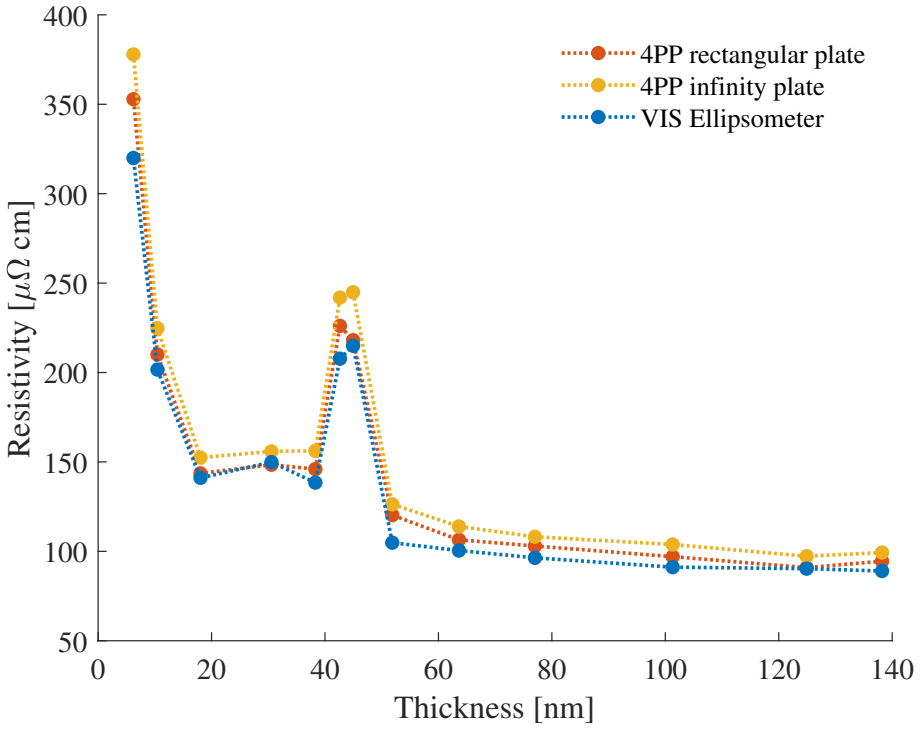

Figure 5.6: Effect of the thin rectangular slice hypothesis on the final results.

The final calculated resistivity by assuming a thin rectangular slice is clearly closer to ellipsometer measurements. As samples are not totally rectangular and measurements have not been made at the exact center, this assumption is however not perfect.

Conclusion

To conclude the resistivity analysis, among all measured resistivities, there was the observation of a peak around 44 nm. Except for this peak, the resistivity is decreasing with thickness down to a convergence value of approximately 90 $\mu\Omega$·cm. This behavior has been discussed and a probable physical explanation is the change in the electrons mean free path coupled to a change of charge carrier density due to intrinsic stresses variation.

5.2 Optical properties analysis

It is also interesting to analyze the evolution of optical properties with respect to thickness. In this part, the behavior of the refractive index n and the extinction coefficient k are presented.

5.2.1 Methodology

As for the thickness analysis and the resistivity analysis, the n and k are determined from ellipsometric measurements by assuming a Drude-Lorentz (DL) oscillator model. Also, the real and imaginary parts of the dielectric function in Equation 4.1 are respectively given by

$$\varepsilon_1 = (n^2 - k^2) \text{ and} \tag{5.5}$$

$$\varepsilon_2 = 2nk\ . \tag{5.6}$$

In addition to the UV-VIS-NIR ellipsometer, measurements have been performed with an IR ellipsometer. The variations of (Ψ,Δ) with respect to the wavenumber have been measured for sample 16 (138 nm) considered to be optically opaque. Measurements settings used for the IR spectroscopic ellipsometry are:

- Max. spectral range, i.e. wavenumbers from 400 to 6000 cm^{-1}.
- Angle of incidence between 60° and 80°, step of 10°.
- 500 scans.

The methodology remains the same as the one used for all ellipsometer measurements and the DL oscillator model assumptions are still applied.

5.2.2 Results and discussion

It is first important to compare the measured (n, k) from the assumed optically opaque sample (sample 16, 138 nm) with the fitted DL oscillator model. The comparison is shown in Figure 5.7 for the UV-VIS-NIR ellipsometer. Measurements seem to fit relatively well with the DL model for wavelengths smaller than 1000 nm.

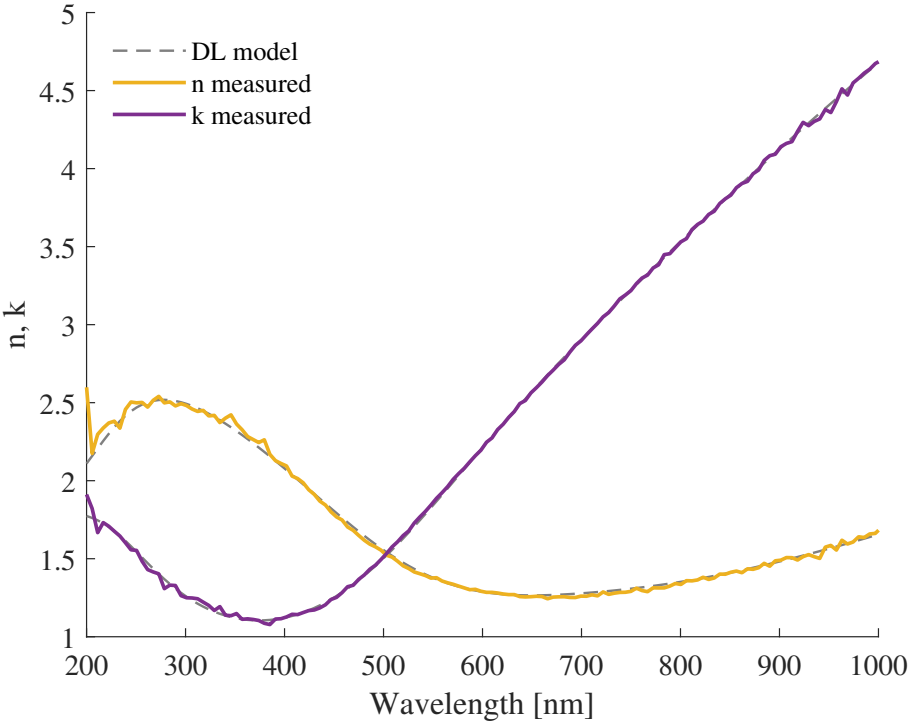

Figure 5.7: Comparison between experimental (n, k) coefficients and the corresponding DL fitting for UV-VIS-NIR ellipsometer measurements of the optically opaque sample (sample 16, 138 nm).

Concerning IR ellipsometer measurements, shown in Figure 5.8, results are fitting with the DL model until wavelengths of 10 μm, corresponding to a wavenumber of 1000 cm^{-1}. Then, measurements start to diverge. These results are certainly no longer valid for $\nu \geq 10\mu m$. Two hypothesis are possible :

- The wavenumber at which the divergence starts is near the one for which Ti-N molecular bonds are oscillating. In literature, this characteristic wavenumber is around 1035 cm^{-1} [67] [22]. In contrast, the DL oscillator model does not consider molecular dipoles. Therefore, additional Lorentz oscillators would have been needed to get accurate theoretical results.
- Measurement inaccuracies due to an ineffective angle configuration and/or a low number of scans. An optimization of the angles and more scans would have been needed to get accurate experimental results.

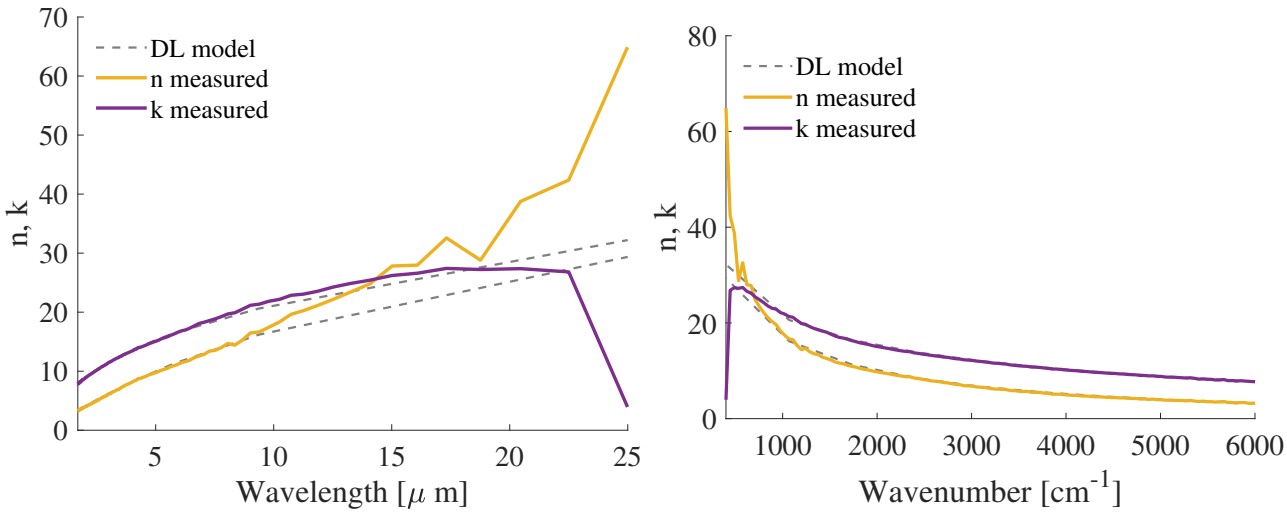

(a) Wavelength.

(b) Wavenumber.

Figure 5.8: Comparison between experimental (n, k) coefficients and the corresponding DL fitting for IR ellipsometer measurements of the optically opaque sample (sample 16, 138 nm).

First, variations of (n, k) and (ε_1, ε_2) with respect to the wavelength are extracted from the DL model fittings of chapter 4. Figure 5.9 and Figure 5.10 show these variations for 6 different samples. In addition, the variation of some characteristic points is presented.

For instance, the wavelength at which the intersection between n and k is occurring is interesting because it corresponds to the point cancelling the real part of the dielectric function, i.e. the point where $\varepsilon_1 = 0$. This relation is presented in Figure 5.11a for several thicknesses. The variation of k with respect to this wavelength is also presented in this figure. There is the apparition of a small peak for the same samples as for the resistivity peak, around 44 nm. Otherwise, the general tendency is a decrease of the wavelength. Variations become more significative for small thicknesses, here for thicknesses lower than 20 nm. This region could therefore be interesting to analyze in more details by preparing more samples within this range. After the aforementioned peak, variations become less significative.

The wavelength at which the minimum of the extinction coefficient k_{min} is occurring is presented in Figure 5.12 for several thicknesses. The variation of k_{min} itself is also shown in this figure. There is no general tendency with respect to the thickness. However, an interesting decrease visible for thicknesses around the now well-known 44 nm region, for both ν (wavelength) and k_{min}.

The wavelength at which the minimum of the dielectric function imaginary part $\varepsilon_{2,\,\text{min}}$ is occurring is presented in Figure 5.13 for several thicknesses. The variation of $\varepsilon_{2,\,\text{min}}$ itself is also shown in this figure. The same behavior as the one described for k_{min} is visible for $\varepsilon_{2,\,\text{min}}$.

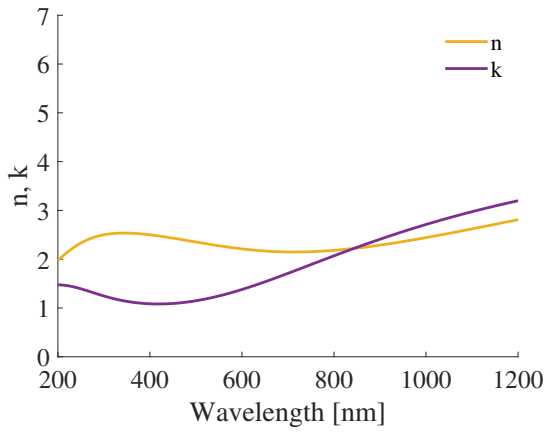

(a) Sample 2, 6 nm.

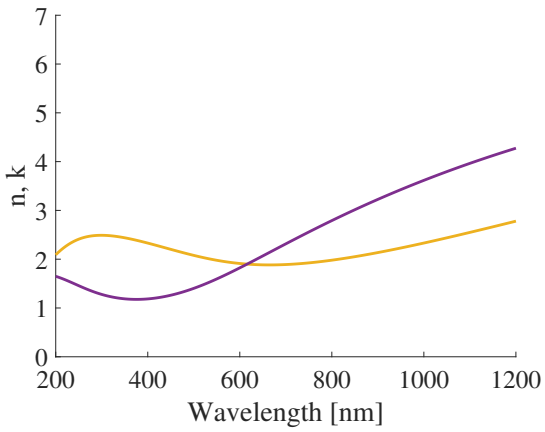

(b) Sample 3, 10.5 nm..

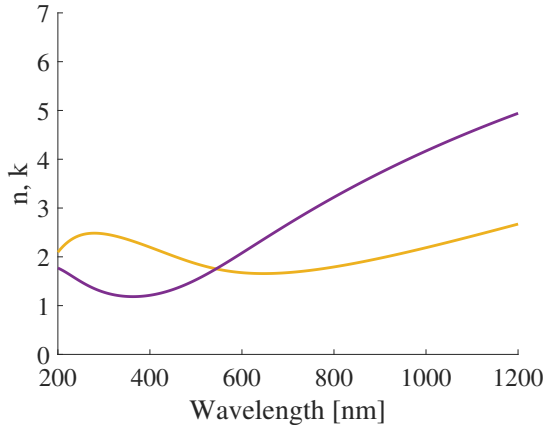

(c) Sample 4, 18 nm.

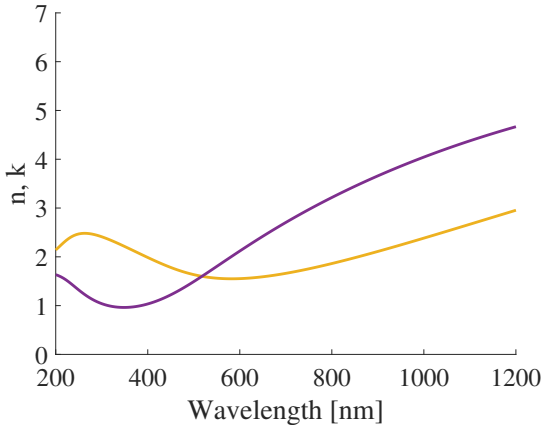

(d) Sample 8, 45 nm.

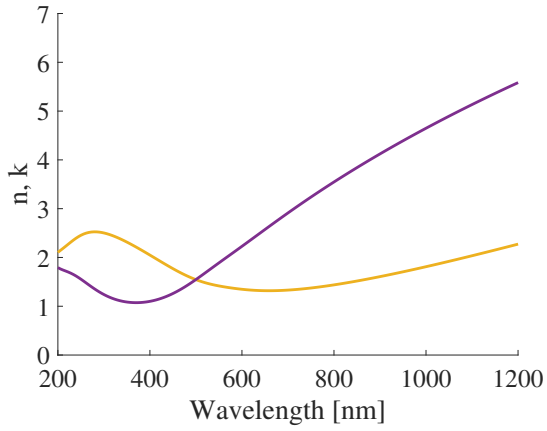

(e) Sample 11, 64 nm.

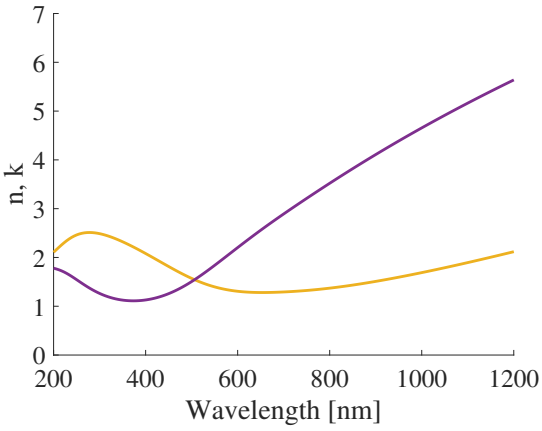

(f) Sample 14, 101 nm.

Figure 5.9: Evolution of n and k with respect to the wavelength for samples 2, 3, 4, 8, 11 and 14 using the DL model and obtained with the UV-VIS-IR ellipsometer.

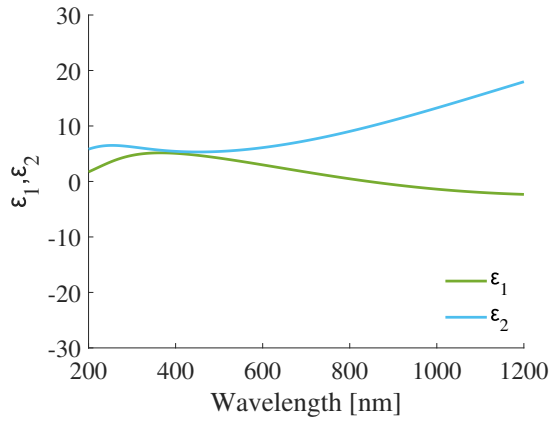

(a) Sample 2, 6 nm.

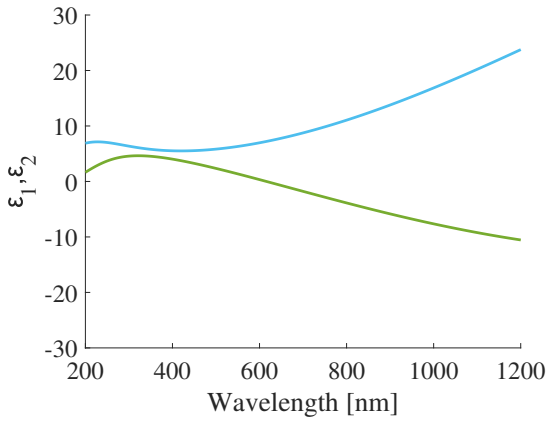

(b) Sample 3, 10.5 nm.

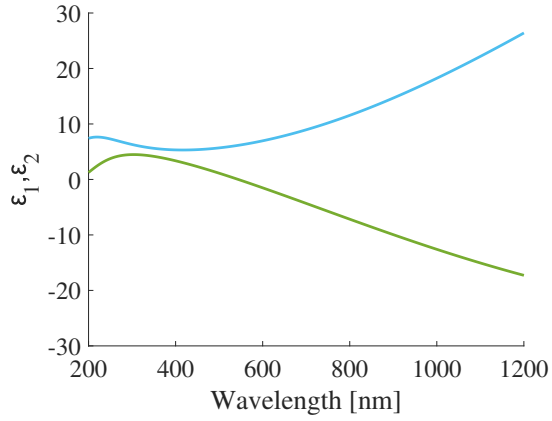

(c) Sample 4, 18 nm.

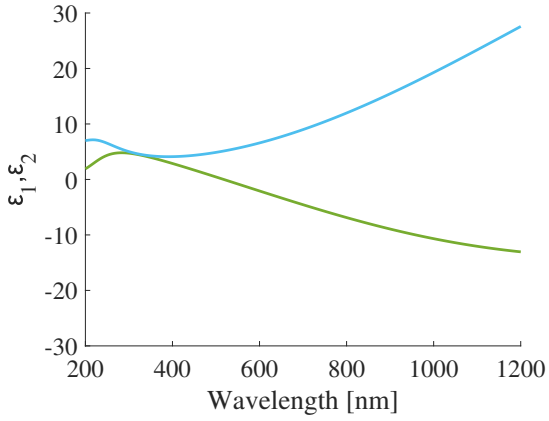

(d) Sample 8, 45 nm.

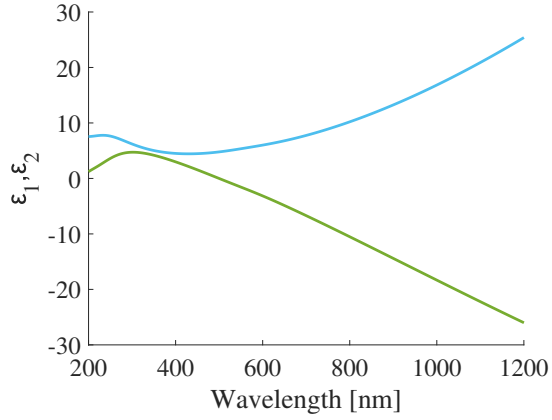

(e) Sample 11, 64 nm.

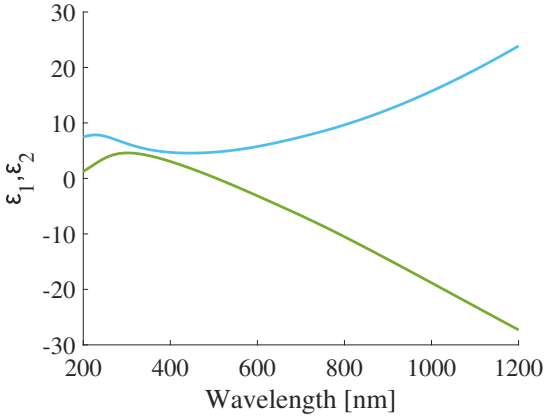

(f) Sample 14, 101 nm.

Figure 5.10: Evolution of ε_1 and ε_2 with respect to the wavelength for samples 2, 3, 4, 8, 11 and 14 using the DL model and obtained with the UV-VIS-IR ellipsometer.

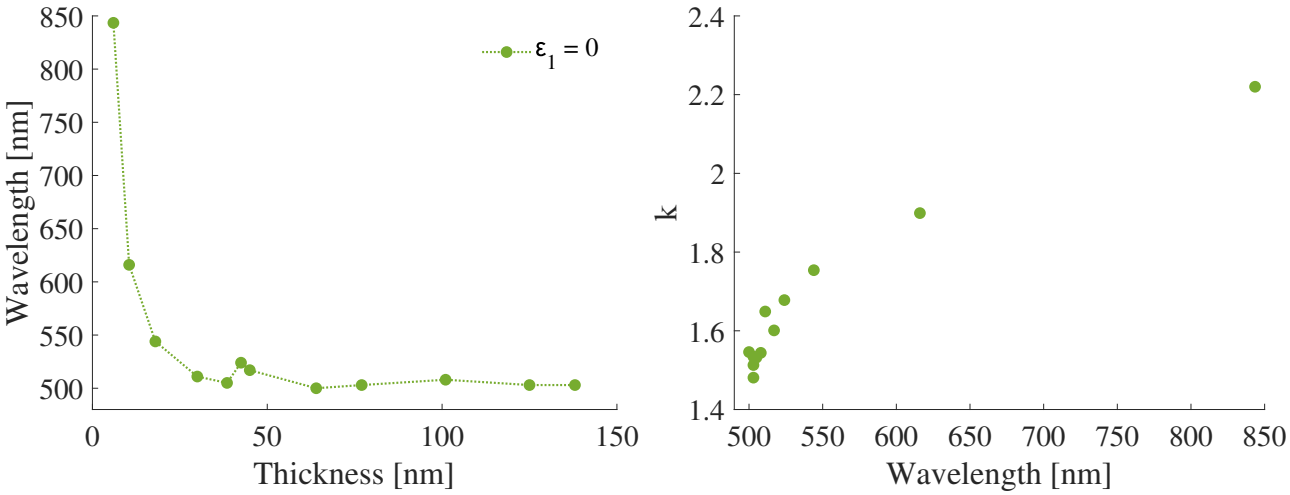

(a) $\varepsilon_1 = 0$ wavelength vs thickness

(b) k vs $\varepsilon_1 = 0$ wavelength.

Figure 5.11: Relevant tendencies involving the $\varepsilon_1 = 0$ intersection.

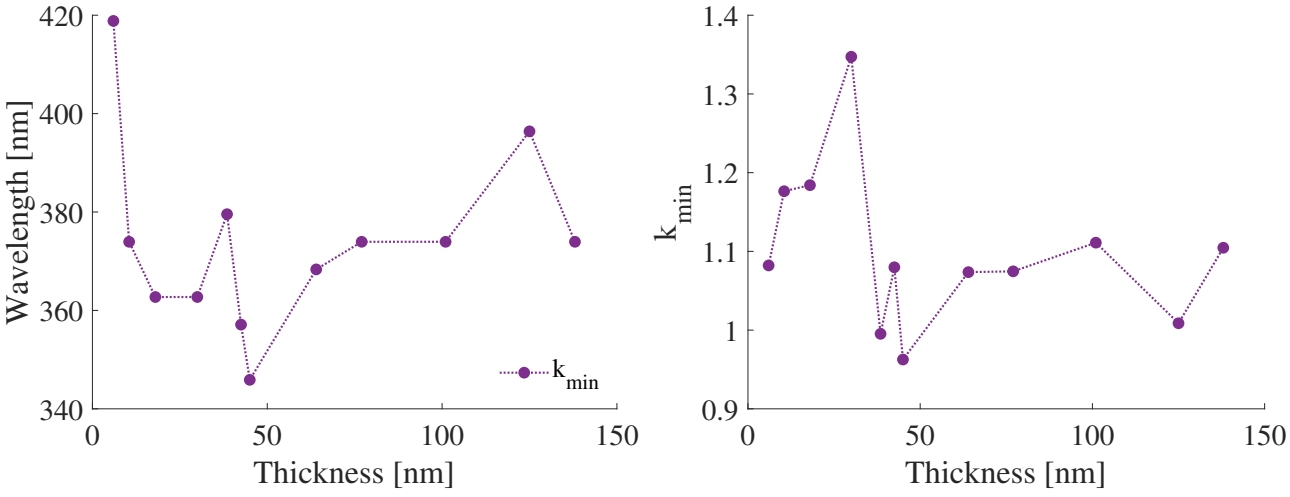

(a) k_{min} wavelength vs thickness

(b) k_{min} vs thickness.

Figure 5.12: Relevant tendencies involving k_{min}.

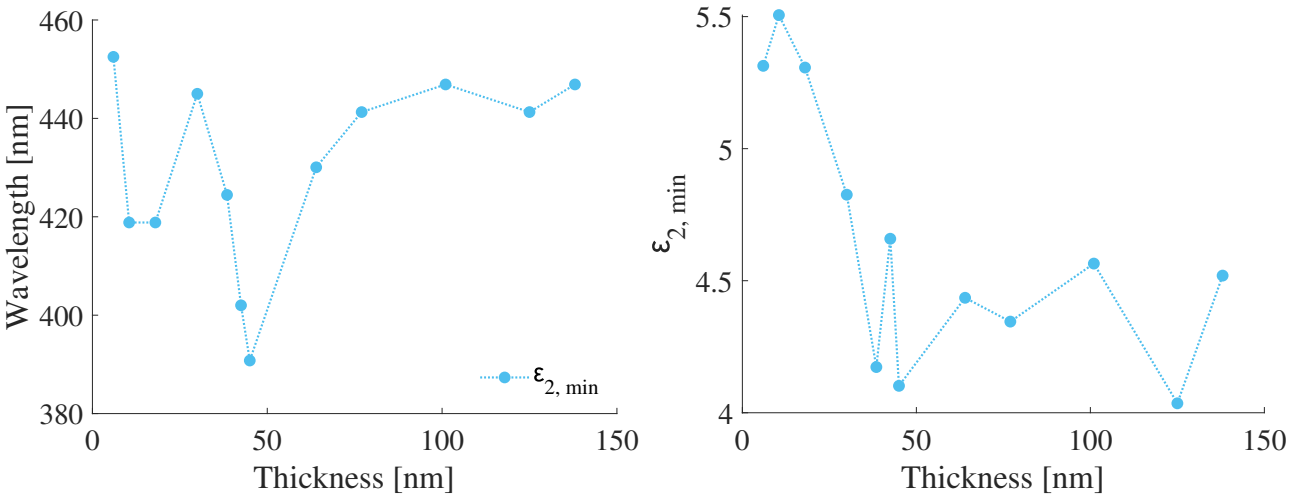

(a) $\varepsilon_{2,\,\text{min}}$ wavelength VS thickness

(b) $\varepsilon_{2,\,\text{min}}$ VS thickness.

Figure 5.13: Relevant tendencies involving $\varepsilon_{2,\,\text{min}}$.

Conclusion

To conclude, n and k are varying significantly with respect to the thickness. This means that, to determine their value, a study involving the thickness of the thin film must be performed. Bulk data is therefore not valid anymore for thin films.

5.3 Roughness analysis

The surface of a thin film may influence its electrical properties. As mentioned in section 5.1, roughness increase can lead to more scattering for the electrons [66]. Additionally, it helps to characterize the uniformity of the deposition. In the next paragraphs, the roughness results are presented and discussed.

5.3.1 Methodology

The analysis is made on 6 samples covering the entire thickness range. Measurements have been performed with the interferometric microscope. From the height variation $|Z(x, y)|$ in the analyzed surface, three relevant parameters are studied: S_a, S_q and S_z. S_a is the mean roughness and S_q the Root Mean Square (RMS) roughness, given by

$$S_a = \iint_{\text{Surface}} |Z(x, y)| dxdy \; . \tag{5.7}$$

S_z represents the average difference between the five highest peaks and the five lowest valleys.

Measurement settings for the interferometric microscopy are listed below.

- Optical magnification: 115x.
- Numerical magnification: 1x.
- Measurement area: 57μm x 42.7μm.
- Lateral sampling: 0.089 μm.
- Post-process correction: Cylinder and tilt.

The observed sample can be tilted and slightly curved, so cylinder and tilt corrections are activated. Measurements have been made for samples of 18, 45, 52, 77 and 138 nm. The roughness has also been determined for a Si (100) substrate. Three measurements are made for each sample at 3 locations.

5.3.2 Results and discussion

Roughness results are provided in Table 5.3.

Table 5.3: Roughness parameters for samples 4, 8, 10, 12 and 16 (from 18 to 138 nm).

Sample	**Thickness (nm)**	S_a **(nm)**	S_q **(nm)**	S_z **(nm)**
1	0	0.4 $\pm$ 0.2	0.5 $\pm$ 0.2	6 $\pm$ 3
4	18	0.4 $\pm$ 0.1	0.5 $\pm$ 0.1	7 $\pm$ 1
8	45	0.4 $\pm$ 0.1	0.5 $\pm$ 0.1	5 $\pm$ 2
10	52	0.4 $\pm$ 0.1	0.5 $\pm$ 0.1	6 $\pm$ 1
12	77	0.5 $\pm$ 0.1	0.6 $\pm$ 0.1	7 $\pm$ 1
16	138	0.4 $\pm$ 0.2	0.5 $\pm$ 0.2	6 $\pm$ 2

Concerning the variation with thickness, no significative changes are observed. This can also be because very thin films have not been investigated, the first one having a thickness of 18nm. These orders of magnitude are also reaching the instrument limitations, which can be the cause of inaccuracies. An example of measurement is shown in Figure 5.14.

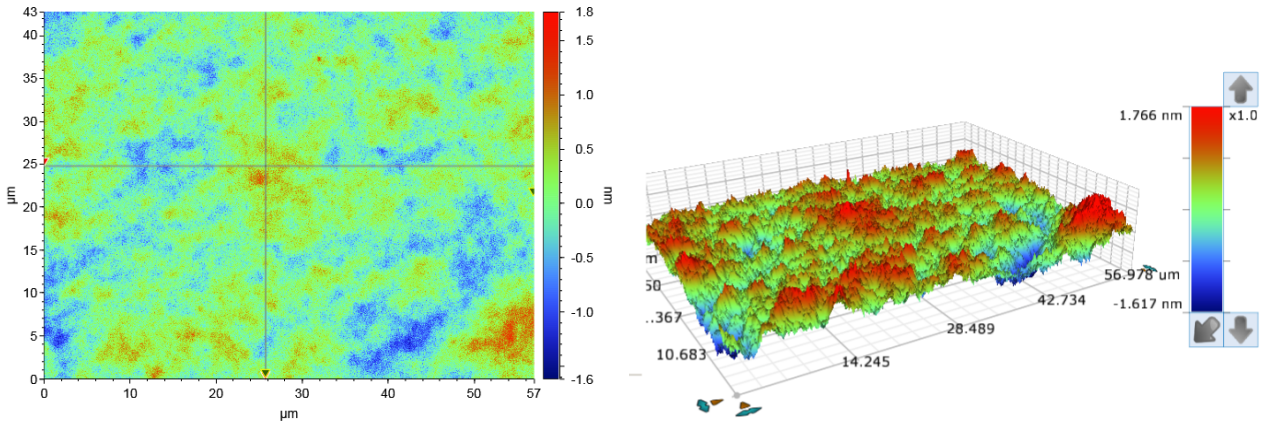

(a) 2D profile.

(b) 3D profile.

Figure 5.14: Example of a profiler roughness measurement (sample 8, 45 nm).

Assuming the roughness is not influenced by the thickness, an average S_a, S_q and S_z can be obtained independently of the studied sample. Computed parameters in this case are shown in Table 5.4. These values enter in typical TiN roughness that can be found in literature for similar preparation conditions and thicknesses [36].

Table 5.4: Overall roughness parameters.

Parameter	**Value (nm)**
S_a	0.4 ± 0.1
S_q	0.5 ± 0.1
S_z	6 ± 2

5.4 Results summary

One important result highlighted in this section is the observation of a resistivity peak for thicknesses of 44 ± 1 nm. Another relevant piece of information is that, except for the peak, the resistivity is decreasing with respect to the thickness. These results are explained by the combination of two phenomena: the electron mean free path increase with respect to small thicknesses and intrinsic stress changes in the thin film itself. Another interesting result is the correspondence between ellipsometer and 4PP measurements. Lastly, the resistivity is affected by the choice of the substrate, which will generate different stresses.

The analysis of optical properties also revealed some changes for samples having a thickness of around 44 nm. In the graph of the laser wavelength variation with respect to the point at which refraction and absorption are equal, a small peak appeared. Some high variations of the minimum absorptivity and the dielectric function imaginary part are also showing a transition at the vicinity of this thickness.

For thicknesses between 18 and 138 nm, no changes in roughness are observed. Therefore, at these thicknesses, the resistivity change is not due to a change of roughness. S_a, S_q and S_z have been computed and are respectively equal to 0.4, 0.5 and 6 nm in average.

Results obtained in this section are only available for thin films deposited over a Si (100) substrate by IBS but do provide information concerning the property changes with respect to the thickness in a general way. To go further in the analysis, more thicknesses should be investigated, more configurations with another substrate as well. Additionally, a study with respect to deposition conditions, for example by varying the nitrogen partial pressure in the thin film can be another way to continue the analysis.

To conclude this section, the analysis of the thin film/substrate model has been studied. The provided information is useful for the general knowledge of TiN thin films but also for the next step of microheater fabrication.

The remaining part to complete this work is the properties analysis of the prepared TiN track, which, in addition to thickness dependencies, can also vary with the transfer technique and its process parameters. As an alternative, all electrical properties measured in this work provide information concerning microfabrication by ablation of the thin film instead of transfer deposition.

Chapter 6

Track deposition and characterization

Contents

The goal of this section is the deposition and characterization of TiN tracks. One possible way to achieve this is by using LIFT. First, generalities concerning the technique are proposed. They are followed by a brief description of the lab facility used for LIFT in the CSL: the laser micromachining workstation. Then, the deposition method is briefly described. Finally, results are presented and discussed.

6.1 Laser-Induced Forward Transfer (LIFT)

These generalities include a description of the LIFT and other Additive Manufacturing (AM) techniques before diving in what are key parameters for the track deposition.

6.1.1 Other techniques overview

The terms "Additive Manufacturing", which basically encompasses all 3D printing methods, are quite wide and can be classified in several ways. Here is one possible classification: processes based on conventional photolithography (several steps) and digital printing (single step) [63]. On one hand, the

conventional photolithography (or optical lithography) aims to transfer a pattern to a substrate through a mask. Initially, the substrate is coated with a layer of photoresist. After that, it is exposed to light while a pattern mask is applied. Then, an etching is performed. The treated substrate is finally immersed in a developer solution, which removes the areas of the photoresist exposed to light.

On the other hand, digital manufacturing has a fabrication approach but also some functional structures and devices for which all the process can be done digitally [14]. The main advantage of this technique is that it is possible to work without masks, photoresist or etching, allowing to have a parallel design correction with fabrication. Also known as "direct-write process", digital manufacturing englobes dispensing, transfer, or printing of individual units of material called "voxels" (volumetric pixel) [44]. Finally, advantages of photolithography compared to direct-writing are better quality and better resolution [63].

Going further in direct-writing techniques, there are four main direct-write processes: dispensing, flow, particle beam and laser [44]. Table 6.1 provides a classification of its main mechanisms and working material. First, dispensing aims to deliver droplets of the material without any contact between the nozzle and the substrate surface while flow mechanisms are flowing continuously. Concerning particle beam mechanisms, they are defined as deposition techniques resulting on the interaction between a particle beam and the element to be deposited [16]. The last presented category regroups all mechanisms used with the help of a laser.

Table 6.1: Direct-write techniques mechanisms and working materials [44].

Process	**Mechanism**	**Materials**
Dispensing	Inkjet and electrohydrodynamic inkjet	Low-viscosity fluids
	Aerosol	All types
Flow	Tip (nScrypt) and Quill (MicroPen)	Pastes
	Dip-Pen Nanolithography (DPN)	Low-viscosity fluids
Particle beam	Focused ion beam (FIB)	Metals and oxides
	e-Beam	Metals
Laser	Micromachining	All types
	Laser Chemical Vapor Deposition (LCVD)	Metals and oxides
	Laser-Induced Forward Transfer LIFT	All types
	Laser-Induced Backward Transfer (LIBT)	All types

A laser beam can be used to modify, remove or transfer a part of the material of interest, initially deposited over a carrier substrate. Laser techniques all have in common to apply a very localized heating to the substrate. This has the advantage of achieving a greater resolution compared to other mechanisms. Also, using a laser allows dealing with solids, pastes and liquids. Concerning laser modifying, the material can be modified through different mechanisms such as sintering, micro stereolithography and multiphoton [62]. These methods are out of the scope of this master thesis; thus, the focus is made on remove and transfer mechanisms. An illustration of all different laser mechanisms is shown in Figure 6.1.

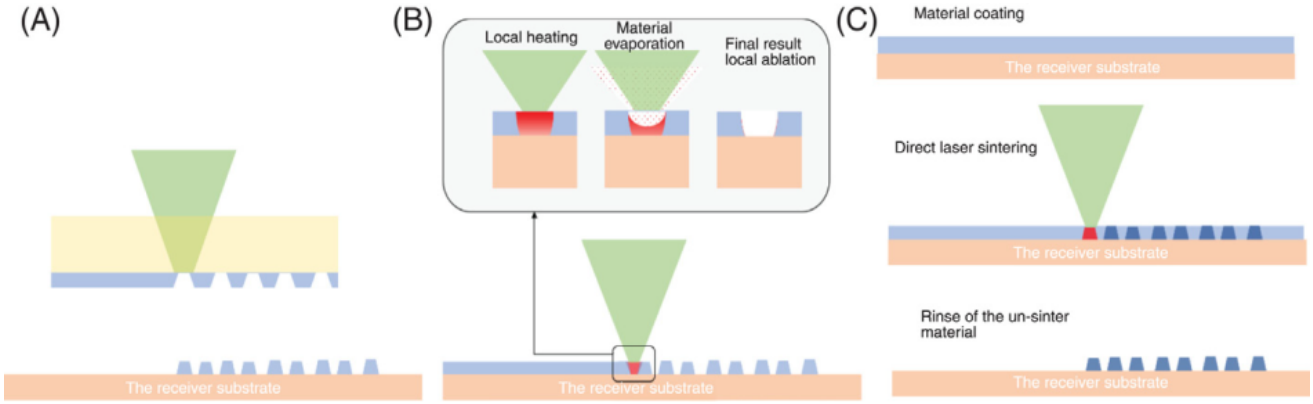

Figure 6.1: Laser printing methods: (A) Transfer, (B) Removal and (C) Modifying [63].

The removal can be performed with laser micromachining, which can be an athermal ablation, melting or evaporation (thermal). What is important for micromachining is the behavior of the material with the laser, which strongly depends on the wavelength or the pulse duration of the laser itself. Applications of laser micromachining can be found in the fabrication of precision fuel injectors or in the cutting and texturing of biomedical implantable parts [54].

Moreover, the transfer can be performed with laser additive microfabrication. The three most successful mechanisms are LCVD, LIFT and LIBT. The specificity of laser transfer mechanisms is the fact that the transferred material and the source of energy can be chosen without a lot of dependency between each other [44]. As a result, neither of these methods encounter problems like source material contamination, material delivery system blockages, or limited capability to print different material types, unlike other direct-write processes. LCVD is performed in a chamber with inlets for reagent gases. The focused laser beam then generates heat and consequently, there is material deposition on the substrate [57]. LIFT is the chosen mechanism to perform the deposition of TiN and is described in the next section.

6.1.2 Description

The Laser-Induced Forward Transfer (LIFT) printing aims to focus a laser beam on a constituted of a thin film and an optically transparent (to the laser) donor substrate. As the focus is at the interface between the thin film and the substrate, a micro-explosion happens and propels the material forward. The propelled material will then "land" on a receiver substrate, placed at a specific distance from the

donor substrate. The deposited material is called a "voxel" (volumetric pixel) and it can reach a volume of a few femtoliters [62] (for liquid applications).

In other words, the LIFT can be described with three main steps:

1. ablation of the donor film material from the donor substrate;
2. transfer of the donor film material at a certain velocity;
3. deposition of the material as a voxel on the receiver substrate.

Transfer velocities strongly depend on parameters such as the ejection mechanism, the material's properties or process parameters [10]. But, for solid LIFT, typical ranges of 200-1200 m/s can be attained [9]. The LIFT can be performed with or without a sacrificial layer, called the Dynamic Release Layer (DRL). It is mostly used when the thin film material needs to keep the same crystalline structure, when not having phase change is preferable. It is also necessary when the material is highly sensitive to thermal changes [12]. A representation of LIFT with and without DRL is shown in Figure 6.2.

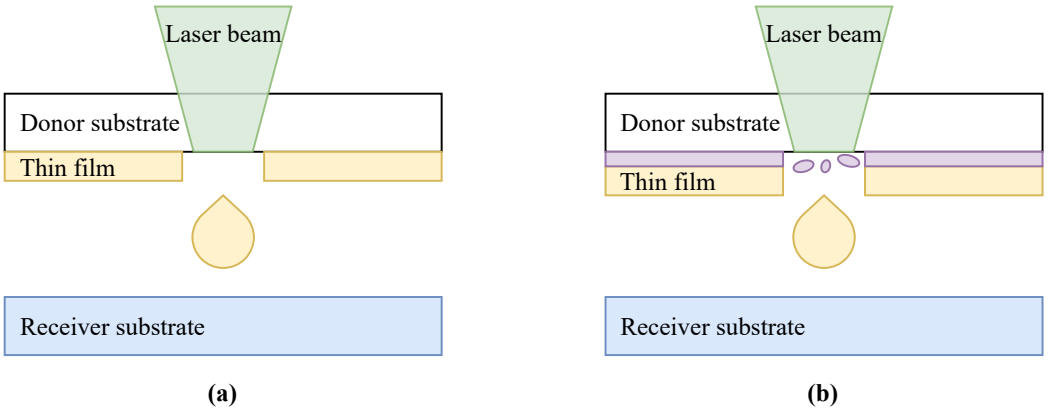

Figure 6.2: LIFT (a) without and (b) with a sacrificial layer [9].

There are several ways of classifying LIFT techniques. They can be sorted based on the interaction (direct, indirect, chemically induced), or the phase of the donor material (solid, paste, liquid). The second classification is used for the next paragraphs.

For solid layers, the initial material in the donor film absorbs the incoming radiation and is subsequently propelled towards the receiving substrate. This propulsion is due to a sudden increase of pressure and temperature locally. During the transfer, it is interesting to note that a shockwave is generated, which could be a problem for the deposition. For TiN layers, solid LIFT is usually performed [40].

Concerning liquid LIFT, even if the general principle is the same, there are some differences in the behavior of the donor layer. Also, some other relevant parameters must be considered like the liquid absorption energy or rheological conditions. Most liquid depositions are based on the formation of a

bubble where the laser is focusing, this bubble will then form a jet and the liquid layer is transferred to the receiver substrate [14]. The use of intermediate layer is also possible.

Finally, pastes are typically highly viscous, but not as viscous as liquids, and the paste LIFT is also known as Laser Decal Transfer (LDT). As pastes are not really affected by the deformation caused by the surface tensions, they follow the same shape as the one defined by the laser intensity. This allows "play" with the laser intensity to have the desired shape more easily than for solid and liquid LIFT [31]. To illustrate that, some measurements have already been performed with transferred silver nano-suspensions onto Si receiving substrates in Figure 6.3, for solid, liquid of paste depositions.

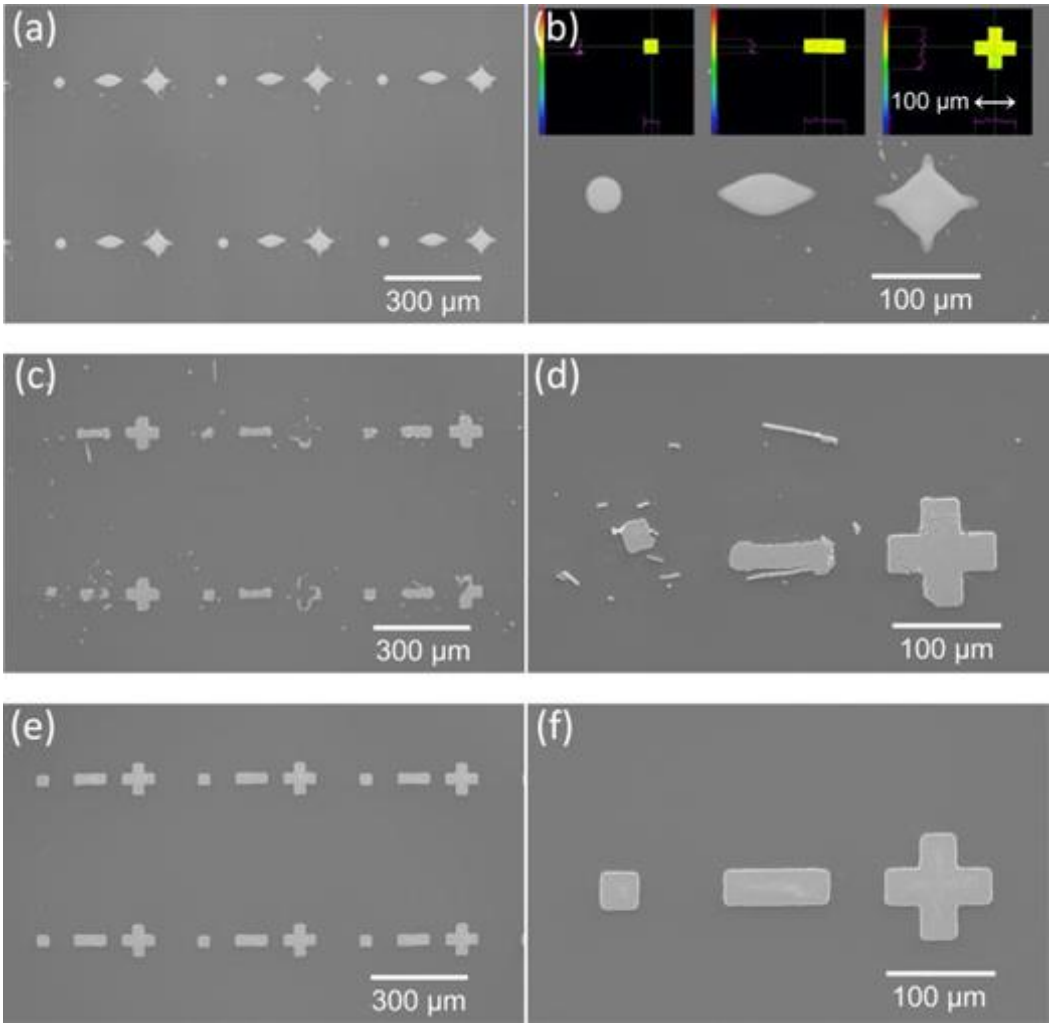

Figure 6.3: Comparison of three distinct viscosities for the deposition of silver onto a Si substrate. (a-b) Low viscosity "liquid-like", (c-d) Very High viscosity "solid-like", (e-f) High viscosity "paste-like" [31].

As a summary, the taxonomy of LIFT is shown in Figure 6.4. It is worth noting that this classification is not exhaustive, and is only one way to visualize AM techniques.

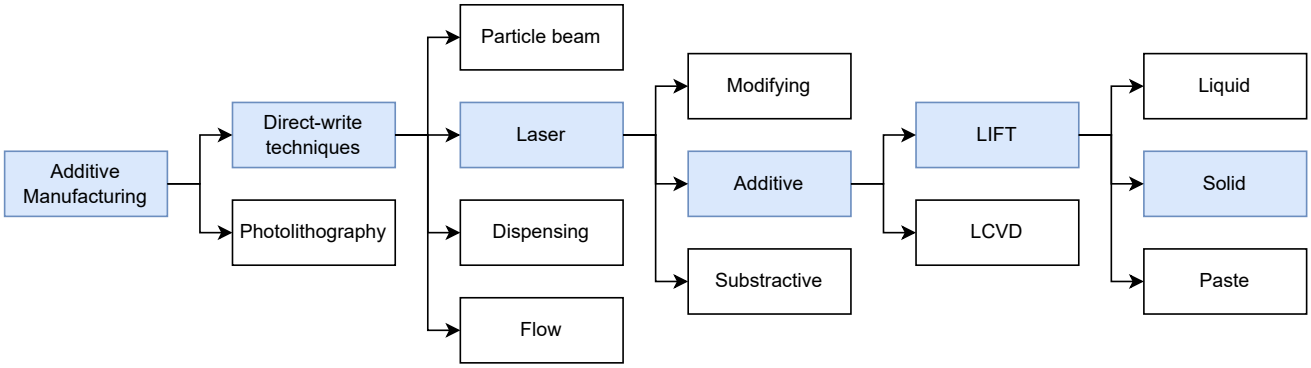

Figure 6.4: Taxonomy of the LIFT [44], [14], [63].

Normally, LIFT is performed with a pulsed laser, each pulse corresponding to one voxel deposition. However, recent studies showed that it is also possible to perform LIFT with several laser pulses [37][29] and even with a continuous laser source [52]. The latter works like a single pulse laser deposition but instead of having droplets, the deposited layer is continuous. A comparison between pulsed and continuous laser deposition is shown in Figure 6.5.

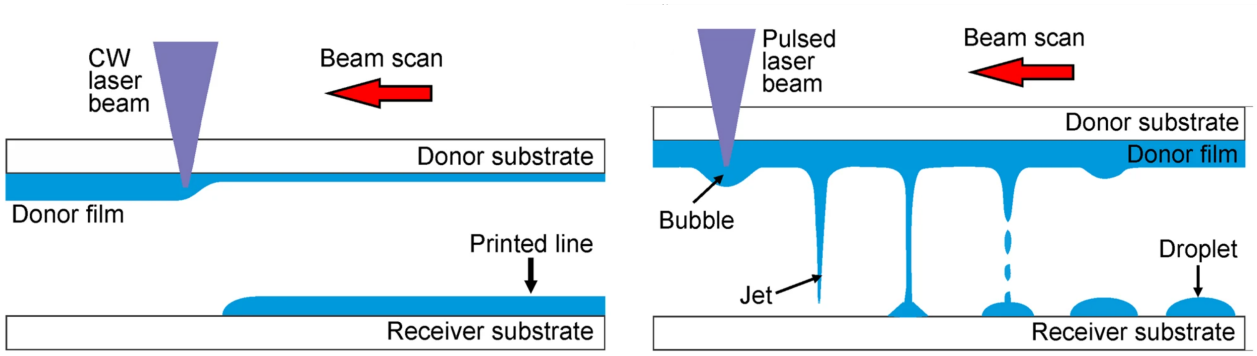

(a) Continuous wavelength.

(b) Pulsed.

Figure 6.5: Pulsed and continuous laser sources LIFT [52].

6.1.3 Important parameters and limitations

During the process, some parameters can be critical to get an effective deposition. According to Das A. at al. [9], important parameters are fluence (J/cm^2), the distance between the donor and the receiver (μm), the scan rate (mm/s) and the focal point of the laser beam, which is generally a great indicator of the beam diameter. The surrounding environment can also change results.

Fluence

The first parameter is fluence, which is defined by the expression:

$$\mathrm{F\ (J/cm^2)} = \frac{E_{\mathrm{pulse}}}{A_{\mathrm{foc}}}, \tag{6.1}$$

where E_{pulse} is the laser pulse energy (J) and A_{foc} is the effective focal spot area (cm^2). In fact, a balance is needed to get acceptable deposition results. Some tests have already been performed for a LIFT with a Ni donor (180 nm) and a gap between the donor and the receiver of $10\mu m$. These tests are shown in Figure 6.6.

At low fluences, the first picture clearly shows that the deposited material is not sufficient and fluence needs therefore to be increased. But although increasing fluence means that the ablation is increasing, at some point, this ablation will be too high. This phenomenon is shown in the third picture. There can also be some debris or thermal damage at high fluence. These problems are mostly due to an higher shock during the deposition, as the flyer velocity is linked with fluence [10]. In addition, higher velocities generated lead to having stronger impacts on the receiver substrate and thus a drop in quality. On the other hand, having lower velocities leads to some adherence problems between the voxel and the receiver. It is therefore important to find an optimum fluence to limit these effects and maximize the efficiency of the deposition.

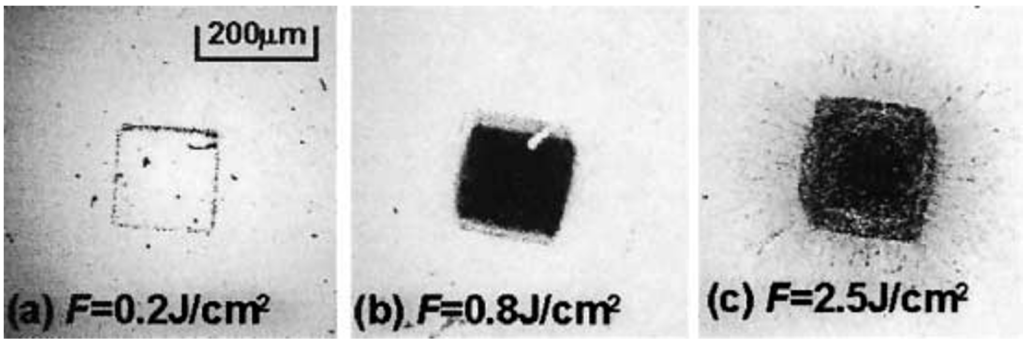

Figure 6.6: LIFT performed with Ni films results. (a) Low fluence, (b) Optimized fluence, and (c) High fluence [49].

Distance

Next, the distance between the donor and the receiver, denoted L, is also an important parameter. When this distance is larger, the efficiency of the projection tends to be lower. This efficiency is interpreted through the spread length and Figure 6.7 shows its dependency (d) with respect to L. In this example, Ni voxels are deposited with several fluences from 2 to 4 J/cm^2 and a thin film thickness of 180nm. An increase of d with respect to L is noticeable, this is because the voxel has more time to be spread for larger distances. Generally, when fluence is optimum, a higher accuracy is reached for small donor-substrate distances [61].

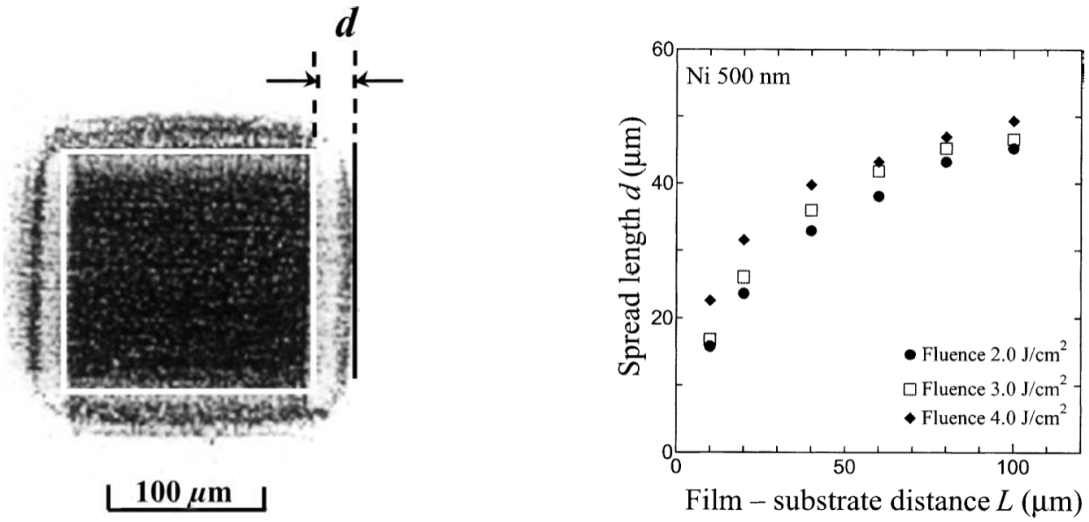

(a) Deposited structure.

(b) Relationship.

Figure 6.7: Evolution of the spread length with respect to the substrate distance for a given fluence [49].

Laser pulse duration

The choice of the laser influences the deposition. A first important laser parameter is the pulse, with ranges going from milliseconds (ms, long pulsed) to nanoseconds (ns, short pulsed) or even femtoseconds (fs) [64].

Both long and short pulsation lasers have advantages and drawbacks. Short pulsed lasers show a better ablation in the cost of a loss of adherence [64]. Examples of uses of ns lasers can be found in biological applications such as cells printing. The use of fs pulses lasers permits to be more precise and reduce the heating effects [26] [25]. Following the same logic, long pulsed lasers have more heat effects because the heated material is more exposed. Moreover, the energy distribution of the pulse itself can influence the deposition.

6.2 Laser micromachining workstation

The last instrument used in the scope of this work is a laser micromachining workstation using a UV excimer laser. The purpose of this instrument is to perform ablations and consequently LIFT or LIBT. An illustration of its general setup is shown in Figure 6.8.

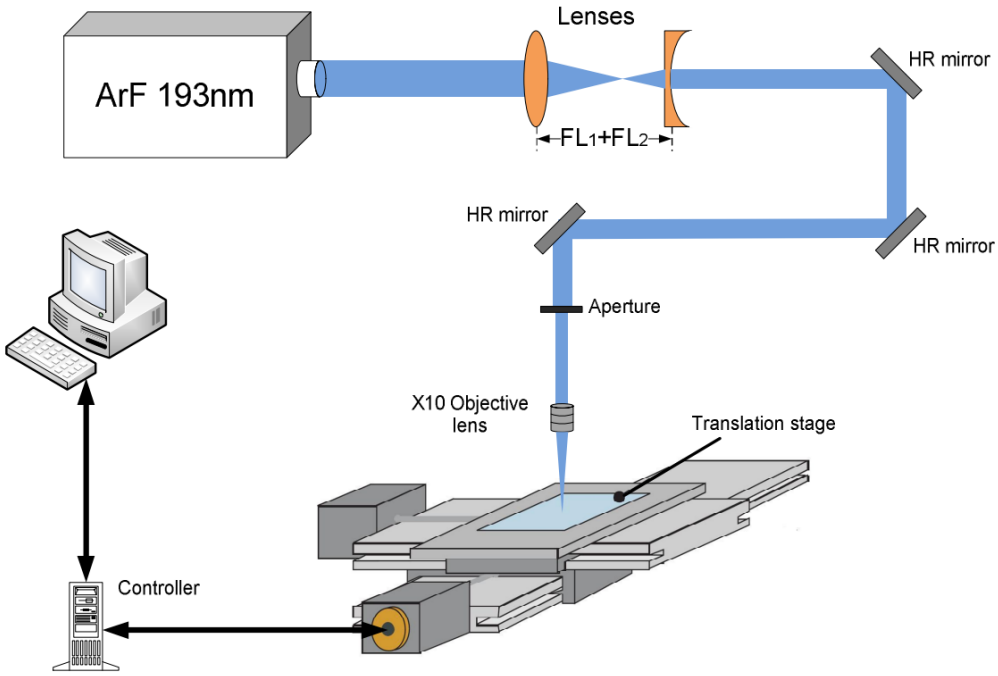

Figure 6.8: Schematics of a typical laser micromachining system [46].

The used laser is an ArF excimer with a wavelength of 193 nm. Also, it is a pulsed laser with a pulsation of the order of the nanosecond. Usually, this kind of laser is used for the micromachining of piezoceramics (PZT), silicon carbide (SiC) or pyrex [11], but LIFT can also be performed. Concretely, the laser passes through a defined mask of a specified shape depending on the desired pattern. Concerning the environment of operation, the ablation can be done in air, nitrogen or vacuum. It is also equipped with a digital microscope and a fume extraction mechanism. Views of the setup are illustrated in Figures 6.10 and 6.9.

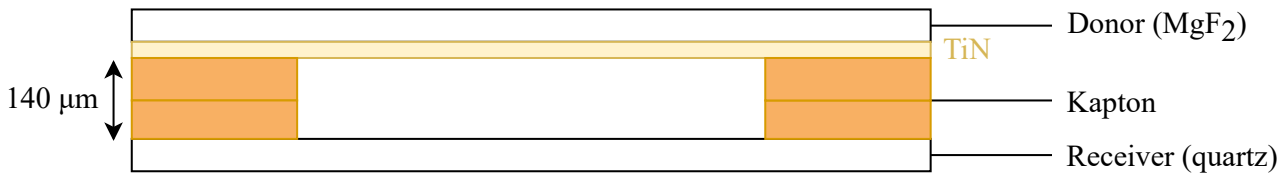

Figure 6.9: Schematics of the LIFT setup (side view).

The donor substrate for LIFT must be transparent for wavelengths corresponding to the used laser. The chosen one for tracks preparation is the MgF_2. The transmission range of MgF_2 starts at 120 nm and ends at 7 μm [13]. Thin films prepared over Si (100) cannot be used for LIFT. However, an alternative can be the ablation of the thin film directly to get the desired track. The receiver substrate is the final substrate used for applications in microheaters. Commonly used materials have already been presented in Figure 1.6. In this work, the track is prepared over a quartz crystal to allow a possible LIBT as it is transparent to UV wavelengths.

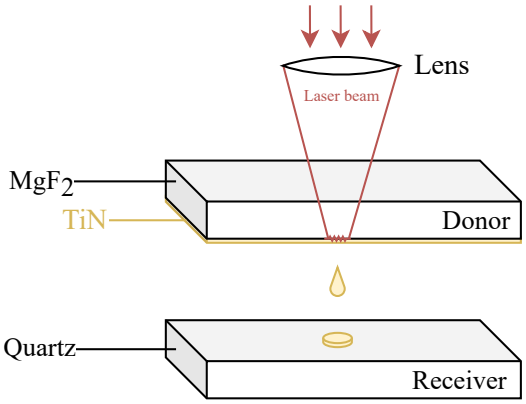

Figure 6.10: Schematics of the LIFT setup (3D view).

This instrument is used to study the way thin films can be transferred from the donor substrate onto a receiver substrate. More specifically in this work, about the TiN transfer between MgF_2 and quartz. To separate the two substrates by a known distance, two layers of 70 μm Kapton™ tape are used. A picture of the micromachining system is displayed in Figure 6.11.

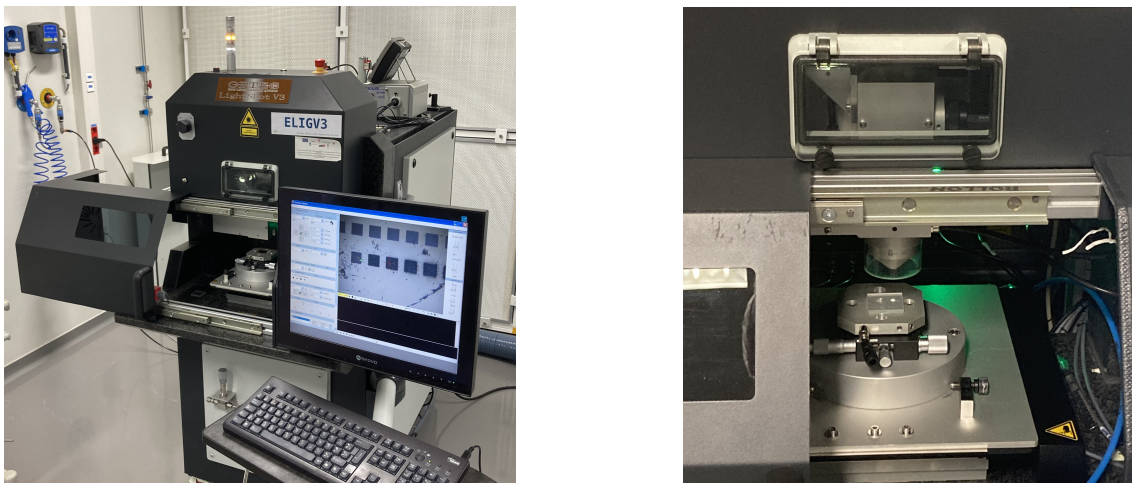

(a) General instrument.

(b) Transfer area.

Figure 6.11: Photography of the LIFT instrument.

6.3 Methodology

To complete this section, some LIFT tests have been performed with sample 9, having a thickness of approximately 44 nm on a MgF_2 donor substrate. The track deposition is made over a quartz receiver substrate positioned at 140 μm, as shown in Figure 6.9. First, the behavior of the ablation with respect to the provided energy is studied by making a row matrix of energies varying from 0.36 mJ to 1.44 mJ ($\Delta E = 0.18mJ$). Then, two lines of 8 mm are made: one only constituted of 1 layer of TiN (L1), the other one constituted of 5 superposed layers (L5). Hereafter in Table 6.2 are listed the main track preparation settings.

Table 6.2: Important used settings for LIFT tests.

	Matrix	**Lines**
Energy (mJ)	1.8	3-4*
Transmission (%)	20-80	30-45*
Repetition rate (Hz)	5	
Pattern shape	Rectangle	
Pattern dimension (μm)	125	
Medium	Medium	

The wear of the laser due to its end of life led to undesired stability problems: the laser had to be refilled three times during the process. Consequently, all results shown here are not completely relevant on a quantitative basis. However, in terms of tendencies and general qualitative interpretations, it is still useful to show and discuss them. Concerning lines (*), the energy was 4 mJ with $T = 30\%$ (= 1.2 mJ). Because of the laser instabilities, the energy at the end (around the third/fourth layer) changed to 3 mJ with $T = 45\%$ (= 1.35). So L5 was submitted to an average laser energy of $\sim$ 1.28 mJ.

After that, the tracks are observed with the digital microscope described in chapter 3 with a magnification of 250x. This microscope is also used to determine the width of L5. In parallel, its thickness is estimated with the profiler to estimate an eventual final deposited volume. The used mode is VSI and not PSI like the samples thickness determination. Finally, the roughness of L1 and L5 are measured still with the profiler also in VSI. General measurement settings are listed below.

- Optical magnification: 5x (thickness det.), 20x (roughness det.).
- Numerical magnification: 1x.
- Post-process correction: Modal tilt only (thickness det.), Tilt and cylinder (roughness det.).
- 5 measurements (at different locations).

Post measurements corrections are the same as the ones used previously for the determination of the thickness and roughness for thin film samples deposited by IBS.

6.4 Results and discussion

First, the fluence of the laser is given by Equation 6.1, so the variation of the ablation with respect to the energy can be expressed in terms of fluence. Figure 6.12 shows digital microscope images of the ablation evolution with respect to the fluence. It can be observed that for the two first ablation patterns, sides still have imperfections, highlighted in red. Then, for fluences around 5 J/cm^2, the ablation is well defined, and this range can be assimilated to the optimal fluence. For higher fluences, some spreading becomes to be visible, similarly to the high fluence deposition shown in Figure 6.6.

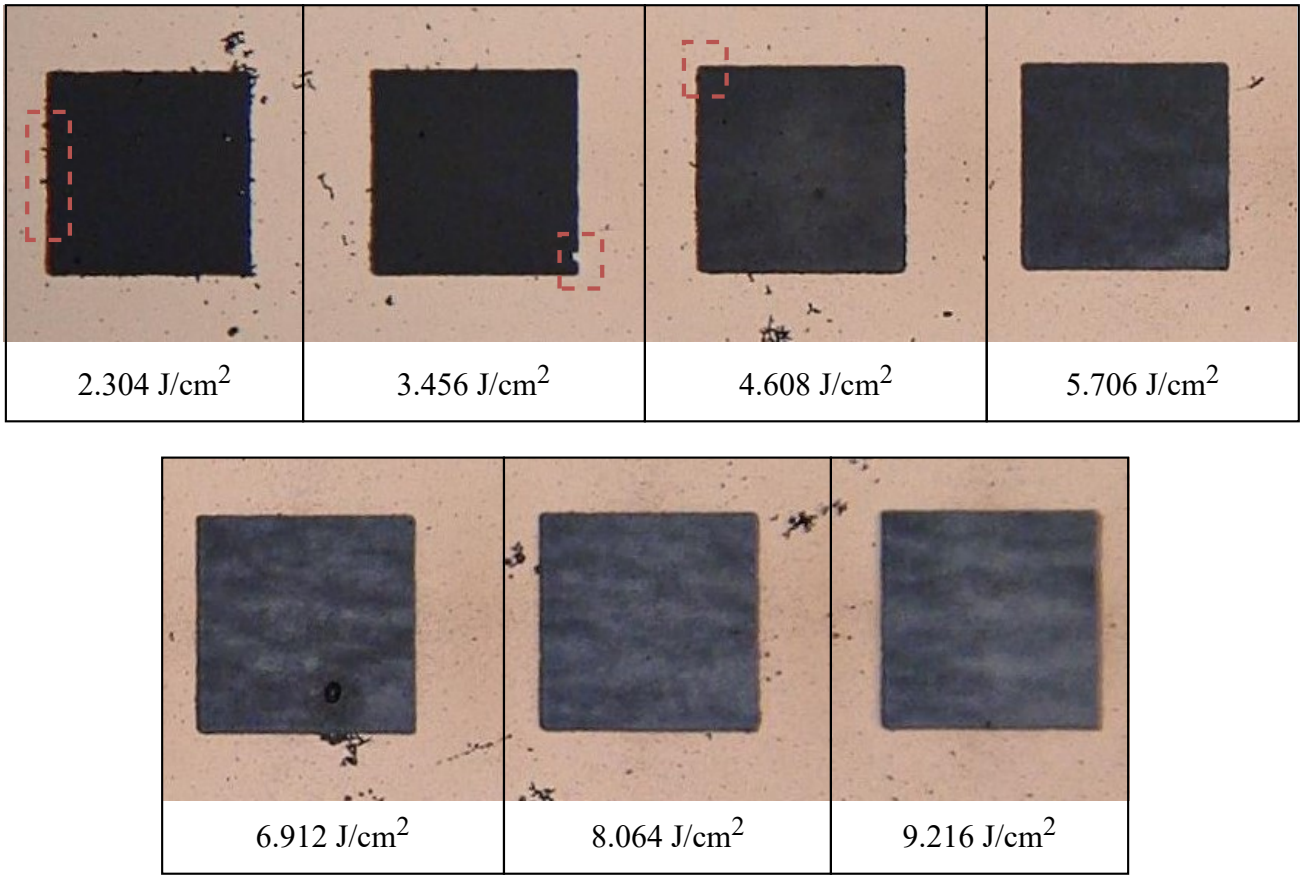

Figure 6.12: Images of the ablation evolution with respect to the fluence taken by the digital microscope (sample 9).

Concerning the deposited track, L1 and L5 are shown in Figure 6.13. They both have a deposited length of 8 mm. As a first observation, there is a clear change of color between them.

The width of L5 has also been determined directly with the microscope and is equal to

$$w_{\mathrm{L5}} = 129.5\mu\mathrm{m}\ . \tag{6.2}$$

This means that the deposited track is slightly wider that the initial ablation pattern of 125 μm. This represents an increase of 3.5 %. Some TiN parts are also outside the line, but with a lower density.

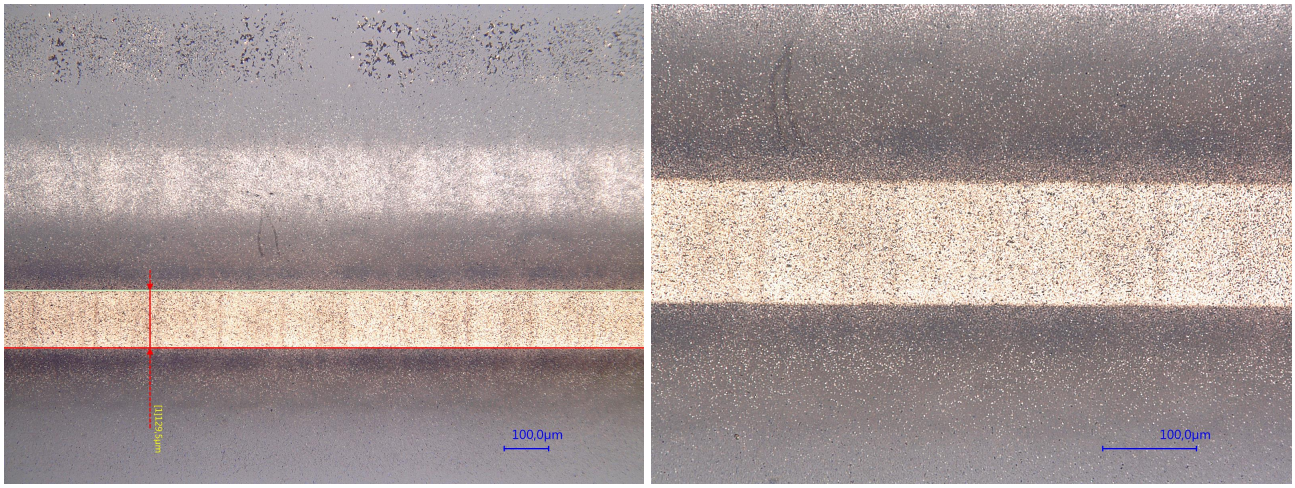

(a) L1 and L5. (b) L5.

Figure 6.13: Images of L1 and L5 taken by the digital microscope (MgF_2substrate).

A roughness analysis is performed for L5. Figure 6.14 shows an example of roughness measurement with the interferometric microscope. For L5,

$$S_a = 60 \pm 2 \text{ nm and } S_q = 90 \pm 2 \text{ nm}. \tag{6.3}$$

This roughness is at least 3 orders of magnitude greater than IBS deposited thin films on Si (100).

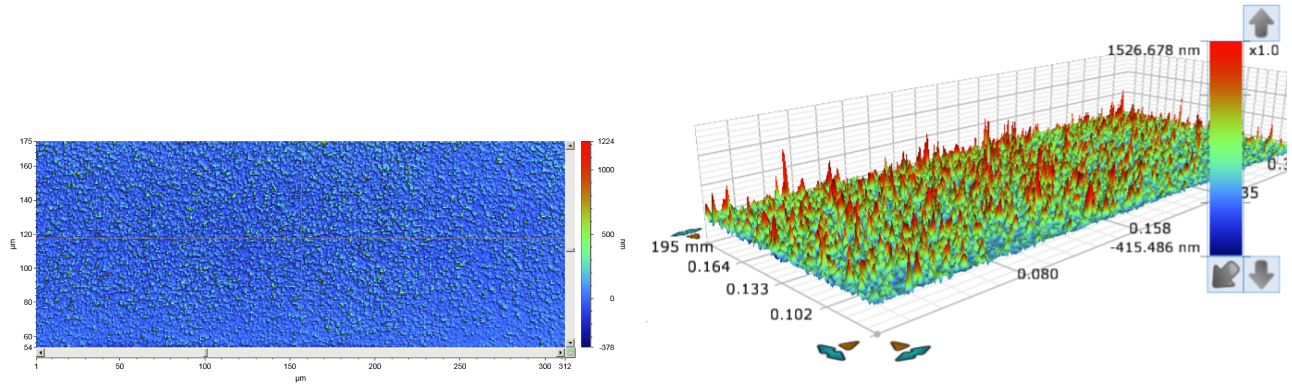

(a) 2D. (b) 3D.

Figure 6.14: Roughness profile of L5 measured by the profiler.

To conclude this section, a preliminary track deposition by LIFT has been made, followed by a basic characterization. It appeared that the optimal fluence is around 5 J/cm^2. In addition, roughness are much higher than the ones of the initial donor sample. However, all experimentations done in this section result from an instable laser setup in terms of energy. In this situation, results explained here have to be verified with a more stable laser to confirm these tendencies or not.

During the internship, experiments stopped at this point but the analysis could be taken a step further. For example, the investigation of the spacing between each ablation or the distance between substrates are interesting to study. Thickness determination of the deposited lines could lead to resistivity analysis.

Also, as an alternative, the track can be prepared directly by ablation instead of LIFT. Ablation could be useful to have less electrical properties variation due to the track preparation, as the substrate does not change.

Conclusion

The motivation behind this work stems from the need to outgas particles from a mirror surface to minimize their impact on the overall performance of a space optical instrument. Therefore, the objective was to establish a solid foundation for the fabrication of micro-heating systems integrated in the surface of mirrors. The second main objective was to enhance our understanding of the properties and preparation of nano-scale coatings. More specifically, the investigation was made on titanium nitride thin films characteristics variations as a function of thickness. In total, 14 TiN coatings over silicon (100) and 1 coating over magnesium fluoride were prepared and characterized, with thicknesses ranging from 6 to 138 nm. An investigation from the preparation of the coating to the preliminary phase of the implementation in a micro-heating system was performed.

An overview of microheater and applications led to the choice of TiN for the material constituting the heating track. The choice was motivated by its ability to withstand microheaters applications, especially in high temperature.

The coatings were prepared by Ion Beam Sputtering (IBS) with constants Ar and N_2 gas flows. Prepared coatings were assumed to be at a nitrogen saturation of 40%. It resulted from the analysis that the deposition rate varied between 0.55 and 0.78 nm/min and was decreasing with respect to the wanted deposited thickness.

During all the investigation, several measurement methods were compared. The thickness determination of coatings was performed by associating ellipsometry results and profiler measurements. The resistivity was determined from 4-point probe and ellipsometric measurements. It resulted to similar values all along the studied thickness range. Optical properties were determined by ellipsometry. The surface roughness was investigated from profiler measurements. All ellipsometry characterizations were made by assuming a Drude-Lorentz model.

Measurements revealed an undocumented resistivity peak for thicknesses of 44 ± 1 nm, reaching a resistivity of $215\pm 10\mu\Omega$·cm. The investigation of this peak resulted in the assumption that intrinsic stress changes inside the thin film as a function of thickness were producing changes in free charge carrier parameters. Resistivity analysis on the MgF_2 substrate consolidated this assumption. Measurements also revealed a decrease of resistivity beginning at approximately 330 $\mu\Omega$·cm for 5 nm and converging to a bulk resistivity of approximately 90 $\mu\Omega$·cm for coatings thicker than 100 nm.

The analysis of optical properties concluded that the refraction coefficient n and the extinction coefficient k as a function of wavelength can be estimated by assuming a Drude-Lorentz model until wavelengths of 1000 nm. It also revealed significant changes of optical properties behavior among the studied thin film thicknesses, and consequently the invalidity of bulk data at these thicknesses. The analysis of the surface roughness for thicknesses between 18 and 138 nm concluded that no roughness variations were observed. An average roughness S_a of 0.4$\pm$0.1 nm and a root mean square roughness S_q of 0.5$\pm$0.1 nm were the final outcomes. The coating prepared on the MgF_2 substrate was deposited over quartz by Laser-Induced Forward Transfer (LIFT). A line of 8 mm and 129.5 μm was deposited. The optimal fluence was determined to be around 5 J/cm^2. A preliminary characterization was made on the roughness and it resulted to a S_a of 60 nm$\pm$ 2 nm and a S_q of 90 nm$\pm$ 2 nm.

To conclude, this work revealed some unexpected particularities TiN coatings can have depending on the way to prepare and deposit it as a microheater. TiN coatings could therefore be a suitable option for the fabrication of micro-heating devices, but further investigations are needed.

Perspectives concerning the continuation are numerous. For the used materials themselves, the heating track, donor substrate and receiver substrate can be changed and studied with respect to their electrical properties or track preparation conditions. Concerning TiN coating preparation, two parameters were not studied in this work: the variation of nitrogen partial pressure and the effect of temperature. These parameters are therefore possible analysis axes to be investigated. The presented characterization can be investigated further. The preparation of more samples around the resistivity peak can lead to a better understanding of the highlighted phenomenon. Finally, A logical continuation of this work is the preparation and electrical characterization of more microheaters by LIFT. A possible alternative is, however, the possibility of using ablation to create the tracks instead.

Applications of microheaters are large and go beyond space applications. Results found here are therefore also exploitable in all kinds of micro-heating devices. The investigation is only at its beginning and the microheaters development is a source of endless possibilities.

Appendix A

Samples related data

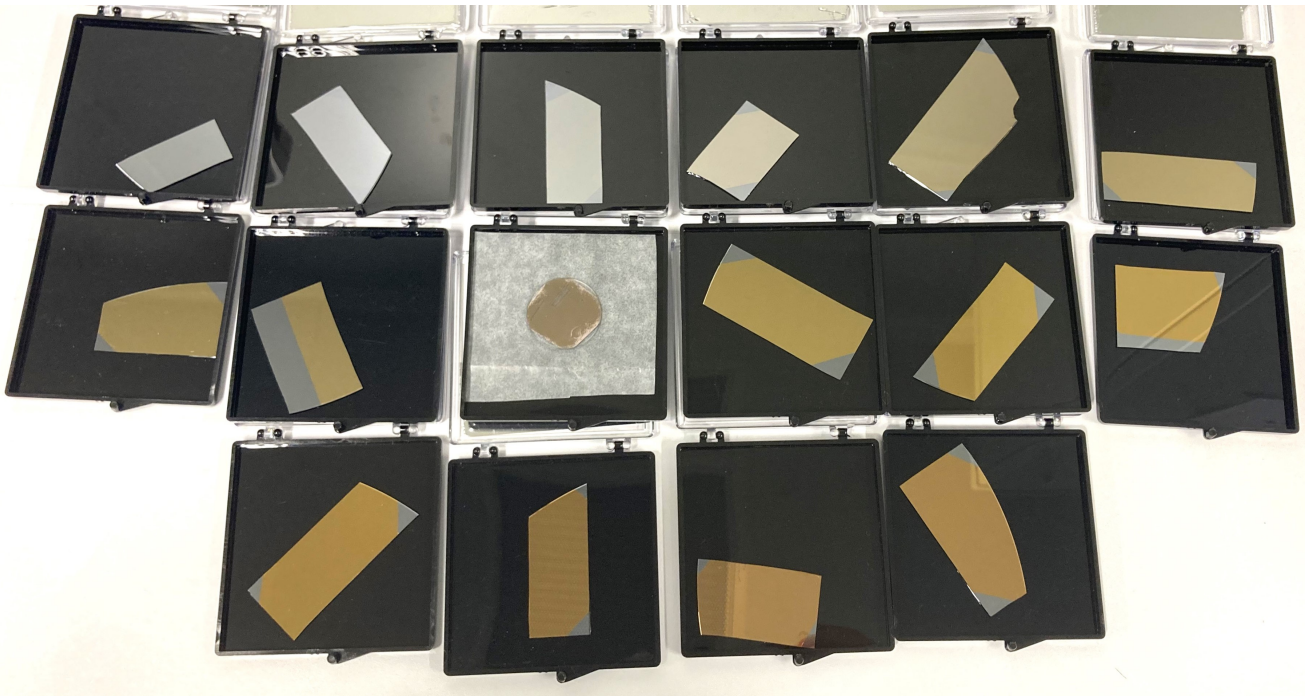

Figure A.1: Photography of all the samples, sorted by thickness.

Table A.1: Samples deposition data.

Sample #	**Date**	**t_{QCM} (nm)**	**Duration (h)**
1	09-04-24	0	-
2	08-05-24	5	00:07:59
3	15-04-24	10	00:15:22
4	10-04-24	20	00:29:30
5	02-04-24	35	00:46:17
6	16-05-24	45	01:03:35
7	19-03-24	50	-
8	07-05-24	50	01:08:34
9	14-05-24	50	01:12:40
10	13-05-24	60	01:32:14
11	10-10-24	75	01:51:31
12	11-04-24	100	02:19:57
13	20-03-24	-	-
14	22-04-24	130	02:55:46
15	25-03-24	150	-
16	29-04-24	175	04:16:10

Table A.2: Dimensions and resisitivity correction factors ($s = 2$ mm).

Sample	**a (cm)**	**b (cm)**	**a/b**	**b/s**	R_1
1	3	1.5	2	7.5	0.8905
2	3.5	2	1.75	10	0.9337
3	5	2	2.5	10	0.9345
4	3.5	2.25	1.56	11.25	0.9421
5	5	2.5	2	12.5	0.9521
6	5.5	2	2.75	10	0.9345
7	4	2	2	10	0.9345
8	4	1.5	2.67	7.5	0.8905
9	2.5	2.5	1	12.5	0.9498
10	5.5	2.5	2.2	12.5	0.9521
11	4.5	2	2.25	10	0.9345
12	5	2.5	2	12.5	0.9521
13	4	3	1.33	15	0.9687
14	4	2	2	10	0.9345
15	4	2	2	10	0.9345
16	4	2.5	1.6	12.5	0.9511

Appendix B

Interferometric step height measurement correction

When using the PSI mode in the interferometric microscope to measure the step height between two different materials, a correction factor is needed. This is because the phase shift due to the reflection of the monochromatic light is not the same when several materials are involved. An illustration is provided in Figure B.1.

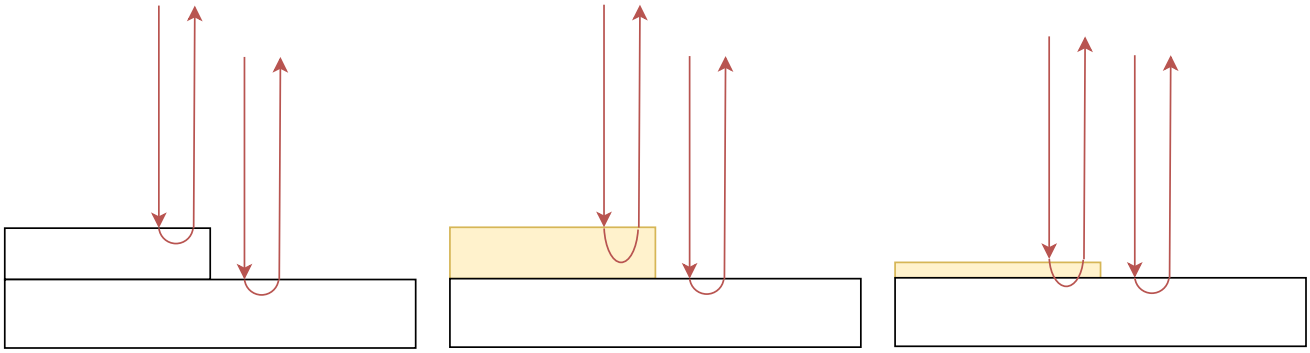

Figure B.1: Step height measurements changes .

For opaque films involving the same material, the measured step distance is given by

$$d_m = d = \frac{\text{OPD}}{2} = \frac{\phi\lambda}{4\pi}, \tag{B.1}$$

where, OPD stands for Optical Path Difference, d is the real distance, ϕ is the phase shift, and λ is the wavelength of the light. But when it comes to opaque films involving two different materials, the measured distance is given by

$$d_m = d + \frac{\Delta\phi\lambda}{4\pi}. \tag{B.2}$$

Thus, to know the phase shift difference between both reflected beams, ellipsometry can be used. The difference between d and d_m is given by

$$d - d_m = \left[\operatorname{atan} \left(\frac{2k_t(1 - n_b^2 - k_b^2) - 2k_b(1 - n_t^2 - k_t^2)}{(1 - n_t^2 - k_t^2)(1 - n_b^2 - k_b^2) + 4k_t k_b} \right) \right] \frac{\lambda}{4\pi}, \tag{B.3}$$

where n and k are the refractive index and the extinction coefficient at measured wavelength λ. The subscripts b and t stand for bottom and top. So, ellipsometer measurements provide the correction factor to the distance measured with the profiler.

For semi-transparent films, the software *Essential MacLeod* [20] is used. As samples are composed of TiN on Si substrates, the software bases on the Abeles matrix formalism to calculate the phase difference between Si and semi-transparent film on Si, here TiN. From there, the thickness correction is calculated for each sample.

Appendix C

Uncertainties estimation

UV-VIS-NIR ellipsometer measurements

UV-VIS-NIR ellipsometer measurements are based on the Drude-Lorentz fitting of samples if the *SpectraRay/4* software [18]. As a reminder, the Drude-Lorentz model expression is given in Equation 4.1. The instrument documentation referenced the uncertainty on Ψ and Δ measurements, listed below.

- $\delta\Psi$ = 0.05°: due to the sample tilt and the absolute offset calibration accuracy.
- $\delta\Delta$ = 0.1°: drift resulting from variations in the light source and temperature changes.

Then, the studied parameter is changed manually until reaching theoretical curves limit variations given by ($\delta\Psi$,$\delta\Delta$). The variation for thickness δt_Ψ leading to $\delta\Psi$ and δt_Δ the one leading to $\delta\Delta$ are calculated and the highest one is always taken. Once δt is known, the uncertainly percentage is given by

$$\epsilon_h = \frac{\delta t}{t} \cdot 100 \,. \tag{C.1}$$

The exact same methodology is applied to determine the free charges uncertainties ϵ_{ω_p} ϵ_{ω_τ}. Concerning the resistivity obtained from the fitting of the Drude-Lorentz model, it is given by

$$R_{\text{el}} = \frac{\omega_\tau}{\omega_p^2} \cdot \frac{1}{2\pi\varepsilon_0 c} \,. \tag{C.2}$$

Its variation can be calculated :

$$\delta R_{\text{el}} + R_{\text{el}} = \frac{\omega_\tau + \delta\omega_\tau}{(\omega_p + \delta\omega_p)^2} \cdot \frac{1}{2\pi\varepsilon_0 c} \,. \tag{C.3}$$

$$\implies \delta R_{\text{el}} = \frac{\omega_\tau + \delta\omega_\tau}{(\omega_p + \delta\omega_p)^2} \cdot \frac{1}{2\pi\varepsilon_0 c} - R_{\text{el}} \,. \tag{C.4}$$

Thus, it gives

$$\delta(R_{\text{el}})_\uparrow = \frac{\omega_\tau + \delta(\omega_\tau)_\uparrow}{(\omega_p + \delta(\omega_p)_\downarrow)^2} \cdot \frac{1}{2\pi\varepsilon_0 c} - R_{\text{el}} \,, \tag{C.5}$$

for the upper limit and

$$\delta(R_{\text{el}})_{\downarrow} = \frac{\omega_\tau + \delta(\omega_\tau)_{\downarrow}}{(\omega_p + \delta(\omega_p)_{\uparrow})^2} \cdot \frac{1}{2\pi\varepsilon_0 c} - R_{\text{el}} \,, \tag{C.6}$$

for the lower one. The uncertainty percentage is finally given by

$$\epsilon_{R_{\text{el}}} = \frac{\delta R_{\text{el}}}{R_{\text{el}}} \cdot 100 \,. \tag{C.7}$$

4PP resistivity measurements

The resistivity obtained from the 4PP measurements and the thickness calculation is given by

$$R_{\text{4PP}} = t \cdot R_{\text{sheet, 4PP}} \,, \tag{C.8}$$

where R_{4PP} is the final resistivity, t is the thickness and $R_{\text{sheet, 4PP}}$ the electrical sheet resistivity from the 4PP measurements. The uncertainty is then given by

$$R_{\text{4PP}} + \delta R_{\text{4PP}} = (t + \delta t) \cdot (R_{\text{sheet, 4PP}} + \delta R_{\text{sheet, 4PP}}) \,. \tag{C.9}$$

$$\implies \delta R_{\text{4PP}} = (t + \delta t) \cdot (R_{\text{sheet, 4PP}} + \delta R_{\text{sheet, 4PP}}) - R_{\text{4PP}} \,, \tag{C.10}$$

where t, δt, $R_{\text{sheet, 4PP}}$, $\delta R_{\text{sheet, 4PP}}$ and R_{4PP} are known for each sample. The critical cases are the combination $(\delta h, \delta R_{\text{sheet, 4PP}})_{\text{max}}$ for the higher bond and $(\delta t, \delta R_{\text{sheet, 4PP}})_{\text{min}}$ for the lower one. Thus, it gives

$$\delta(R_{\text{4PP}})_{\uparrow} = (t + \delta(t)_{\uparrow}) \cdot (R_{\text{sheet, 4PP}} + \delta(R_{\text{sheet, 4PP}})_{\uparrow}) - R_{\text{4PP}} \,, \tag{C.11}$$

for the upper limit and

$$\delta(R_{\text{4PP}})_{\downarrow} = (t + \delta(t)_{\downarrow}) \cdot (R_{\text{sheet, 4PP}} + \delta(R_{\text{sheet, 4PP}})_{\downarrow}) - R_{\text{4PP}} \,, \tag{C.12}$$

for the lower one. The uncertainty percentage is finally given by

$$\epsilon_{R_{\text{4PP}}} = \frac{\delta R_{\text{4PP}}}{R_{\text{4PP}}} \cdot 100 \,. \tag{C.13}$$

Bibliography

[1] J. Alami, K. Sarakinos, G. Mark, and M. Wuttig. On the deposition rate in a high power pulsed magnetron sputtering discharge. *Applied Physics Letters*, 89(15):154104, October 2006.

[2] L. Bartha. Positive-Ion Sources. In Ragnar Hellborg, editor, *Electrostatic Accelerators: Fundamentals and Applications*, Particle Accelerator and Detection, pages 192–221. Springer Berlin, Heidelberg, ragnar hellborg edition, 2005.

[3] M. Becker, M. Gies, A. Polity, S. Chatterjee, and P. J. Klar. Materials processing using radio-frequency ion-sources: Ion-beam sputter-deposition and surface treatment. *Review of Scientific Instruments*, 90(2):023901, February 2019.

[4] E. Benes. Improved quartz crystal microbalance technique. *Journal of Applied Physics*, 56(3):608–626, August 1984.

[5] Frank Bernoux, Jean-Philippe Piel, Bernard Castellon, Christophe Defranoux, Jean-Hervé Lecat, Pierre Boher, and Jean-Louis Stehlé. Ellipsométrie. *Techniques de l'Ingénieur*, June 2003.

[6] P. Bhattacharyya. Technological Journey Towards Reliable Microheater Development for MEMS Gas Sensors: A Review. *IEEE Transactions on Device and Materials Reliability*, 14(2):589–599, June 2014. Conference Name: IEEE Transactions on Device and Materials Reliability.

[7] Inc. Bruker Nano. ContourGT-K Optical profiler User Manual, October 2012.

[8] J.F. Creemer, D. Briand, Henny Zandbergen, W. Vlist, Charles Deboer, N.F. Rooij, and P.M. Sarro. Microhotplates with TiN heaters. *Sensors and Actuators A: Physical*, 148:416–421, December 2008.

[9] Ankit Das, Aniruddha Ghosh, Somnath Chattopadhyaya, and Chien-Fang Ding. A review on critical challenges in additive manufacturing via laser-induced forward transfer. *Optics & Laser Technology*, 168:109893, January 2024.

[10] Philippe Delaporte and Anne-Patricia Alloncle. [INVITED] Laser-induced forward transfer: A high resolution additive manufacturing technology. *Optics & Laser Technology*, 78:33–41, April 2016.

[11] Jean-Philippe Desbiens and Patrice Masson. ArF excimer laser micromachining of Pyrex, SiC and PZT for rapid prototyping of MEMS components. *Sensors and Actuators A: Physical*, 136(2):554–563, May 2007.

[12] V. Dinca, A. Palla Papavlu, A. Matei, C. Luculescu, M. Dinescu, T. Lippert, F. Di Pietrantonio, D. Cannata, M. Benetti, and E. Verona. A comparative study of DRL-lift and lift on integrated polyisobutylene polymer matrices. *Applied Physics A*, 101(2):429–434, November 2010.

[13] A. Duncanson and R. W. H. Stevenson. Some Properties of Magnesium Fluoride crystallized from the Melt. *Proceedings of the Physical Society*, 72(6):1001, December 1958.

[14] Camilo Florian and Pere Serra. Printing via Laser-Induced Forward Transfer and the Future of Digital Manufacturing. *Materials (Basel, Switzerland)*, 16(2):698, January 2023.

[15] Nikolay Gavrilov. High Current Gaseous Ion Sources. In *The Physics and Technology of Ion Sources, Second Edition*, pages 107–132. Wiley, ian g. brown edition, July 2005.

[16] Lucille A. Giannuzzi and North Carolina State University. *Introduction to Focused Ion Beams: Instrumentation, Theory, Techniques and Practice*. Springer Science & Business Media, November 2004.

[17] David A Glocker and S Ismat Shah. *Handbook of Thin Film ¨Process Technology*, volume 2. Institute of Physics Publishing, Bristol and Philadelphia, 1998.

[18] SENTECH Instruments GmbH. SpectraRay4 Software Manual, July 2017.

[19] Maxtek Inc. Maxtek DCM-250 Windows Based Deposition Control Software, 2007.

[20] Thin Film Center Inc. Essential MacLeod , Optical Coating Design Program -User's manual, 1997.

[21] Z. E. Jeroish, K. S. Bhuvaneshwari, Fahmi Samsuri, and Vigneswaran Narayanamurthy. Microheater: material, design, fabrication, temperature control, and applications—a role in COVID-19. *Biomedical Microdevices*, 24(1):3, December 2021.

[22] Il-seok Kim and Prashant N. Kumta. Hydrazide sol–gel process: A novel approach, for synthesizing nanostructured titanium nitride. *Materials Science and Engineering: B*, 98(2):123–134, March 2003.

[23] Jeong Ah Kim, Seung Hwan Lee, Hongsuk Park, Jong Hyo Kim, and Tai Hyun Park. Microheater based on magnetic nanoparticle embedded PDMS. *Nanotechnology*, 21(16):165102, March 2010.

[24] Charles Kittel and Paul McEuen. *Introduction to Solid State Physics*. John Wiley & Sons, 2018. Google-Books-ID: nNpVEAAAQBAJ.

[25] Lothar Koch, Andrea Deiwick, Sabrina Schlie, Stefanie Michael, Martin Gruene, Vincent Coger, Daniela Zychlinski, Axel Schambach, Kerstin Reimers, Peter M. Vogt, and Boris Chichkov. Skin tissue generation by laser cell printing. *Biotechnology and Bioengineering*, 109(7):1855–1863, July 2012.

[26] Lothar Koch, Stefanie Kuhn, Heiko Sorg, Martin Gruene, Sabrina Schlie, Ralf Gaebel, Bianca Polchow, Kerstin Reimers, Stephanie Stoelting, Nan Ma, Peter M. Vogt, Gustav Steinhoff, and Boris Chichkov. Laser printing of skin cells and human stem cells. *Tissue Engineering. Part C, Methods*, 16(5):847–854, October 2010.

[27] Thomas Lautenschläger and Carsten Bundesmann. Reactive ion beam sputtering of Ti: Influence of process parameters on angular and energy distribution of sputtered and backscattered particles. *Journal of Vacuum Science & Technology A*, 35(4):041001, June 2017.

[28] Dongqing Li. Absolute Pressure. In *Encyclopedia of Microfluidics and Nanofluidics*, pages 1–1. Springer US, Boston, MA, 2008.

[29] Qingfeng Li, Anne Patricia Alloncle, David Grojo, and Philippe Delaporte. Generating liquid nanojets from copper by dual laser irradiation for ultra-high resolution printing. *Optics Express*, 25(20):24164–24172, October 2017. Publisher: Optica Publishing Group.

[30] H. A. (Hendrik Antoon) Lorentz. *The theory of electrons and its applications to the phenomena of light and radiant heat*. Leipzig : B.G. Teubner ; New York : G.E. Stechert, 1916.

[31] S. A. Mathews, R. C. Y. Auyeung, H. Kim, N. A. Charipar, and A. Piqué. High-speed video study of laser-induced forward transfer of silver nano-suspensions. *Journal of Applied Physics*, 114(6):064910, August 2013.

[32] L. Mele, F. Santagata, E. Iervolino, M. Mihailovic, T. Rossi, A. T. Tran, H. Schellevis, J. F. Creemer, and P. M. Sarro. A molybdenum MEMS microhotplate for high-temperature operation. *Sensors and Actuators A: Physical*, 188:173–180, December 2012.

[33] Latifa Melk. Thermal analysis of hard ceramics, 2011. Validerat; 20110929 (anonymous).

[34] Andrew J. de Mello, Matthew Habgood, N. Llewellyn Lancaster, Tom Welton, and Robert C. R. Wootton. Precise temperature control in microfluidic devices using Joule heating of ionic liquids. *Lab on a Chip*, 4(5):417–419, October 2004. Publisher: The Royal Society of Chemistry.

[35] Li-Jian Meng and M. P. dos Santos. Investigations of titanium oxide films deposited by d.c. reactive magnetron sputtering in different sputtering pressures. *Thin Solid Films*, 226(1):22–29, April 1993.

[36] Violeta Merie, Marius Pustan, Gavril Negrea, and Corina Bîrleanu. Research on titanium nitride thin films deposited by reactive magnetron sputtering for MEMS applications. *Applied Surface Science*, 358:525–532, December 2015.

[37] Yoshiki Nakata, Koji Tsubakimoto, Noriaki Miyanaga, Aiko Narazaki, Tatsuya Shoji, and Yasuyuki Tsuboi. Laser-Induced Transfer of Noble Metal Nanodots with Femtosecond Laser-Interference Processing. *Nanomaterials*, 11(2):305, February 2021. Number: 2 Publisher: Multidisciplinary Digital Publishing Institute.

[38] nanoScience Instruments. Profilometry, 2024.

[39] W. D. Nix and B. M. Clemens. Crystallite coalescence: A mechanism for intrinsic tensile stresses in thin films. *Journal of Materials Research*, 14(8):3467–3473, August 1999.

[40] Alexandra Palla-Papavlu, V Dinca, Iurie Roatesi, Antoniu Moldovan, James Shaw-Stewart, C. Schneider, Eugenia Kovacs, Thomas Lippert, and Dinescu Maria. Microfabrication of polystyrene microbead arrays by laser induced forward transfer. *Journal of Applied Physics*, 108, September 2010.

[41] Panos Patsalas, Nikolaos Kalfagiannis, and Spyros Kassavetis. Optical Properties and Plasmonic Performance of Titanium Nitride. *Materials*, 8(6):3128–3154, June 2015. Number: 6 Publisher: Multidisciplinary Digital Publishing Institute.

[42] Amitesh Paul and Jorg Wingbermühle. Surface morphology for ion-beam sputtered Al layer with varying sputtering conditions. *Applied Surface Science*, 252(23):8151–8155, September 2006.

[43] Hugh O. Pierson. *Handbook of Refractory Carbides & Nitrides: Properties, Characteristics, Processing and Apps.* Elsevier Science, January 2013.

[44] Alberto Piqué. Chapter 1.1 - Laser-Based Micro–Additive Manufacturing Technologies. In Tommaso Baldacchini, editor, *Three-Dimensional Microfabrication Using Two-photon Polymerization*, Micro and Nano Technologies, pages 1–19. William Andrew Publishing, Oxford, January 2016.

[45] N Popović, Ž Bogdanov, B Goncić, S Zec, Z Rakočević, M Zlatanović, and D Peruško. TiN thin films deposited by ion beam sputtering: effects of energetic particles bombardment. *Thin Solid Films*, 459(1):286–291, July 2004.

[46] Deyao Ren, J. Narayan, and Yuan-Shin Lee. Machined Surface Error Analysis for Laser Micromachining of Biocompatible Polymers for Medical Devices Manufacturing. *Computer-Aided Design & Applications*, 6:781–793, January 2009.

[47] S H Roshna. Magnetron sputter deposition method, June 2023.

[48] L. Roux, J. Hanus, J. C. Francois, and M. Sigrist. The optical properties of titanium nitrides and carbides: Spectral selectivity and photothermal conversion of solar energy. *Solar Energy Materials*, 7(3):299–312, December 1982.

[49] T. Sano, H. Yamada, T. Nakayama, and I. Miyamoto. Experimental investigation of laser induced forward transfer process of metal thin films. *Applied Surface Science*, 186(1):221–226, January 2002.

[50] F. M. Smits. Measurement of sheet resistivities with the four-point probe. *The Bell System Technical Journal*, 37(3):711–718, May 1958. Conference Name: The Bell System Technical Journal.

[51] F Solzbacher, C Imawan, H Steffes, E Obermeier, and M Eickhoff. A new SiC/HfB2 based low power gas sensor. *Sensors and Actuators B: Chemical*, 77(1):111–115, June 2001.

[52] Pol Sopeña, Sergio González-Torres, Juan Marcos Fernández-Pradas, and Pere Serra. Spraying dynamics in continuous wave laser printing of conductive inks. *Scientific Reports*, 8(1):7999, May 2018. Number: 1 Publisher: Nature Publishing Group.

[53] Ronald G. Spruit, J. Tijn van Omme, Murali K. Ghatkesar, and H. Hugo Pérez Garza. A Review on Development and Optimization of Microheaters for High-Temperature In Situ Studies. *Journal of Microelectromechanical Systems*, 26(6):1165–1182, December 2017. Conference Name: Journal of Microelectromechanical Systems.

[54] Koji Sugioka, Michel Meunier, and Alberto Piqué, editors. *Laser Precision Microfabrication*, volume 135 of *Springer Series in Materials Science*. Springer, Berlin, Heidelberg, 2010.

[55] J. E. Sundgren, B. O. Johansson, S. E. Karlsson, and H. T. G. Hentzell. Mechanisms of reactive sputtering of titanium nitride and titanium carbide II: Morphology and structure. *Thin Solid Films*, 105(4):367–384, July 1983.

[56] Haldor Topsoe. *Geometric Factors in Four Point Resistivity Measurement*. Semiconductor division, May 1968.

[57] Emre Turkoz, Romain Fardel, and Craig B. Arnold. Advances in Blister-Actuated Laser-Induced Forward Transfer (BA-LIFT). In *Laser Printing of Functional Materials*, pages 91–121. John Wiley & Sons, Ltd, 2018.

[58] L. Valdes. Resistivity Measurements on Germanium for Transistors. *Proceedings of the IRE*, 42(2):420–427, February 1954.

[59] G. Velmathi, N. Ramshanker, and S. Mohan. Design, Electro-Thermal simulation and geometrical optimization of double spiral shaped microheater on a suspended membrane for gas sensing. In *IECON 2010 - 36th Annual Conference on IEEE Industrial Electronics Society*, pages 1258–1262, November 2010. ISSN: 1553-572X.

[60] Joost Vlassak. Thin Film Mechanics. Technical report, DEAS Harvard University, 2004.

[61] X. Zeng, X.L. Mao, R. Greif, and R.E. Russo. Experimental investigation of ablation efficiency and plasma expansion during femtosecond and nanosecond laser ablation of silicon. *Applied Physics A*, 80(2):237–241, February 2005.

[62] M. Zenou, A. Sa'ar, and Z. Kotler. Laser jetting of femto-liter metal droplets for high resolution 3D printed structures. *Scientific Reports*, 5(1):17265, November 2015. Number: 1 Publisher: Nature Publishing Group.

[63] Michael Zenou and Lucy Grainger. 3 - Additive manufacturing of metallic materials. In Jing Zhang and Yeon-Gil Jung, editors, *Additive Manufacturing*, pages 53–103. Butterworth-Heinemann, January 2018.

[64] I. Zergioti, S. Mailis, N. A. Vainos, C. Fotakis, S. Chen, and C. P. Grigoropoulos. Microdeposition of metals by femtosecond excimer laser. *Applied Surface Science*, 127-129:601–605, May 1998.

[65] W. Zhang, S. H. Brongersma, O. Richard, B. Brijs, R. Palmans, L. Froyen, and K. Maex. Influence of the electron mean free path on the resistivity of thin metal films. *Microelectronic Engineering*, 76(1):146–152, October 2004.

[66] Wenjie Zhang, Jian Cai, Dejun Wang, Qian Wang, and Shuidi Wang. Properties of TiN films deposited by atomic layer deposition for through silicon via applications. In *2010 11th International Conference on Electronic Packaging Technology & High Density Packaging*, pages 7–11, August 2010.

[67] Božana Čolović, Danilo Kisić, Bojan Jokanović, Zlatko Rakočević, Ilija Nasov, Anka Trajkovska Petkoska, and Vukoman Jokanović. Wetting properties of titanium oxides, oxynitrides and nitrides obtained by DC and pulsed magnetron sputtering and cathodic arc evaporation. *Materials Science-Poland*, 37(2):173–181, June 2019.